LHCb calorimeter electronics. Photon identification. Calorimeter calibration

F. Machefert

LAL 11-38

UNIVERSITÉ PARIS-SUD

MÉMOIRE D'HABILITATION À DIRIGER DES RECHERCHES

LHCb calorimeter electronics Photon identification Calorimeter calibration

présenté par Frédéric Machefert

Soutenu le lundi 28 mars 2011 devant le jury composé de

Mr Pierluigi Campana
Mr Jacques Chauveau (Rapporteur)
Mr Jacques Lefrançois
Mr Achille Stocchi (Président)
Mme Isabelle Wingerter-Seez (Rapporteur)
Mr Ken Wyllie (Rapporteur)

Contents

1 The LHCb detector **9**
- 1.1 Detector overview . . . 9
- 1.2 The beam pipe . . . 13
- 1.3 The tracking system . . . 13
  - 1.3.1 The Vertex Locator . . . 14
  - 1.3.2 The Tracker Turicensis . . . 16
  - 1.3.3 The dipole magnet . . . 16
  - 1.3.4 The tracking chambers . . . 17
- 1.4 The RICH detectors . . . 18
- 1.5 The calorimeters . . . 20
  - 1.5.1 The scintillating pad detector and the preshower . . . 21
  - 1.5.2 The electromagnetic and hadronic calorimeters . . . 22
- 1.6 The muon chambers . . . 23
- 1.7 The LHCb trigger and acquisition . . . 25

I The electromagnetic and hadronic calorimeter electronics **27**

2 The front-end board **31**
- 2.1 General overview . . . 31
- 2.2 The Analog part of the front-end board. . . . 32
  - 2.2.1 Description . . . 32
  - 2.2.2 Characterisation of the shaper . . . 35
  - 2.2.3 ADC levels . . . 38
- 2.3 The Digital part of the front-end board . . . 39
  - 2.3.1 The front-end PGA . . . 40
  - 2.3.2 The sequencer . . . 44
- 2.4 Test beams results . . . 46
  - 2.4.1 Sampling window . . . 47
  - 2.4.2 Linearity . . . 48
  - 2.4.3 Noise . . . 48
  - 2.4.4 Crosstalk . . . 49

3 The calorimeter control card **51**
3.1 Introduction . . . 51
3.2 General Description . . . 53
3.3 Data capture and treatment . . . 54
3.4 Control of the crate . . . 58
3.4.1 Trigger, time and fast controls (TTC) . . . 58
3.4.2 Fault . . . 60
3.4.3 The slow control . . . 60
3.4.4 Resets . . . 60
3.5 Tests performed on the CROC and shielding . . . 61
3.5.1 Temperature measurements . . . 61
3.5.2 Overall crate synchronisation . . . 61
3.5.3 Bit error rates . . . 63
3.5.4 1 MHz test at the pit . . . 64
3.5.5 CROC shielding . . . 66

4 Control and acquisition software **69**
4.1 Software for the electronics . . . 69
4.2 Tests of the front-end boards . . . 71

5 Radiation tolerance of the electronics **75**
5.1 Introduction . . . 75
5.2 LHCb environment . . . 76
5.2.1 Particle flux . . . 76
5.3 Irradiations of the calorimeter front-end shaper . . . 79
5.3.1 Irradiation at the Centre de Proton Thérapie . . . 79
5.3.2 Irradiation at GANIL . . . 81
5.4 FPGA radiation tolerance . . . 87
5.4.1 Dose, single event latchup and single event dielectric rupture . . . 87
5.4.2 Single event upset cross-sections . . . 89
5.4.3 Single event upset and clock upset rate estimations . . . 90
5.4.4 LHCb front-end FPGA sensitivity and protections foreseen . . . 93
5.5 Summary table and conclusion . . . 97

II Photon identification and calorimeter calibration **99**

6 Photon identification **101**
6.1 Introduction . . . 101
6.2 Definitions . . . 101
6.3 Acceptance . . . 103
6.4 Reconstructed tracks removal . . . 103
6.5 The method . . . 104
6.6 Performances . . . 111

7 Absolute calibration of the ECAL and Preshower **117**
7.1 Introduction . . . 117
7.2 Toy Monte Carlo . . . 119
7.3 ECAL and PRS extraction method . . . 124
7.3.1 Energy scale extraction . . . 124
7.3.2 The β coefficients . . . 125
7.3.3 Width minimisation . . . 125
7.4 LHCb Monte Carlo . . . 127
7.4.1 Extraction of the calibration from the MC-truth . . . 127
7.4.2 β extraction on a Monte Carlo sample . . . 128
7.5 β extraction from the 2010 data sample . . . 132

Introduction

LHCb [17, 18] is one of the four particle physics experiments at the Large Hadron Collider at CERN. It is dedicated to heavy flavour physics, its main goal being the studies of CP-symmetry violation and rare decays in the sectors of the beauty and charm hadrons. LHCb aims at completing the understanding of the quark flavour physics and at revealing signs of new physics beyond the standard model in a complementary way to the larger multipurpose experiments ATLAS and CMS [92]. The current results on heavy flavour have been essentially obtained at the B-factories (Belle and Babar) or at the Tevatron (CDF and DØ) and showed no significant departure from the standard model predictions. LHCb aims at increasing the precision on the CP-symmetry measurements and the rare decays, many new physics models leading to new contributions to the CP-phases and to rare decay branching fractions.

The standard model is a relativistic quantum field theory [67, 88] which describes the strength and the matter content of the universe. Its prediction power is tremendous, but it still does not explain all our observations and suffers some paradox. It is now common to suppose that the standard model is an effective model of a more fundamental theory which still needs to be discovered [80].

Symmetries are a building block of any modern particle physics theory. The discrete symmetries charge conjugation (C), parity (P) and time reversal (T), respectively change the particles into their anti-particles, flip the space orientation or the direction of time. The combination of the three symmetries CPT is required by any relativistic quantum theory with local interactions. This has the consequence of making the mass and width of any particle to be equal to the mass and width of the corresponding anti-particle. But, no constraint is imposed on the C, P, T, CP, CT and PT operators [79].

In the standard model, the electromagnetic and strong forces are invariant under C, P and T operations where the weak force violates C and P. The violation of CP by the weak interaction was discovered in 1964 from the analysis of the neutral kaon decays [13, 29, 69].

It is now commonly accepted that at the origin of the universe, the big-bang took place and matter and anti-matter were present in balanced quantity. This subtle equilibrium has been broken since by a mechanism which is not understood yet and that led to a tiny positive amount of matter with respect to anti-matter when both annihilate to produce photons.

This mechanism implies that [89]

- the baryon number is not conserved,
- CP symmetry is violated,
- The thermal equilibrium was broken so that the effect that led to the matter anti-matter asymmetry was not compensated by the opposite phenomenon.

The CP violation which has been measured already on the K and B meson systems is not able to explain the amplitude of the mechanism that took place at the origin of the universe, but we could imagine that the energy scale at which we studied this phenomenon does not correspond to the conditions that occurred at that time. This is the motivation for increasing the energy and the statistics of the experiments so that we can be sensitive to any physics beyond the standard model possibly responsible for a stronger CP violation effect.

The search for new physics has taken two aspects. The first one, driven by experiments like ATLAS or CMS, consists in discovering new physics from the new particles involved. LHCb aims at measuring CP violation in the B sector with a yet unreached precision and is more sensitive to the couplings of those new particles and there interventions in virtual effects. In this sense, LHCb is sensitive altogether to the mass of those particles and to their couplings. A large mass making those particles difficult to be discovered directly could potentially be compensated by large couplings and exhibit sizable effects on the decays.

The LHCb detector aims at measuring the CP violation with an unprecedented precision and rare decays in the B meson sector. According to the CKM matrix at the origin of CP violation in the standard model, the B sector shows the largest amplitude for the effect, and if any new physics has to be seen this is most probably an interesting sector to study.

This document focuses mainly on the calorimeter system of the LHCb experiment, from the design of its electronics, the identification of the photons, which relies essentially on this system, to its calibration. The first section is an introduction to the LHCb detector. The rest of the document is divided in two parts. The first one is devoted to the electronics: the front-end will be described, then the configuration and test software developped specifically for the LHCb calorimeter groups. This part ends by addressing the potential problems linked to the radiation levels in the LHCb cavern. The second part is devoted to the preparation of the detector for analysis and partially uses the first data recorded in 2010. It is divided in two chapters regarding the identification of the photons and the absolute calibration of both the preshower and the electromagnetic calorimeter.

Chapter 1

The LHCb detector

Contents

1.1 Detector overview 9
1.2 The beam pipe 13
1.3 The tracking system 13
1.3.1 The Vertex Locator 14
1.3.2 The Tracker Turicensis 16
1.3.3 The dipole magnet 16
1.3.4 The tracking chambers 17
1.4 The RICH detectors 18
1.5 The calorimeters 20
1.5.1 The scintillating pad detector and the preshower 21
1.5.2 The electromagnetic and hadronic calorimeters 22
1.6 The muon chambers 23
1.7 The LHCb trigger and acquisition 25

1.1 Detector overview

LHCb [27] is a single arm spectrometer with a forward angular coverage (10 to (250) 300mrad in the (non-)bending plane of the detector) motivated by the fact that at high energies both quarks from the $b\bar{b}$ pairs are predominantly produced at small angles with respect to the beam. Hence, the acceptance is driven by the kinematics of the B mesons produced at the interaction point and by a compromise on the acceptance, the cost of the equipment that scales with its size and the existing cavern. The $b\bar{b}$ pair boost is given by the largest momentum parton of the two protons interacting and the optimisation led to an acceptance in the pseudo-rapidity range $2.0 \leq \eta \leq 5.5$ (see figure 1.2).

At the nominal luminosity $\mathcal{L} = 2 \times 10^{32}\text{cm}^{-2}\text{s}^{-1}$ and the nominal beam energy of 7 TeV, 3×10^{11} $b\bar{b}$ pairs should be produced at the experiment interaction point in a year of data

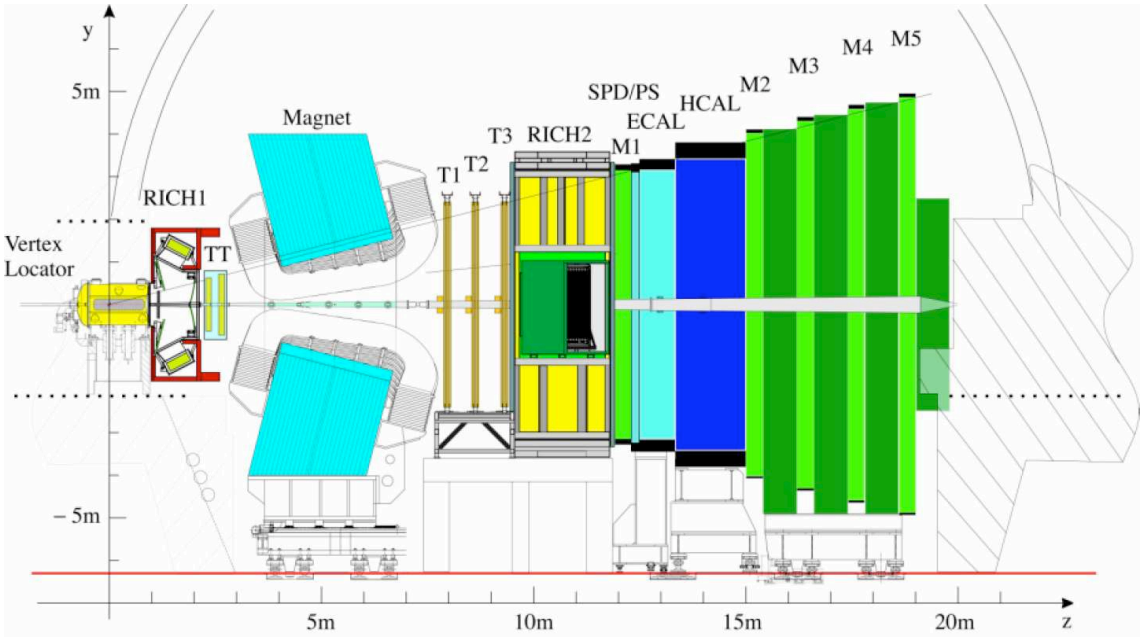

Figure 1.1: Overview of the LHCb detector.

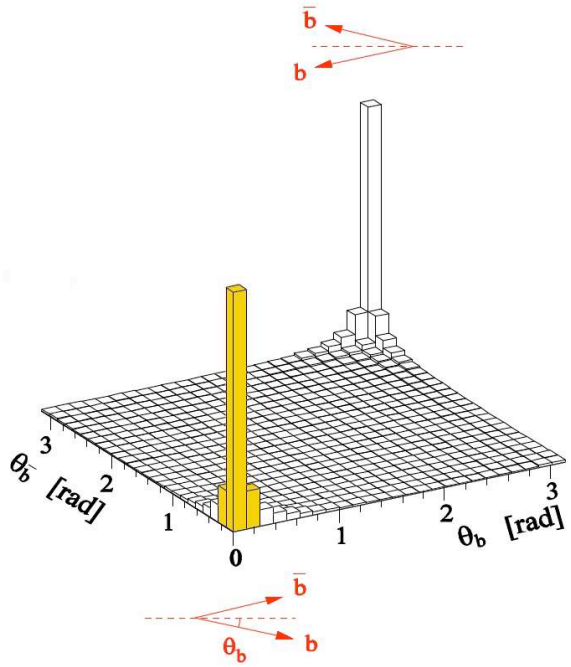

Figure 1.2: Angular distribution of the B mesons produced at the LHCb interaction point. The detector acceptance corresponds to the yellow bins of the 2D plots.

taking (considering 200 days and a Hübner factor of 0.25 [78]). LHCb benefits from a large $b\bar{b}$

cross-section of about 500μb and from a ratio $\sigma_{b\bar{b}}/\sigma_{inelastic}$ reaching 0.6%[1]. Although running at low luminosity leads to a lower statistics, it has the advantage of reducing the event pile-up and of producing events simpler to analyse. The overall detector radiation damage is also lower at LHCb than in other higher luminosity experiments which has an effect on the electronics design. Hence, the luminosity may be tuned independently from the other experiments by changing the beam focus.

LHCb consists of a magnet, a vertex locator (VELO), a tracking system, two ring imaging Cherenkov detectors, a calorimeter and a muon system. The figure 1.1 and picture 1.3 show a view of the detector.

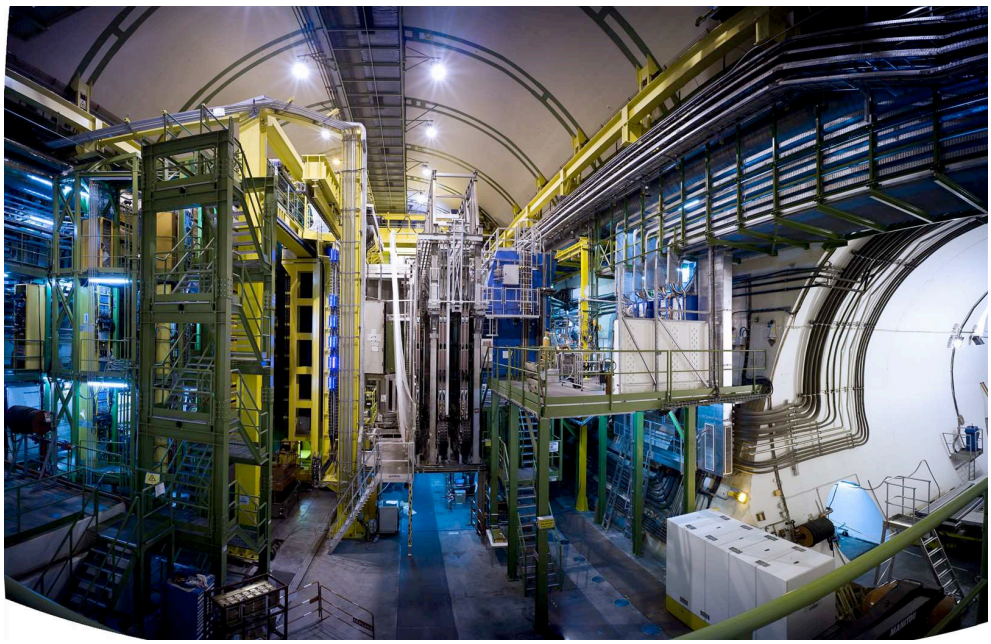

Figure 1.3: Picture of the LHCb detector after installation and seen from the counting room protection concrete wall. At the right (foreground), the access to the large well used to bring large equipments is visible. The LHCb detector is partially hidden by the frames and plateforms supporting the equipments. The z-axis, as seen on figure 1.1 goes here from right to left. Following it, the vertex locator where the interaction takes place is on the far right and cannot be seen. The magnet is the blue structure located behind the green platform. Then, the tracking stations and the RICH2 are visible. The yellow gantry is above the four calorimeters. The muon system is located farther away, close to the left cavern wall.

The main purpose of the LHCb calorimeters, that concern a large fraction of this document, is the selection and identification of hadrons, electrons and photons and the measurement of their energies and directions, both at the first trigger level and for the online reconstruction. Four sub-detectors are associated to perform such identification: a scintillating pad detector (SPD) and a preshower (PRS) allow to tag charged particles and to determine their electromagnetic nature; they are followed by an electromagnetic (ECAL) and a hadronic (HCAL)

[1] Those values are for a nominal beam energy of 7TeV. The $b\bar{b}$ cross-section is reduced and was measured to roughly 250μb at 3.5TeV.

calorimeter. The calorimeter system is used at the first level trigger (L0) of LHCb by providing high transverse energy electron, photon, neutral pion and hadron candidates. The response of the calorimeter system has to match the accelerator frequency and provides a measurement at 40MHz. The data are pipelined in the front-end electronics of the calorimeter, of the muon chambers and of the pile-up veto that contribute to the L0. Finally, the data are read out and sent to the CPU farm of the High Level Trigger (HLT) of LHCb at an average rate of 1.1MHz.

The LHCb experiment is located at the LHC interaction point 8, where DELPHI used to collect data at LEP time. The physics domain of the collaboration is very specific and requires to trigger on B event signatures which are mainly the large Pt of the daughters and the time of flight of the B meson (which is typically of 1cm). Those characteristics of the interesting events make the triggering on piled-up events more difficult. Hence, the beam conditions of the experiment are very different from those of the two big multipurpose experiments ATLAS and CMS where the nominal luminosity is planned to reach $10^{34}\text{cm}^{-2}\text{s}^{-1}$. At LHCb, the focusing of the beam is such that the luminosity is supposed to be in the range $2 \times 10^{32} - 5 \times 10^{32}\text{cm}^{-2}\text{s}^{-1}$ with an accelerator filled with 2808 bunches among which 2622 collide at the P8 interaction point. Then, the average number of events per crossing is around 0.4 as can be seen from figure 1.4 with a single collision in roughly 30% of the crossings.

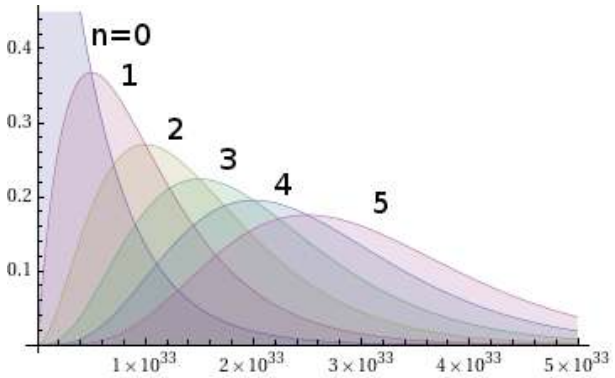

Figure 1.4: The probability to have from $n = 0$ and up to 5 collisions per bunch crossing depending on the luminosity at the LHCb interaction point ($\text{cm}^{-2}\text{s}^{-1}$).

Notice that the beam conditions in 2010 did not correspond to the "nominal" situation as the accelerator energy reached 3.5TeV per beam only and it has been filled by a maximum of $\approx$ 400 bunches. To compensate for the lack of statistics, the β^* was tuned to a small value of 2.5m, leading to a larger pile-up reaching up to 2.7 events per crossing at the beginning of some of the machine fills. This tuning permitted to recover part of the missing statistics but the price to pay was more difficult triggering conditions as some additional cuts had to be applied in order to remove too large multiplicity bunch crossings. Moreover, the first level trigger threshold and so the bandwidth sharing favoured muon channels (not so affected by the pile-up) and consequently disfavoured other decays.

1.2 The beam pipe

The LHCb beam pipe (see picture 1.5) is an essential and subtle component of the detector as the reconstruction of the particles is performed up to very high pseudo-rapidity values. It is crucial not to create too many secondary particles in this region where the multiplicity is the largest and a high occupancy at the level of the tracking system or the Cherenkov detectors would reduce their efficiency.

The first three conical segments of the beam pipe, starting from the exit window of the VELO and up to 12 meters along the z axis are made of beryllium which scarcely interacts with the particles produced from the pp collisions, the segments being connected with aluminium bellows. Beryllium being expensive, toxic and the sections difficult to make with this material, stainless steel is used in the next segments, at the level of the calorimeters, where particles are nevertheless supposed to be absorbed but for the muons.

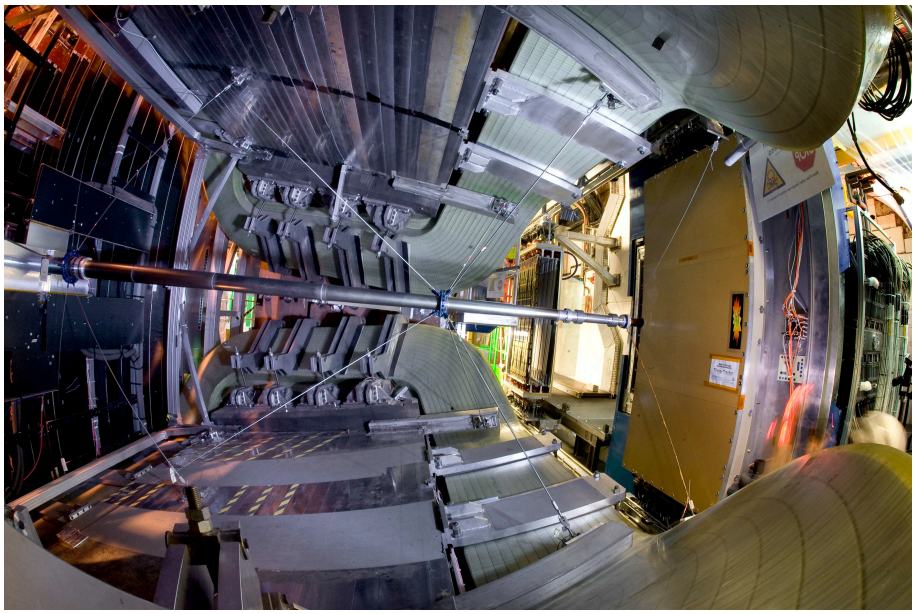

Figure 1.5: Picture of the LHCb beam pipe at the level of the magnet aperture, i.e. between the tracker turicensis (left) and the outer-inner tracking systems (right). The z-axis of figure 1.1 goes here from right to left. The conical sections are visible with the bellows and the supports.

The supports of the beam pipe, visible on picture 1.5, are directly in the detector acceptance. Hence, they have been designed not to affect the particles and are made of a first interface ring of polyimide-graphite followed by an aluminium collar to which are connected eight stainless steel cables and rods pulling altogether upwards and downwards.

1.3 The tracking system

The tracking system of LHCb is composed of the vertex locator (called VELO, see figure 1.6), the tracker turicensis (TT stations, figure 1.8), the magnet, and three tracking stations (called

T1, T2 and T3) made of two parts, the inner and the outer one (figure 1.9). The tracking algorithms are written to connect the hits from the previous sensors and reconstruct the trajectories given the known and imposed magnetic field.

1.3.1 The Vertex Locator

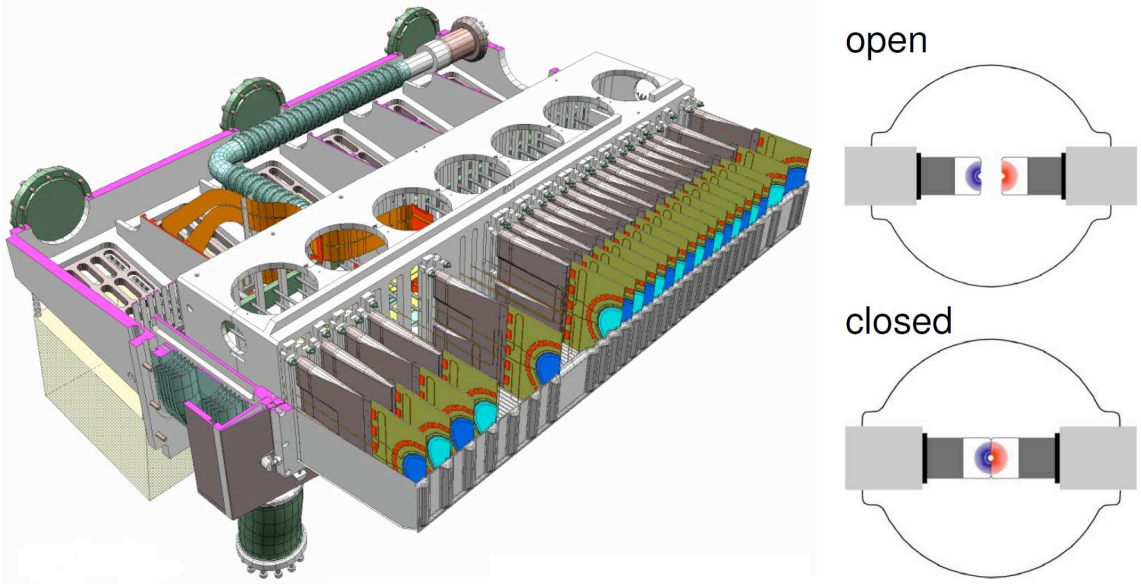

Figure 1.6: Left: Drawing of one half of the VELO. The corrugated aluminium foil is visible at the right of the drawing, just in front of the half disk silicon sensors. Right: The two halves of the VELO are shown both in the open and closed positions, i.e. before and during stable beam conditions of the accelerator.

The VELO [23] which is the first detector seen by the particles and the closest one to the interaction point is probably the most important sub-detector of an experiment dedicated to B physics and in LHCb it is also the most sophisticated one. The purpose of the VELO is to reconstruct the primary and secondary vertices of the pp collisions and of the particles flying both in the forward and the backward directions. The straight trajectories of the charged particles produced are built from hits recorded in the VELO and are furthermore matched to the hits seen in the following tracking chambers. Moreover, two specific sensor layers of the VELO located in the backward region are used for the first level trigger in order to veto pile-up events.

The VELO covers the LHCb acceptance and the z region extending from -50cm up to 1m. It is made of single sided silicon strip sensors of n^+-on-n type (but for one module made of n^+-on-p) located in a secondary vacuum vessel separated from the beam pipe by an aluminium foil. The design and manufacturing of this foil was an important effort as it has to be very thin, corrugated in order to reduce the thickness of material crossed by the incoming particles before they actually see the silicon sensors and to be sufficiently resistant to safely protect the LHC machine vacuum. It also aims at guiding the beam wake-fields and at shielding the VELO

readout electronics (located at the edge of the PCB supporting the silicon sensors) from the radio-frequency pick-up from the proton bunches.

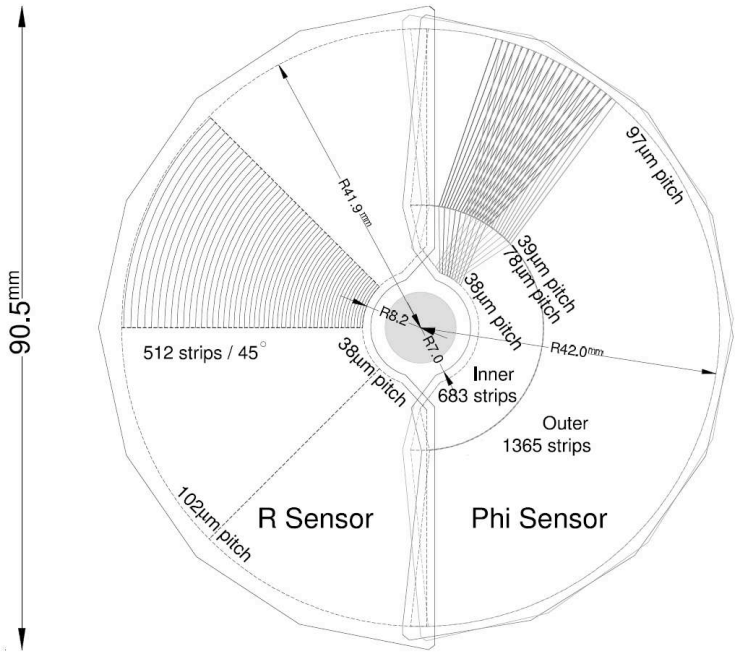

Figure 1.7: Drawing of two facing half VELO stations showing the data-taking condition geometry.

The detector itself is made of two jaws on the right and left of the beam pipe that are retracted to almost 3cm except during stable beam accelerator conditions and data-taking when they are closed to 8mm. Each jaw contains 23 half disk sensors or half stations along the z axis, 2 of those being used for the pile-veto. When closed, the half-stations are slightly displaced by 1.5cm along z in order to fully close the acceptance and leading to a small overlap at the bottom and top of the sensors.

Each half station contains two types of silicon sensors, glued back to back and giving r and ϕ hit locations (see figure 1.7).

The $r-$sensor is made of 512 circular 45° strips centered on the nominal beam position in closed configuration. The division in 45° sectors permits to reduce the occupancy and the strip capacitance. When closed the extreme $r-$sensor strips are at 8.2mm (inside) and 41.9mm (outside) from the beam nominal centre. The strip pitch depends on the radii, from 38μm (inner) to 102μm (outer).

The $\phi-$sensor are made of radial strips divided in two regions with radii extending from 8mm to 17.25mm for the inner part with an angle with respect to the true radial direction of ±20° and from 17.25mm to 41.9mm for the outer part with an angle of ±10°. Notice that the angle of $\phi-$sensors of two consecutive modules are inverted in order to make a stereoscopic reconstruction of the tracks. As for the $r-$ sensors, the pitch varies from 39μm for the inner edge of the 683 inner strips to 97μm at the outer edge of the 1365 outer strips.

1.3.2 The Tracker Turicensis

The tracker turicensis stations [28] are made of two stations of two layers each located at the z position of 2.5m from the nominal interaction point (i.e. just between the first RICH detector and the magnet) and 27cm apart. They cover the full LHCb acceptance, two layers having vertical strip and two layers (one in each station, see figure 1.8) rotated ones with an angle of $\pm 5°$ for $U - V$ spatial reconstruction.

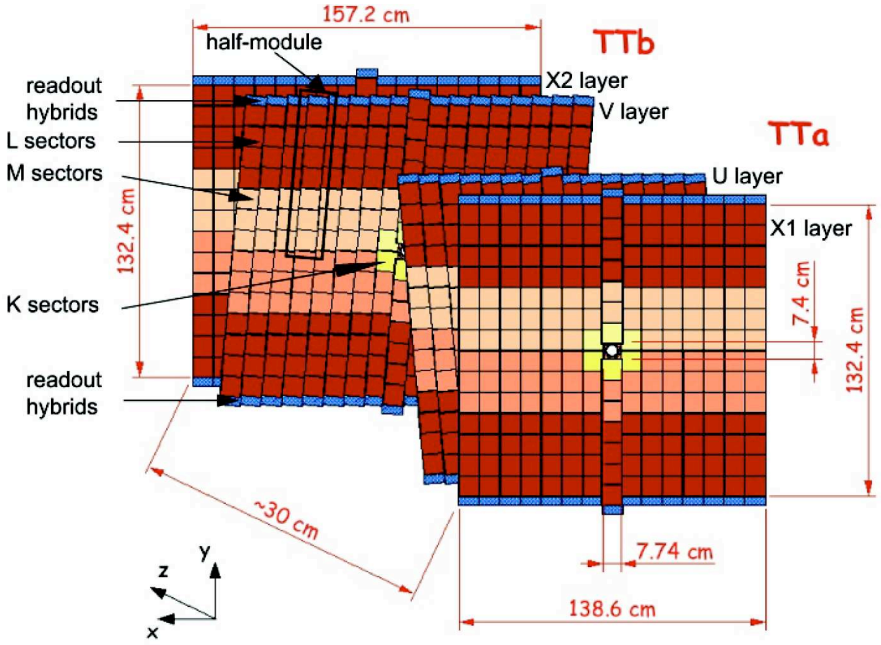

Figure 1.8: The geometry of the two tracker turicensis (TT) stations. The readout hybrids are located at the top and bottom and are shown in blue. The various readout sectors (L, M and K) of the modules are indicated by different colours.

The TT stations have mainly three purposes. First they permit to have intermediate hits between the VELO and the tracking stations located on the other side of the magnet. Without them, connecting the segments would be more difficult, reduce the efficiency and increase the ghost rate.

More specifically, they permit to build tracks from low momentum particles that are swept by the magnetic field, do not reach the tracking stations T1-T3 and would not be reconstructed shouldn't we have intermediate hits. Finally, they give a significant additional information to reconstruct the neutral long-life particles such as K_s^0, that decay outside the VELO volume.

The TT is built from silicon sensors of p^+-on-n type, seven of them making a module, the detector containing 128 of the latter.

1.3.3 The dipole magnet

The $\vec{B}$ field produced by the magnet [19] imposes a curvature to the charged particles which permits to deduce the sign of their charge and their momentum. The largest and best-known

the magnetic field, the better the momentum resolution. The maximum value of $|B|$ is 1.1T along the y axis and at a z position of 4.7m, so that the particles are bent in the $x-z$ plane. The overall integrated field seen from the interaction point is roughly $\int B.dl \approx 4$Tm leading to a momentum resolution of 0.45% up to 200GeV.

The dipole magnet is made of two saddle shape coils mounted inverted on top of each other (see figures 1.1 and 1.5) surrounded by the iron yoke and whose aperture corresponds to the LHCb acceptance. The technology chosen is warm in order to permit a fast ramp-up of the field and a regular inversion of the current and thus of the field orientation. This is of capital importance when looking for asymmetric effects that could be faked by magnet systematics. Inverting the field cancels such experimental problems and reduces the measurement errors.

1.3.4 The tracking chambers

The three tracking stations T1, T2 and T3 are located downstream the particle flow and are made of two parts, an inner one made of a silicon detector [28] and the outer part [22] built from arrays of straw tubes. The purpose of those stations is to complete the track and momentum reconstruction after the magnet bending. The track and hit multiplicity being larger in an ellipse around the beam pipe slightly extended along the x axis (because of the particle curvature), the hit granularity had to be smaller in this region and two very different technologies have been used (figure 1.9).

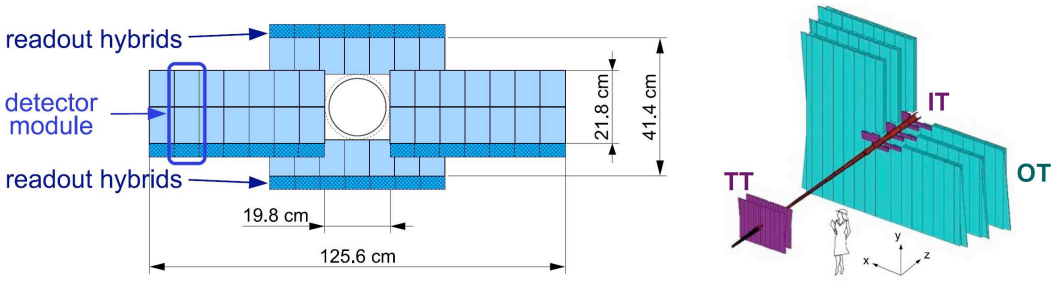

Figure 1.9: Left: the inner part of the tracking stations T1 to T3. Right: the tracking system with the tracker turicensis and the three stations T1, T2 and T3 where the outer region covering the larger part of the acceptance is coloured in blue.

The inner tracker is made of 130k silicon strips of 11 or 22cm depending on the position and covers an area of 4m^2. As for the tracker turicensis, a U-V spatial reconstruction is possible by the orientation of the strips which are vertical, rotated by $\pm 5°$, and vertical again respectively in the four layers of the detector. The silicon sensors used are also of the same type as the TT ones (p^+-on-n) with a pitch of 198μm. As can be see from figure 1.9, the modules slightly overlap in order to permit a precise alignment with particles.

The outer region of the tracking station T1, T2 and T3 are large modules covering a surface of 6.0×4.9m^2 corresponding to the acceptance of the detector and made of four detection layers with the same vertical, $\pm 5°$, vertical tube orientations as the inner part and providing the U-V reconstruction.

As already mentioned, and because of the area to be covered, the technology is very different from the inner detector, the multiplicity allowing a coarser granularity. Each detection layer is composed of two rows of drift tubes of 4.9mm (inner diameter). The gas used is a mixture of Argon (70%), CO_2 (28.5%), O_2 (1.5%) giving a drift time lower that 50ns, but still larger than the theoretical bunch crossing rate and leading to some spillover. There is no read out of the position along the tube and the intrinsic resolution is of 190μm.

1.4 The RICH detectors

Several sub-detectors contribute to the particle identification in LHCb. The calorimeter and the muon system disentangle electrons, photons, hadrons and muons. The various species of hadrons are separated by two Ring-Imaging Cherenkov detectors [20] located on both sides of the magnet called RICH1 and RICH2 (figure 1.10). B physics requires to select exclusive decays of the heavy mesons. The RICH detectors permit to identify specific hadronic decays with a high efficiency and a low contamination. Nevertheless, they usually operate in well-defined momentum range. This is the reason why LHCb has two such devices, specialised in two overlapping momentum ranges.

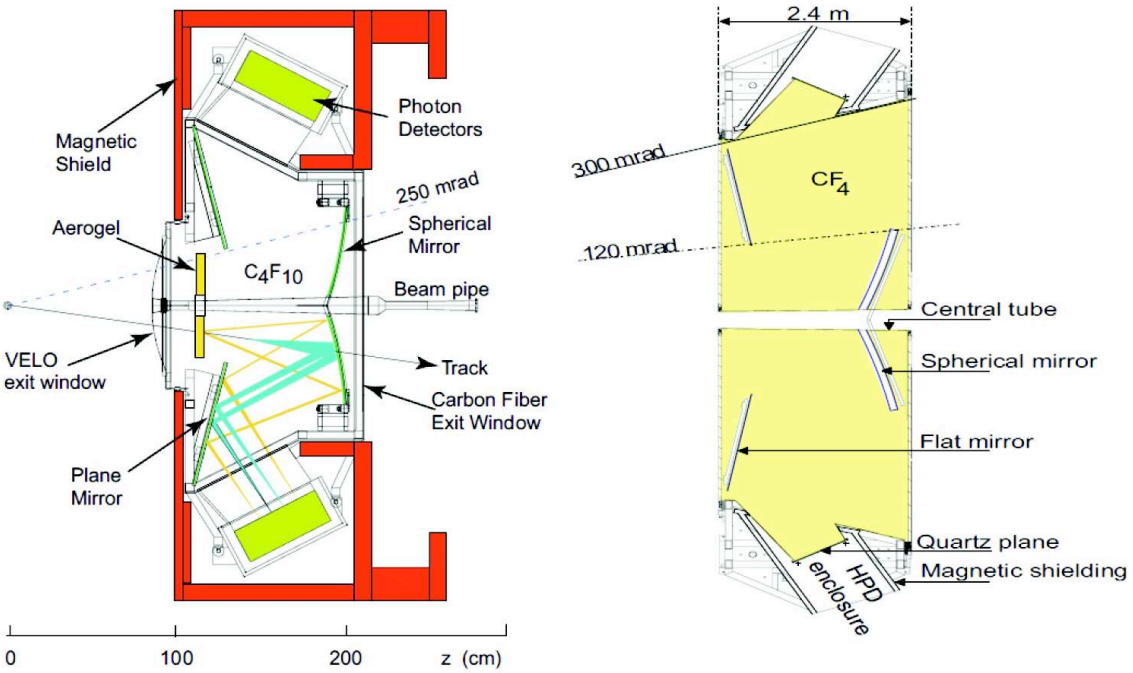

Figure 1.10: Drawing of the two Cherenkov detectors of LHCb. RICH1 (left) and RICH2 (right) are different in term of angular coverage (both drawings are not at the same scale) and momentum operating conditions. The two radiators of RICH1, aerogel (in yellow, close to the entrance window of RICH1) and C_4F_{10} produce two rings centered on the same point after reflection on the mirrors.

The basic principle of the two RICH is the same. The Cherenkov light is focused and extracted from the detector acceptance with a combination of spherical and flat mirrors. In the peripheral region, boxes contain the photo detectors which convert the light into an electrical signal. From the determined radius of the Cherenkov ring reconstructed, the medium index and the momentum of the tracks (obtained from the tracking system, see above), the mass of the particle can be measured and thus its type.

The RICH photo detectors used in LHCb are planes of Hybrid Photon Detectors (HPD) having 1024 pixels each for a granularity of $2.5 \times 2.5\text{mm}^2$ and providing a measurement every 25ns. The two RICH are very different in term of

- angular acceptance,
- operation momentum range.

RICH1 looks at the full LHCb acceptance in a momentum range from low values up to 60GeV. This is possible by using two radiator, aerogel ($n = 1.03$, up to 10GeV) and C_4F_{10} ($n = 1.0014$, from 10GeV to 60GeV). Hence each track produces in RICH1 two rings of different radii centered on the same point. RICH2 is specialised in the identification of particles whose momentum exceeds 15GeV up to 100GeV and consequently whose pseudo-rapidity is rather large. Hence, the angular coverage of RICH2 does not extend farther than 120mrad, i.e. half the LHCb angular acceptance, and the tank of the detector contains CF_4 ($n = 1.0005$). The specificities of the radiators is given on figure 1.11.

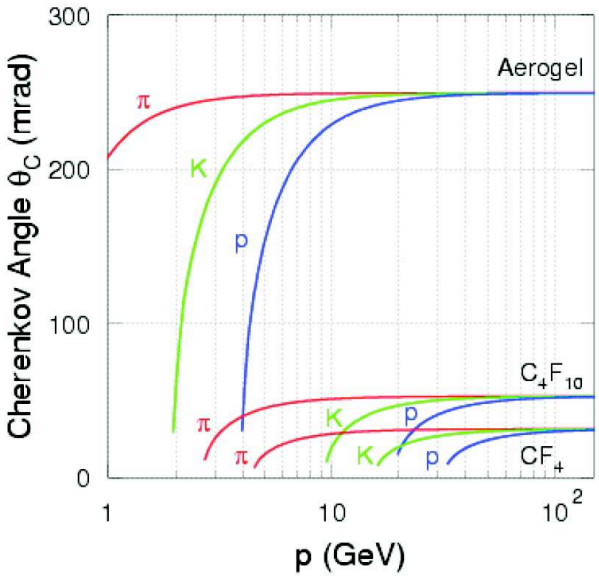

Figure 1.11: Cherenkov cone aperture with respect to the momentum of the particle and for the three radiators used in the two RICH detectors of LHCb.

The theoretical angular dispersion in the three radiators is 2.6, 1.5 and 0.7mrad respectively in the aerogel, C_4F_{10} and CF_4. Nevertheless, at LHCb start-up the performances of the aerogel were rather at the level of 5mrad. This seemed partly to be due to dispersions between aerogel

tiles. Performing individual tile calibrations improved the resolution without yet reaching the expected value.

The two RICH and especially RICH1 are located close to the magnet and the HPD have to be shielded against the magnetic field, in order no to distort the image reconstructed on the pixel chip. Boxes have been designed to protect the HPD with the constraint of not affecting the magnetic field map in the detector acceptance.

1.5 The calorimeters

This document focuses on some specific aspects of the calorimeters that will be described mostly in the next chapters. The reader will only find here a brief introduction to the calorimeter system and should either look at references [59] or at the following sections if details are needed.

The four calorimeters are wall-like structures divided in two halves which may be open and fully taken out of the acceptance. The first calorimeters seen by the particles incoming from the interaction point are the scintillating pad detector (SPD) and the preshower (PRS) which are followed by the electromagnetic (ECAL) and the hadronic (HCAL) calorimeters (see figure 1.12).

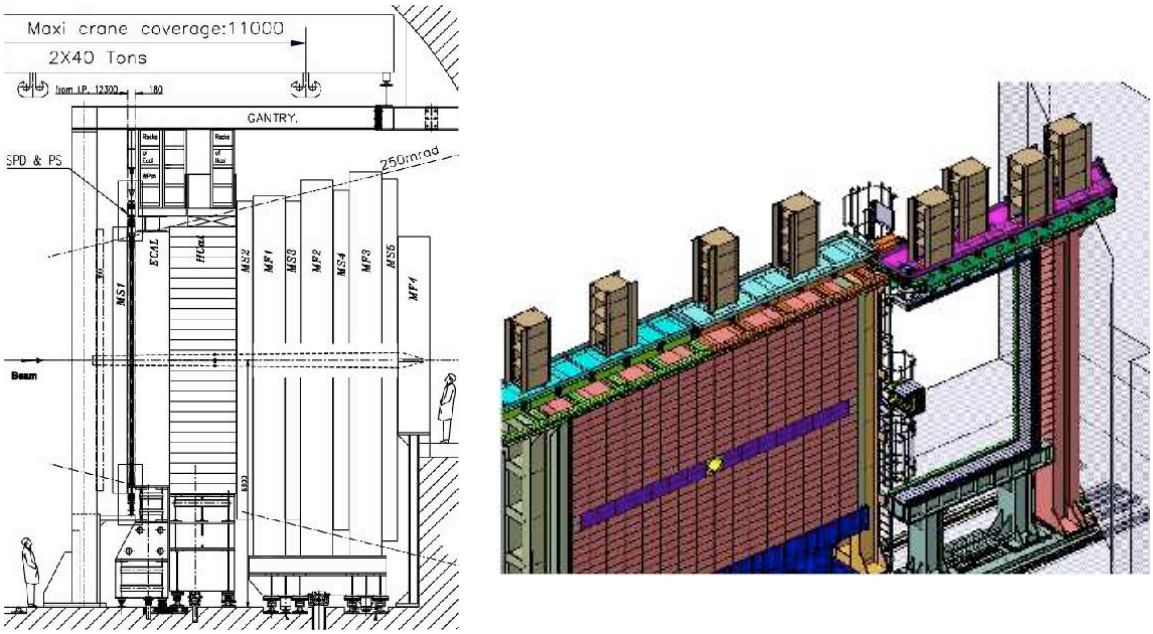

Figure 1.12: Left: the wall like structure of the calorimeters is easily recognized between the M1 and M2 muon chambers (here indicated by "MS1" and "MS2" for muon stations 1 and 2). Right: This drawing shows the calorimeter system partially open and shows the location of the electronics crates on the platform above the detector.

The readout electronics that is an important topic of this document is located mainly on the platform above the sub-detectors where a narrow passage permits to access the crates.

The identification capabilities and disentangling of electrons, photons and hadrons by the calorimeter system comes from crossing the information from the SPD, PRS, ECAL and HCAL.

Sub-detector	SPD/PRS	ECAL	HCAL
Number of channels	6016 each	6016	1488
Lateral size	6.2×7.6 m^2	6.3×7.8 m^2	6.8×8.4 m^2
Longitudinal depth	180mm - $2.5X^0$ - $0.1\lambda_I$	$25X^0$ - $1.1\lambda_I$	$5.6\lambda_I$
Basic requirement	20/30 photo-electrons per MIP	$10\%/\sqrt{E} \oplus 1.5\%$ (E in GeV)	$80\%/\sqrt{E} \oplus 10\%$ (E in GeV)
Dynamic range	0-100 MIPs - 1 bit (SPD), 10 bits (PRS)	0-10 GeV E_T	0-10 GeV E_T

Table 1.1: The requirements to the LHCb calorimeter system.

The SPD threshold is set so that only charged particles give a hit. The preshower being located after a lead absorber measures a sizable energy deposit for electrons and photons. The ECAL fully absorbs the electromagnetic particles (photons and electrons) while the hadrons are mainly absorbed by the HCAL.

1.5.1 The scintillating pad detector and the preshower

The design of the SPD and PRS [64, 63] are very similar and consists of two scintillating vertical planes made of 6016 pads. A 2.5 radiation length lead sheet is sandwiched between the two sub-detectors. This lead converter allows to initiate the electromagnetic showers so that electrons and photons deposit a sizable amount of energy in the PRS. Charged particles leave in the SPD a minimum ionising particle (mip) signal which is detected while photons do not interact. Combining the SPD and the PRS information with the cluster position reconstruction of the ECAL gives a determination of the nature of the electromagnetic particle interacting with the calorimeter system. This technique is used offline but also at the first level trigger of LHCb to tag high transverse momentum hadron, electron, photon and pion candidates, characterising a high mass B meson decay. Table 1.1 gives the main requirements to the LHCb calorimeter system. The PRS and SPD have a segmentation that varies with respect to the distance to the beam pipe, the cell sizes matching the ECAL cell size in order to make a projective system pointing to the LHC beam collision. The SPD/PRS cells are scintillator pads grooved and holding an helicoidal wavelength shifting fibre (WLS) as showed on picture 1.13. The light is propagated by clear fibres to multi-anode photomultipliers (MAPMT) located in boxes above and below the SPD/PRS walls and containing the very front-end electronics in charge of the shaping and for the SPD only, also of the sampling of the signal [48].

The SPD very front-end [49] provides to the front-end electronics a binary information corresponding to the amplification and integration of the charges collected from the MAPMT. After pedestal subtraction and spillover correction, the signal is compared with a threshold loaded by the slow control of the experiment. The output of this comparison is sent to the front-end electronics on a differential line.

The PRS has an energy range of 100 mips. The signal of its MAPMT is also shaped and integrated on the very front-end. But unlike the SPD, the differential analog output is sent on 27 m long twisted pairs to the PRS front-end boards housing a 10 bit ADC where the pedestal, spill-over and integrator gain corrections are applied.

Both the SPD and PRS rely on a similar technique to measure the MAPMT signal and based on two parallel interleaved integrators running at 20MHz per channel, one being read out and reset while the other is integrating the pulse.

The overall performances of the SPD and PRS system have been determined during the

Figure 1.13: Picture of a SPD/PRS scintillating pad with its wavelength shifting fibre (WLS fibre) capturing the light produced. The WLS fibre is connected to a clear fibre that propagates the light to the very front-end located at the top or bottom of the SPD and PRS walls. A multi-anode photomultiplier is visible at the right of the picture.

commissioning of the detectors that took place before and during LHC start-up and are fully satisfactory. The noise is estimated to be of the order of 3mV for the former (a mip producing 100mV in average). The noise of the PRS is reduced to 1.2 ADC count (a mip corresponding to 10 ADC counts[2]) [65]. Its pedestal is centered at 140 ADC counts with a maximum of 300 saving the expected dynamic range. The SPD and PRS detectors are built around a very front-end and a front-end which are located from 20 to 30 meters apart. This leads to stringent timing constraints on the design and to the integration of degrees of freedom to compensate for the cable lengths and accurately sample the signals at the level of the front-end boards.

1.5.2 The electromagnetic and hadronic calorimeters

The characteristics of the ECAL and HCAL sub-systems are quoted in table 1.1.

The ECAL [61, 36] and HCAL [3, 10] are two wall-like calorimeters with a variable segmentation that fits the particle multiplicity. They have both the same electronics that is described in the next chapters, the main difference between those detectors is in the design of the modules. The ECAL is a shashlik system, each module consisting of 66 layers of scintillator (4mm) and lead (2 mm) corresponding to one, four and nine cells of 12×12 cm^2, 6×6 cm^2 and 4×4 cm^2 respectively in the outer, middle and inner areas defined by the distance of the cells to the beam pipe (figure 1.14 and 1.15). To fully contain the electromagnetic shower the ECAL is $25X_0$ thick.

The HCAL is made of 26 modules of iron and scintillator tiles piled-up (see figure 1.16). Like the ECAL, the light produced is also transported by WLS fibres but readout only by 1488

[2]This corresponds to the nominal design. During the commissioning and the first data taking period, the mip was set first at 20 ADC counts so that it count be clearly seen. The relative calibration of the cells was easier. The absolute calibration of the SPD, i.e. the conversion from the number of ADC counts to the overall energy deposited in the PRS scintillator and the absorber is the subject of the last part of this document.

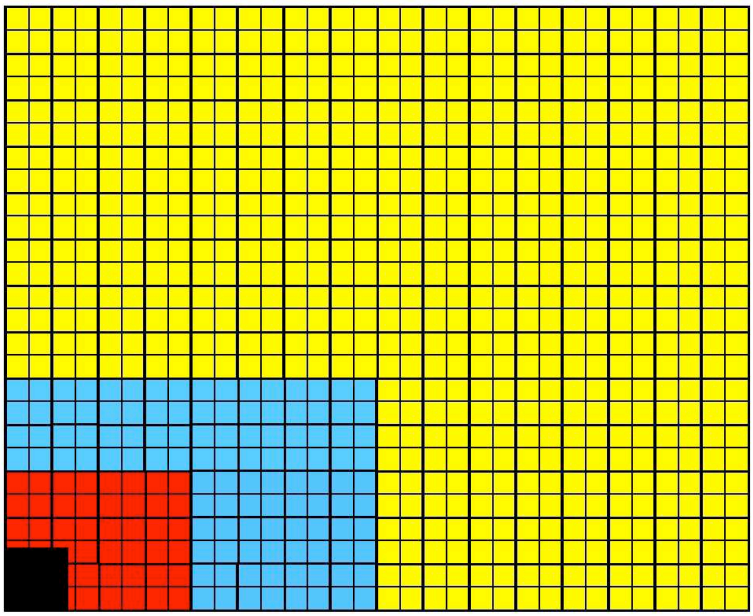

Figure 1.14: The plot shows the separation among the different ECAL granularity regions on a quarter of electromagnetic calorimeter. In yellow, the outer region, in blue the middle and in red the inner one. The size of the cells is respectively 12×12, 6×6 and $4 \times 4\text{cm}^2$ as shown on figure 1.15.

photomultipliers dividing the detector in cells of 26.2×26.2 cm^2 or 13.1×13.1 cm^2 in the outer and inner regions respectively, the previously defined ECAL middle zone being merged here with the inner one. WLS fibres cross longitudinally the modules of the ECAL and HCAL to collect and propagate the scintillator light to photomultipliers powered by Cockcroft-Walton bases [34]. Both, the ECAL and HCAL PM high voltages are adjusted so that the measurement is directly performed in transverse energy, which is the most relevant quantity to trigger on.

The HCAL has an interaction length of $5.6\lambda_I$ due to the 1.2m long master iron plates interlaced by six 4mm thick spacer iron plates. In between the absorbers, scintillator tiles are introduced and produce the light collected by the WLS fibres (see figure 1.16, right).

1.6 The muon chambers

The muon stations [21] are supposed to detect what has not yet been absorbed by the other sub-detectors, i.e. the muons which have a large penetration power. Hence, it is located at the end of the LHCb spectrometer, just before the cavern wall (figure 1.17).

Five stations compose the system, one just before the SPD scintillator layer and called M1, the four others after the hadronic calorimeter and interleaved with thick absorber walls of iron of 80cm.

M1 is not only specific because of its location. Contrary to the others it is built from Gaseous Electron Multiplier (GEM) detectors because of the occupancy and radiations in the

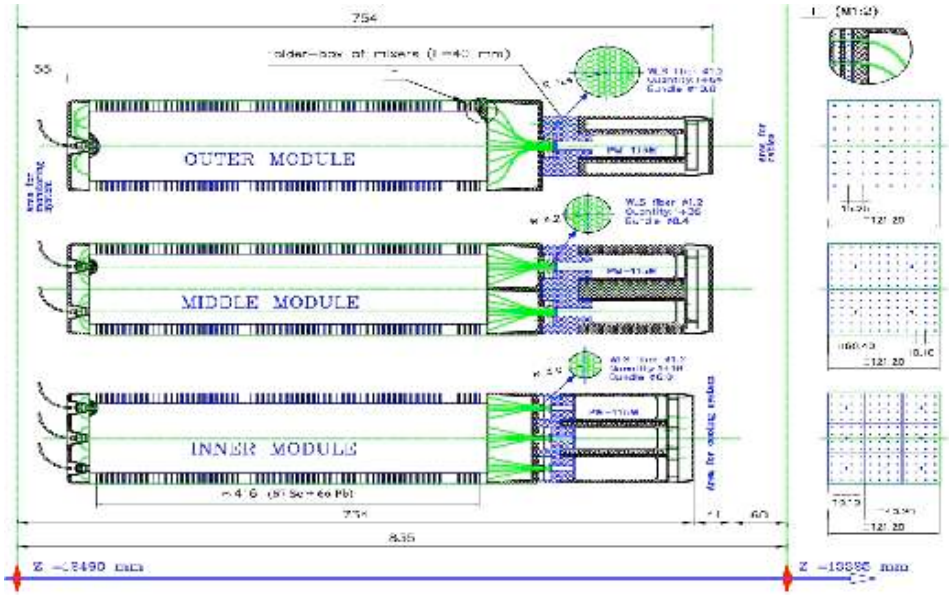

Figure 1.15: The drawing shows the ECAL cells corresponding to the inner region (lower modules containing 9 cells and red area on figure 1.14), the middle region (4 cells per module, blue area on 1.14) and outer region (a single cell per module, yellow on 1.14). The disposition of the cells on the drawings is such that the particles come from the left, the PMT being located at the back of the modules.

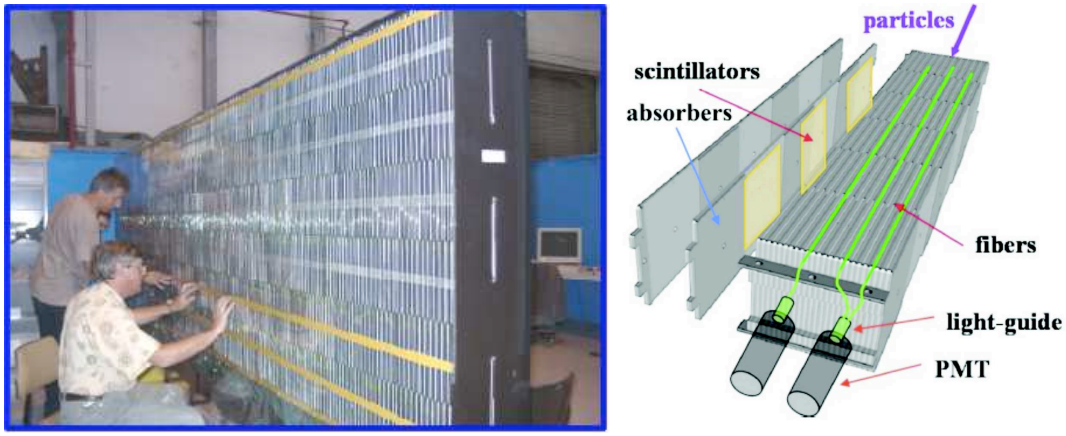

Figure 1.16: Left: the picture shows the manufacturing of a HCAL module. According to the module orientation, the particles would originate from the top on the picture, the light being propagated from the tiles to the PMT located at the bottom. The 26 modules are piled-up horizontally to build the hadronic calorimeter wall. Right: design of a HCAL module the long iron master plates support the absorbers and the introduced scintillators pads.

corresponding region while M2, 3, 4 and M5 are equipped with multi-wire proportional chambers (MWPC).

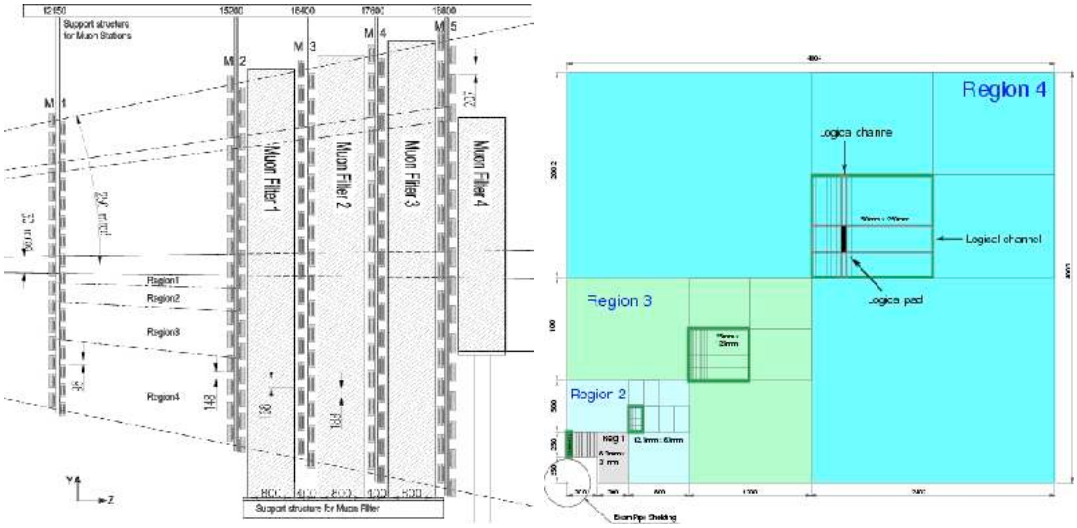

Figure 1.17: Left: profile view of the muon system. In between M1 and M2 is the space for the calorimeter system. Right: the sharing among the 4 regions of the muon chambers.

As for the calorimeter system, the muon chamber are divided in regions of different granularities leading to similar occupancies over the detector acceptance. Thus, the spatial resolution decreases when looking at larger angular aperture with respect to the beam pipe, but those regions also correspond to the larger multiple scattering effect making spatial requirements not so crucial here.

Notice on figure 1.17, left, the iron filter 4 which is designed to shield LHCb from the LHC machine background.

1.7 The LHCb trigger and acquisition

The purpose of any trigger is to reject the background or not interesting events while keeping the signal. At LHCb, in nominal conditions (which are not what was experienced during the year 2010) and a luminosity of $2 \times 10^{32}\text{cm}^{-2}\text{s}^{-1}$, the inelastic pp collision rate reaches 16MHz, that is reduced to 12MHz if considering events containing at least 2 "reconstructible" charged tracks. Only 100kHz consists of signal or $b\bar{b}$ events.

The trigger [24] aims at removing the large background fraction and preserving the useful kHz of B events. It operates at two levels, the first one (called L0) is implemented in custom-made electronics and is based on the information of the calorimeter, muon and pile-up veto systems and relies on the fact that single objects pass for example P_t thresholds (except for di-muon criteria where several objects are considered). The L0 output rate is limited to 1.1MHz which is the limit of the acquisition bandwidth. The L0 latency before the decision is propagated back to the front-end is set to 160 bunch crossing or 4μs.

If a L0 decision yes is made, the front-end electronics of the sub-detectors sends all the data through optical fibres to the so-called TELL1 boards (apart from the RICH that depends on a similar hardware) located in the counting room and which are the interfaces between the

sub-systems and the entry point to the PC farm that performs both the second level trigger and the acquisition and that should contain ultimately 16000 CPU cores.

We already saw that the TELL1 boards receive the data from optical fibres. They also receive from the fast control of the experiment (that sends the L0 signal) a destination address or the id of the computer to which they should transmit the data. All the TELL1 of the counting room build synchronously a packet of events (multi-events packet or MEP, usually ten consecutive L0 triggered events) containing exactly the same bunch crossing sequences and send it to the destination address through a switch. Hence, each PC of the farm receives several blocks of identical event sequences corresponding to different parts of the detector.

The second level trigger is done in two consecutive sub-levels (HTL1 and HLT2) which are C++ applications running sequentially [26, 25]. The HLT1 mainly aims at confirming the L0 decision by using the L0 objects and adding the VELO and tracking station information in the corresponding regions of interest to refine the reconstruction. Several "alleys" are defined corresponding to the specific L0 objects confirmed and new selection criteria are applied on the better evaluated momentum, on the tracks impact parameters or the secondary vertex displacement [60, 33, 72]. The HLT1 output rate is of the order of 30kHZ, the bandwidth sharing among the alleys being easily tunable.

At 30kHz, it is now possible to perform a global reconstruction of the events which is the first task of the HLT2 level. Of course, the same PC will run sequentially the HLT1 and the HLT2, so that no exchange of data in the farm is needed. The HLT2 consists of a set of algorithms trying to identify either an inclusive or an exclusive decay. Exclusive selections in HLT2 are usually very similar to the offline selections. If one of those algorithms selects an events, it is kept and stored on disk. The output rate of the HLT2 is of 2kHz. Considering that an event is 35kB on average, the output is of 70MBs^{-1}. When a PC has finished processing a set of blocks corresponding to a MEP, the fast control of the experiment gets the information and puts the computer back on the list of machines that are potential destination addresses for the TELL1 data.

The trigger of LHCb was used in 2010 in a rather unexpected way. As was already mentioned and in order to compensate for the lack of statistics due to the small number of bunches in the machine, the focusing of the beam was such that it became acceptable to have several events per crossing. In those conditions, the pile-up veto was not used. Nevertheless, multiple interaction events swallowing a large bandwidth or leading to an unacceptable processing time in the farm could not be used. Hence, Global Event Cuts (GEC) have been defined from threshold on quantities like the number of hits in the SPD or the number of hits in the VELO. The events failing those GEC are rejected.

Part I

The electromagnetic and hadronic calorimeter electronics

The LHCb electromagnetic and hadronic front-end electronics is based on two types of boards. The front-end board (FEB) and the calorimeter readout board (CROC) that will be described in the next chapters. The former are in charge of capturing, shaping and integrating the signal from the photomultipliers (PMT). An ADC converts the voltage corresponding to the integration of the pulse to a 12 bits value sent to a first stage processing FPGA[3] (called Fe-PGA for Front-End PGA). This treatment is performed on groups of 4 channels, each board receiving signals from 32 PMT. The Fe-PGA removes the pedestal, stores the 12 data bits results in a circular RAM and evaluates the trigger information on 8 bits.

The first level trigger (L0) processing [16] is locally performed on a dedicated PGA on the board [42] (Trig-PGA)[4]. The L0, at the calorimeter level, is based on a sequence of selections [24]. The first parameter looked at is the transverse energy deposited in 2×2 cells of the ECAL and HCAL. The selection of the largest E_t candidate is done by the Trig-PGA on each FEB and is sent to a Trigger Validation Board (or TVB, which has been designed by the Annecy group, one board being located in each half of the ECAL crates and receives the information from several FEB) where 4 cases are defined, photon, π^0, electron and hadron, according to the coincidences of the signals in the projective cells of the SPD, PRS, ECAL and HCAL. Each TVB keeps a single candidate per type (after adding the ECAL contribution to the HCAL P_t of the hadron candidate) and sends it to the last calorimeter specific stage of the trigger processing, the selection board, which finally keeps the higher E_t candidate per type for the full calorimeter. The decision is made by applying cuts on the transverse energy of the filtered deposits and by combining the information from the muon system and the pile-up veto.

The L0 decision is propagated back to the front-end electronics through the Trigger and Timing Control system of LHCb (TTC), then to the calorimeter readout board (CROC) located in the middle slot of each calorimeter crate (SPD/PS, ECAL and HCAL), to the backplane and finally to the front-end boards. Then, the data stored in the circular RAM of the Fe-PGA are sent to another PGA called sequencer (Seq-PGA) which gathers the data from the 8 Fe-PGA. The events are built with a specific format and on 34 words which are serialised and sent through the backplane to the CROC. The last stage is the processing of the CROC which propagates the data to the optical emitters, performs the fibre synchronisation, checks the conformity of the data and provides evolved debugging capabilities.

The FEB and CROC will be described in the first two sections of this part. The performances will also be given.

The front-end electronics is localized on a platform above the calorimeter system. The radiation levels received in this region are large compared to the standard radiation levels received in most previous high energy physics experiments and it was necessary to select specific components and to test them in beams. This was done and the third chapter will report on some of the methods and on the results obtained.

[3]FPGA means Field-Programmable Gate Array. This is an integrated circuit whom logic may be programmed by the user. The code is loaded into the component either at each power on (the most common situation), with a specific tool but as many times as needed (this is the case of the APA flash components from Actel mentioned later on) or only once (case of the AX FPGA from Actel used on the front-end boards and based on the anti-fuse technology).

[4]Not described in this document.

Chapter 2

The front-end board

Contents

2.1 General overview 31
2.2 The Analog part of the front-end board. 32
2.2.1 Description 32
2.2.2 Characterisation of the shaper 35
2.2.3 ADC levels 38
2.3 The Digital part of the front-end board 39
2.3.1 The front-end PGA 40
2.3.2 The sequencer 44
2.4 Test beams results 46
2.4.1 Sampling window 47
2.4.2 Linearity 48
2.4.3 Noise 48
2.4.4 Crosstalk 49

2.1 General overview

The front-end boards of the LHCb ECAL and HCAL [43] are identical. Each FEB receives at its input connectors, the signal of 32 PMT from coaxial cables of different length. The FEB should acquire the signal, shape it, integrate it in order to get a measurement of the transverse energy deposited in the calorimeter cells (the gain of the PMT is tuned so that the charge is proportional to $E \times \sin\theta$). This is done by the input stage of the FEB which is built around an analog shaper designed at the Laboratoire de l'Accélérateur Linéaire (LAL). The details of the conception of the shaper can be found at [32]. The digital part is based on an ADC to convert the shaper output in a 12 bit word and performs the numerical manipulations of the signal in several FPGA.

Figure 2.1 shows the different parts of the front-end board.

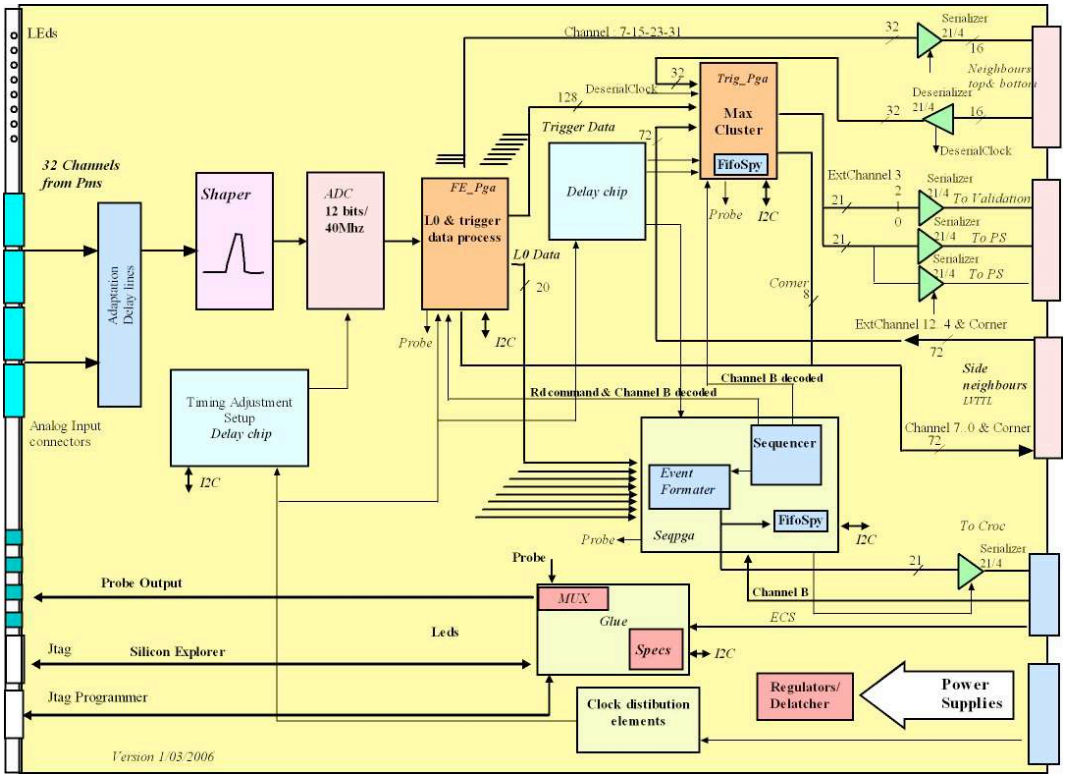

Figure 2.1: The design of the FEB of the ECAL and HCAL systems. At the top left, the input connectors are visible and feed the analog part of the FEB (shaper and ADC). The FE-PGA processing follows, then the system is divided in two activities: the trigger operations, right top, and the acquisition of the data at 1MHz, below. The bottom part of the figure shows the slow control of the FEB.

2.2 The Analog part of the front-end board.

2.2.1 Description

The signal from the photomultipliers is characterized by a rising time of less than 5ns. The decay is longer than the allowed sampling interval of 25ns, the separation between two bunch crossings. This is due to the added effects of the size of the region of the shower, the scintillator decay, the fibre light propagation (each ECAL fiber runs twice though the modules so that the light propagates directly to the PMT and in the other direction goes first towards the front of the module, travels in a loop before heading to the PMT at the back of the modules [59]), the PMT signal conversion (whose time depends on the applied high voltage). Hence, the signal has to be shaped in order to reduce it to the 25ns window. A clipping is done at the level of the PMT base either with a 5ns delay line for the ECAL (see figure 2.2) or by a cable on the HCAL base where the space limitations are not so constraining. This clipping reduces the decay length by injecting on the cable the inverted signal with a delay of 10ns. The resulting pulse is narrower and shows a tail of less than 2% after 25ns. A coaxial cable transports the signal from the PMT base to the calorimeter front-end electronics located above the detector

on a platform perpendicular to the beam axis. The front-end boards are plugged into 14 crates for the ECAL and 4 for the HCAL. Each crate contains from 12 to 16 boards, each one treating the signals from 32 channels. The first processing stage of the front-end board is performed by

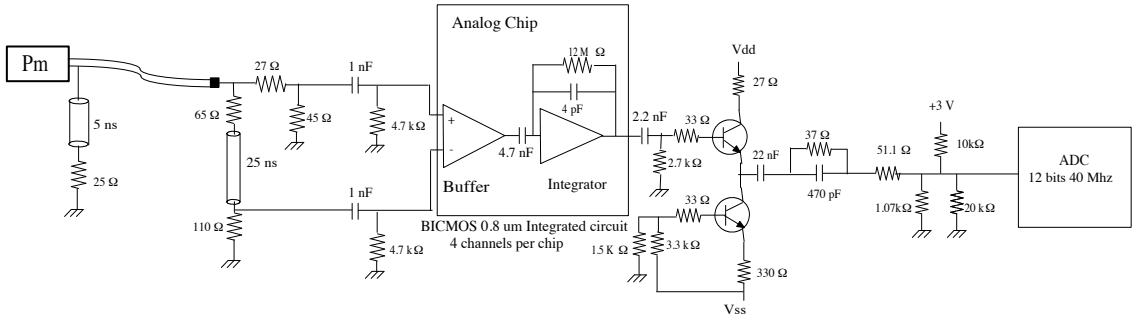

Figure 2.2: Schematics of the analog part of the front-end electronics. From left to right, the signal is produced at the cell level by the photomultiplier. After the clipping, it is transported to the front-end board where it is split in two paths feeding the differential inputs of a buffer stage. The integrator performs the energy measurement which is sampled by the ADC.

the analog electronics. It is build around two main components:

- The integrator that measures the area of the pulse, area which is proportional to the energy deposited in the calorimeter module. This is an ASIC built at LAL.
- The 12 bits flash ADC running at 40MHz from Analog Device (AD9042).

The shaper will be briefly described here, its characterisation will be more deeply covered [32].

The maximum current expected from the PMT is of 20mA on 25Ω. The ADC working range is 1V with an input impedance of 250Ω. Apart from those external constraints, the shaper should cope with the overall detector requirements:

- The noise of the integrator itself should be limited to 1ADC count, which corresponds to 250μV at the ADC input or to $E_t = 2.5MeV$ after reconstruction as the dynamic of the ECAL is roughly of 10GeV on 12 bits. The ADC noise will also contribute, as will be seen later.
- The linearity of the shaper should be at the 2% level over the full dynamic range.
- It was already pointed out that the residue or spillover after 25ns should be less than 2%.
- To be comfortable, the sampling region should be stable (flat) on a range of ±2ns.
- The channel crosstalk should be limited below 1%.

Some of those criteria have been obtained from physics channels, for example $B \to K^{\star}\gamma$, where the purpose was to have statistical and constant terms of the same amplitude at the average P_t of the photons of this decay. With such constraints the most significant effects on the resolution do not come from the electronics.

Notice that the clipping performed before the integrator processing removes a fraction evaluated to 60% of the photo-electrons collected by the PMT. The amount of photo-electrons delivered by the ECAL and HCAL is of the order of 3000 and 100 per GeV, respectively. The 60% statistics reduction should not lead to a significant fluctuation with respect to the full signal integration.

The integration of the signal is performed with a capacitor of 4pF. The obvious difficulty comes from the fact that before any new measurement the charges have to be removed from the capacitor. A switch system connecting the capacitor to the ground could empty it. But, it would necessarily induce a dead-time and the switch itself may inject unwanted charges which could lead to a drift of the integrator or to a pedestal hard to remove. The first problem (dead-time) is usually solved by using two interleaved integrators running at 20MHz, one integrating while the other is read and reset. This is what is done in the PS/SPD very-front-end electronics.

Another solution was applied here that solves the two problems. But, it requires the usage of a differential input stage that removes linearly the signal to itself after a delay of 25ns. This can be seen from the left and center parts of figure 2.2 where the signal is split in two branches, one passing through a 25ns delay line (model EP123146 from PCA electronics, 25ns $\pm$ 0.5ns delay on 100Ω). The adaptation of the signal to the coaxial cable impedance is indicated at this level on figure 2.2. The two branches feed a differential buffer that aims at subtracting the two signals during integration and also at adapting the input current from the PMT to the small value of the integrator capacitor that will follow. The DC level is removed at the output of the buffer by the 4.7nF capacitor before the signal is captured by the integrator. Notice that a large value resistor is connected in parallel to the integration capacitor in order to fix the DC level at the input of the integrator. The overall decay time of the integrator is of $\approx 2\mu$s, long with respect to the integration frequency. It is partly due to the integrator capacitor of 4pF and the output resistor of 2kΩ located at the buffer output (not represented on figure 2.2).

The resulting integrated signal is a rising pulse corresponding to the integration of the signal that lasts for $\approx$ 22ns followed by a plateau of $\approx$ 4ns, then the integration of the inverted polarity resets the integrator to 0 in $\approx$ 25ns. Of course the sampling of the ADC should be on the plateau in order to

- fully measure the signal,
- have a stable measurement independent of any inevitable clock jitter.

The shaper output stage contains an emitter follower that permits to feed the low impedance input stage of the ADC of 300Ω, a resistor of 51Ω being used to reduce the gain of the system and 250Ω coming from the ADC input impedance.

Finally, the 1.07kΩ inserted before the ADC aims at setting the baseline at about 128 ADC counts. This allows negative fluctuations of the pedestal with a sufficient margin of 128 counts. Two other resistors of 10kΩ and 20kΩ (not showed on figure 2.2) connected respectively to the +3V and the ground, have been mounted. They have no effect but to shift this pedestal by 100 ADC counts. Indeed, the 250Ω input impedance of the ADC is subject to fluctuations from production and this may have an effect on the baseline leading to a possible reduction of the 128 ADC count margin. Removing one of the two resistors would permit to adjust this baseline during the test of the front-end boards.

2.2.2 Characterisation of the shaper

Linearity

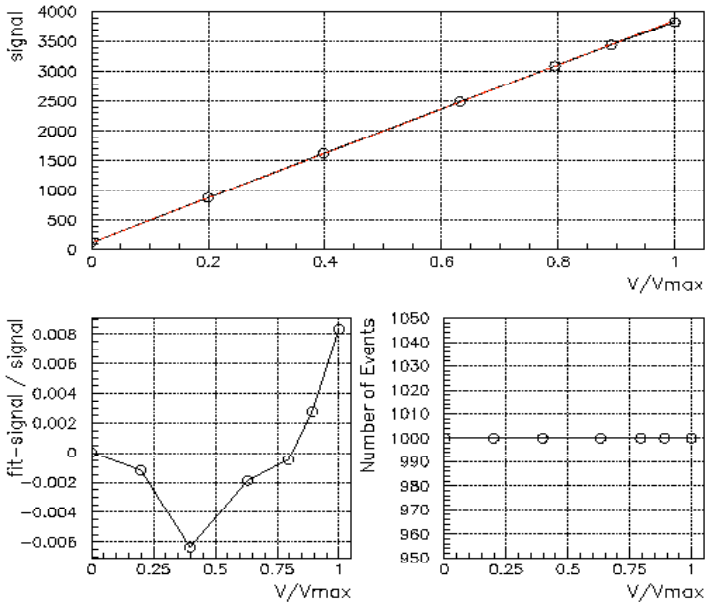

Figure 2.3: The shaper linearity on the full ADC dynamic range. The top plot shows the measured signal versus the attenuation applied on the signal input and the linear fit which is perfomed. The bottom left plot is the departure from the perfect linearity. At the bottom left the statistics per data point is indicated.

The shaper has been tested with respect to the important criteria already mentioned (noise, linearity, crosstalk, etc...). The linearity has been measured in test bench with a precise attenuator. The original pulse is reduced in amplitude and the attenuation in dB is compared to the ADC output. The linearity is obtained from a linear fit of the signal amplitude with respect to the selected attenuations and is evaluated by (fit−signal)/signal. Figure 2.3 shows the result and correct behaviour of the shaper-ADC system over the full dynamics which remains in the $\pm 1\%$ limits.

Crosstalk

The ASIC produced from the schematics of figure 2.2 contains 4 identical channels which become the basic unit both for the analog and a large fraction of the digital part of the FEB (a Fe-PGA deals with the 4 shaper outputs). The crosstalk was extracted by pulsing a channel of the shaper and measuring the output on the others. It was very reproducible among the various combinations and mostly below 0.5% as can be seen from the plots of figure 2.4. Here,

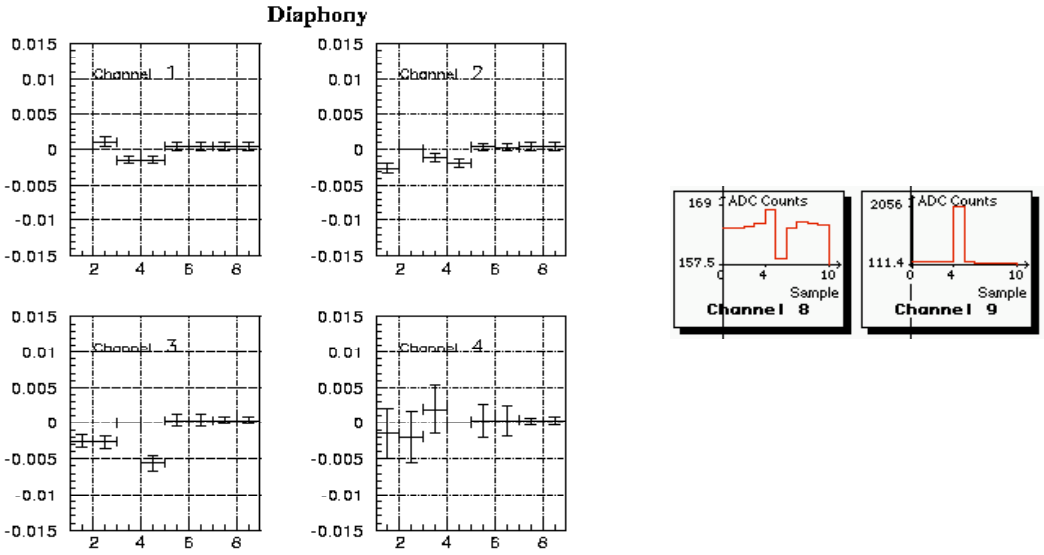

Figure 2.4: The four left plots show the measured crosstalk between the 4 channels of a shaper as measured on a test bench. The two right plots show the raw pedestal of a channel (here, number 8) when another one (channel 9) is pulsed with a 2000 ADC counts signal.

the four left plots show the fraction of the signal injected on one channel and seen by the 3 others of the shaper and 4 other channels of the neighbouring shaper of a prototype board that contains 4 copies. Nevertheless, a specific combination involving channels 3 and 4 led at first to a larger crosstalk than expected (of the order of 1.5%). This problem was identified as due to an inevitable crossing of an integrator output with a channel input and was cured by reducing the metal path width in order to reduce the capacitance effect. Figure 2.4 was made after correction and shows that this specific combination was back below 1%.

Noise

The noise was studied by extracting its coherent and incoherent contributions from a large sample of empty events recorded on the channels of the shaper. Two quantities called here A and B have been measured,

$$A = \sum_{j}^{m \text{ events}} \left(\sum_{i}^{n \text{ channels}} x_{ij} - \bar{x} \right)^2 = m \left(n^2 \sigma_{\text{coh}}^2 + n \sigma_{\text{incoh}}^2 \right) \tag{2.1}$$

$$B = \sum_{j}^{m \text{ events}} \sum_{i}^{n \text{ channels}} (x_{ij} - \bar{x})^2 = m \times n \left(\sigma_{\text{coh}}^2 + \sigma_{\text{incoh}}^2 \right) \tag{2.2}$$

Solving σ_{coh} and σ_{incoh} from the extraction of A and B of equations 2.1 and 2.2 disentangle the effects.

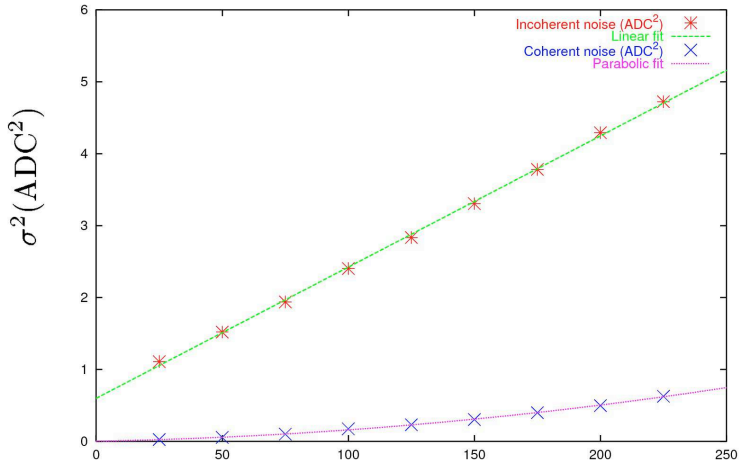

Figure 2.5: The analog electronics (shaper and ADC) noise measured with its coherent and incoherent contributions. The noise effect is showed with respect to the effective integration time window in ns, the electronics providing a measurement every 25ns.

The two noise contributions have also been studied in $n \times 25$ns time windows, in order to obtain the effective integration time effect on the noise. The method used consisted, for a specific time window of for example 50ns, to remove by software the integrated signal captured 75 ns before. This was possible as the digital firmware was programmed to store several consecutive samples at each event trigger.

The results are showed on plot 2.5 where the coherent and incoherent contributions are given with respect to the integration time. The incoherent noise is supposed to be mainly due to pick-up noise integrated by the system. It is evolving linearly with $\sqrt{t}$ as is shown by the fits of the curves. On the contrary, coherent noise increases linearly with time, but remains at a very small level.

From the figure 2.5 it is also possible to extract the ADC contribution, that is interpreted as the "no integration" noise or noise measured at 0ns by extrapolation. We get a value of 0.60 ADC counts for the ADC. This result is mostly due to the reduction of the ADC digital commutation noise (see next section). The form of the fits is

$$\sigma^2_{\text{incoh}} = 0.60 + 0.02 \times t \text{ in ADC}^2 \tag{2.3}$$

$$\sigma_{\text{coh}} = 0.08 + 0.5 \times 10^{-2} \times t \text{ in ADC} \tag{2.4}$$

To extract an estimation of the noise seen in the reconstruction, it is necessary to know the effective time integration. We will see that the digital processing performs a pedestal subtraction with the signal integrated either 25 or 50ns before the measured event (see next section, 2.3). We could then estimate from figure 2.5 that the overall noise will be on average of $\approx$ 1.3 ADC counts per cell. This is exactly what is presently measured in the cavern on the commissioned detector. Finally extrapolating those numbers to a typical photon cluster of

3×3 cells, the fluctuations will be of 3.5 and 2.4 ADC counts ($\sim$ 8.8MeV and $\sim$ 6.0MeV in P_t) respectively for the incoherent and coherent noise [1].

The noise of the shaper is well below one ADC count as expected from the analog electronics simulations. This is in fact partly due to the 4pF capacitor of the integrator that permitted to reduce the amplification of the input buffer of the shaper. A first iteration of the chip had a 2pF capacitor and slightly worst noise characteristics.

The sampling window width has not been considered in the present section. Many tests had been performed to control that the integrated signal could be safely sampled. But, the expected plateau width (requested to be $\pm$2ns) depends crucially on the signal pulse shape and will be more carefully studied in the test beam result part.

2.2.3 ADC levels

Part of the noise of the analog electronics is due to the burst of current from the ADC outputs. In order to reduce the current pulled by the commuting bits, the digital part power supply could be lowered (the choice was between 5, 4.4V and 3.3V) and resistors could be added at the ADC twelve bit outputs. The operation is not easy has the introduction of the resistors by reducing the rising time of the signals will make the sampling of the bits by the following FPGA more difficult. So, this optimisation of the noise had to be done in close relations with the work done to define the electrical standard used at the FPGA input and with the evaluation of the time range for which the 12 bits are correctly sampled. To take an example, if a bit rises too slowly during its transition form 0 to 1, the time for which the signal is above the FPGA input threshold to capture this value is so short, that the 12 bits cannot be properly captured altogether.

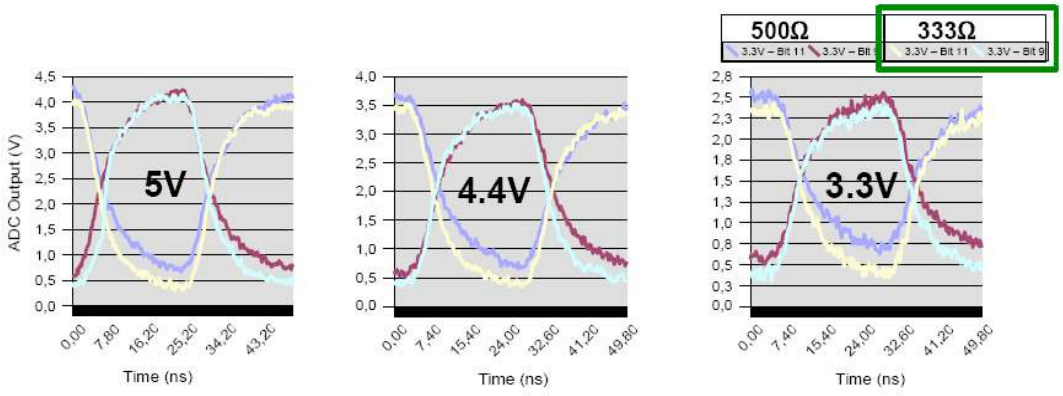

Figure 2.6: The signals captured after the ADC outputs and the resistors added in series for several values of the resistors and of the voltage used to power up the digital part. The two types of transitions are looked at.

[1] The incoherent noise is obtained by summing quadratically the contributions of the 9 cells while the coherent one is evaluated from a linear combination of the error, thus bringing respectively a factor 3 and 9. The integration time used is defined by the subtraction. As we subtract the pedestal from the smallest of the two previous signals, the average integration time introduced in the equations 2.3 and 2.4 is $(25 + 50)/2 = 37.5$ns.

The optimisation is made more difficult by the fact that the threshold for 0 to 1 and 1 to 0 transitions is not the same at the FPGA input. Moreover, the ADC used in the front-end electronics has a bit whose polarity is inverted (2048 value or bit 12), leading to a specific timing for it. Nevertheless, taking those constraints into account, the sampling should be done safely on the 12 bits whatever the transitions.

Bits	5.0V		4.4V		3.3V	
	Level	$\Delta t(500/333\Omega)$	Level	$\Delta t(500/333\Omega)$	Level	$\Delta t(500/333\Omega)$
V_{IL}	1.8	20.2/23.4	1.5	20.2/22.0	1.16	18.0/22.4
V_{IH}	2.5	24.1/22.7	2.2	24.2/23.2	1.67	23.2/22.3

Table 2.1: The table lists the safe time intervals in ns for the sampling of the 12 bits of the FPGA for three power supplies and two values of the ADC output resistors, 500 and 333Ω. The levels indicated correspond to the low and high threshold for the sampling of the transition with the FPGA.

Several tests have been done with different resistors and several power levels from 5V to 3.3V. Table 2.1 lists the time intervals for which the sampling by the FPGA is considered as safe for different configurations. Figure 2.6 shows the corresponding ADC outputs (signal measured after the resistor in series). The electrical standard PCI-X (3.3V) was assumed to be safe enough in coincidence with a 333V resistor in series at the ADC bit output. This is also a configuration that limits drastically the noise induced by the ADC commuting bits in the analog electronics.

2.3 The Digital part of the front-end board

Figure 2.1 shows a general overview of the board with the different digital components that consist of four FPGA:

- The Fe-PGA is in charge of capturing the data from the ADC, performing the pedestal subtraction, evaluating a 8 bits measurement from the 12 bits ADC data for the trigger [41] and keeping the data until a first level trigger 'yes' decision is made. Then, the stored 12 bit words for the 4 channels treated by the Fe-PGA are sent to the Sequencer FPGA (called Seq-PGA later on, see below).

- The Seq-PGA is in charge of building the event from data sent by the 8 Fe-PGA of the board. It also propagates to the Trig and Fe-PGA several control signals (first level trigger bit, reset commands, etc...).

- The Trig-PGA receives the calibrated transverse energy measurements from the Fe-PGA of the board and from the neighbouring ones. It calculates the E_t sum over 2×2 cell clusters and sends the results to the validation board treating the trigger candidates of the FEB region. The Trig-PGA will not be described further.

- The slow control of the board is built around the SPECS interface [30, 31] that provides to the board a I^2C bus.

The FEB also integrates 9 clock phasers adjustable on the full period range with a precision of 1ns (from 0 to 24). Each part provides 4 clocks.

2.3.1 The front-end PGA

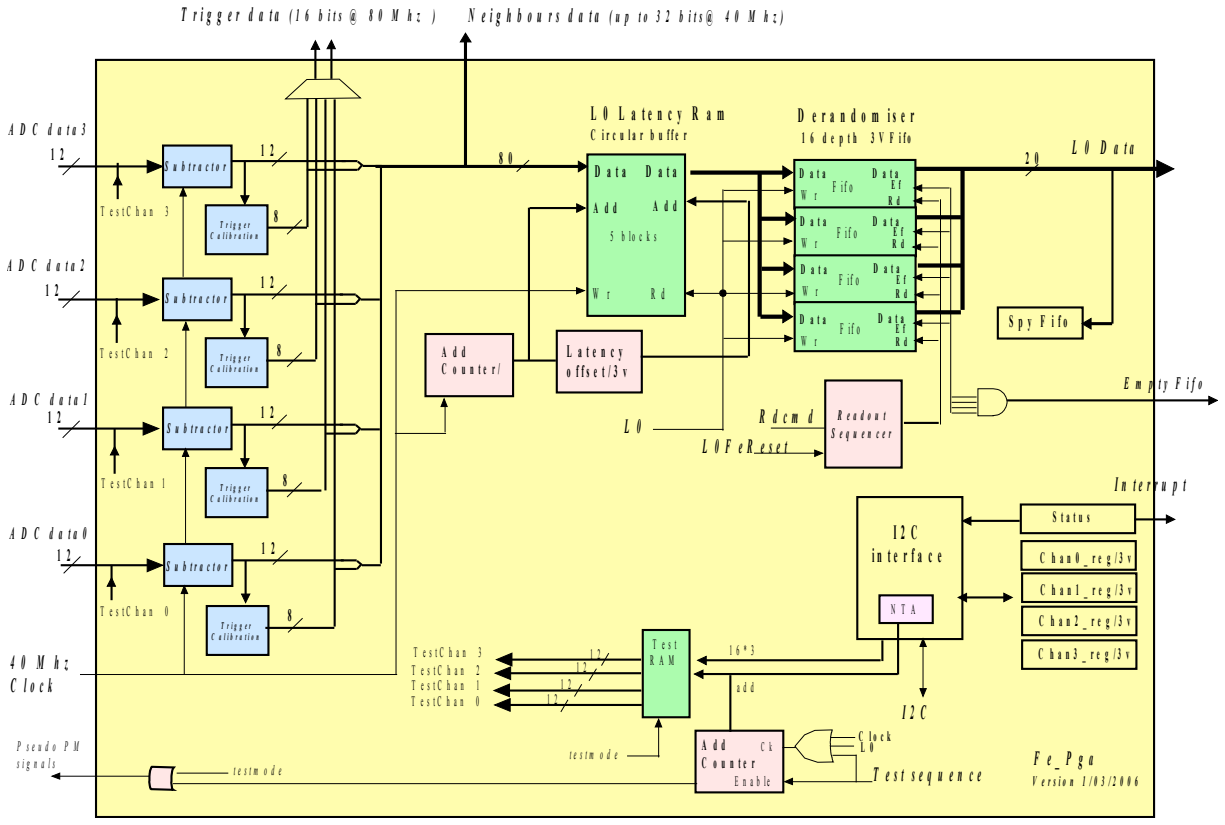

Figure 2.7: This schematics shows the overall functional blocks of the Fe-PGA from the capture of the data, the digital treatment (pedestal subtraction, trigger data evaluation, ...), the pipelining of the 12 bit data and to the derandomiser.

ADC bit sampling

Schematics 2.7 shows the treatment performed in the Fe-PGA. The first processing step is the capture of the data provided by the ADC. We already mentioned the specific electronic

standard chosen (PCI-X) for the Fe-PGA. The component itself is an Actel anti-fuse FPGA AX250 [2]. The reason for this choice will be given in the radiation tolerance chapter 5.

To correctly sample the shaper integrated signal the ADC phase must be tuned so that it captures the signal on the ±2ns plateau. This is done thanks to a clock "phaser" (sometimes also called "delay chip") [12]. The board contains 9 such components and 8 of them allow to tune the synchronisation of the 32 channels independently. Thus, the time arrival of the ADC bits with respect to the Fe-PGA clock is variable and the capture must be flexible to adapt the ADC bit phase. The capture is made twice in parallel with the Fe-PGA main clock and the inverted polarity of this same clock. The ADC bit stability range (see previous section) is such that one of the two polarities at least samples correctly the data. 32 parameters (one per channel) loaded through the I^2C bus (altogether with the clock phases of the ADC) permit to select the correct polarity to capture the data..

Digital calculations

The subtraction of the signal from the previous bunch crossing removes a large fraction of the noise whose frequency is lower than the typical effective integration time. This was explained in section 2.2, where the subtraction was operated in software from the data acquired on several consecutive samples. The subtraction is now done in a specific functional block of the FPGA.

This operation has another aim as it will remove the pedestal of the signal. Simulations [5] have shown that the occupancy, even in high multiplicity regions of the calorimeter, is low enough to consider that the probably for 3 sizable signals to occur in three consecutive LHCb periods of 25ns is negligible (for an average pile-up of 0.4 interaction per crossing). Hence, the baseline subtraction is done by removing from the current signal the smallest of the two previous ones.

Removing the smallest of the two previous samples naively leads to an effective integration of $(25+50)/2$ ns and a noise of ≈ 1.3 ADC counts as mentioned already. Another consequence of this type of subtraction, is that, selecting systematically the smallest of the two previous samples, induces a bias in the measurement. This bias is estimated to be 0.42 times the pedestal fluctuations i.e. half an ADC count. This offset is removed from the data in the software reconstruction.

Notice that 256 is added to the ADC value before the subtraction is performed in order to prevent the data to be negative for small fluctuations, the data being then coded on 13 bits. The final result is truncated between 0 and 4095. Hence, a true "0" signal is coded 256 ADC counts, the digital value ranging between -256 and 3839.

A second subtraction method was implemented in the electronics and consists in evaluating the previous pedestal offset by a constant (that is loaded on 3 bits by the slow control and whose value is typically between 1 and 3) and comparing it to the previous measurement. If the later is larger, the former is used for the current pedestal otherwise the measurement is used as a new pedestal. This second method varies more slowly than the standard method presented above and may not follow rapid pedestal fluctuations, but it leads on average to slightly better resolution by 0.2 ADC counts on average. This second method may be chosen by setting some registers (a switch and the constant coded on 3 bits).

Finally another register permits to disable the subtraction. This possibility is very useful to debug a damaged board as the data do not depend anymore on the history and the digital

treatment is simplified.

The second digital operation is the calculation of the trigger information. To evaluate those words, it is necessary to convert on 8 bits the ADC data after having applied a calibration factor to them. The reader interested in how this calculation and truncation to 8 bits is done at the FPGA register level will find more details in [44].

At this level, the data sent to the acquisition contain the 12 bits from the ADC to which the 8 bits obtained from the trigger calculation are added. Each word are now 20 bit wide. This will allow to control at future stages the correct transmission of the signals, as the trigger part, the 8 last bits, can be re-evaluated from the 12 first ones.

Synchronisation scheme for the data capture

In the previous section, the first stage of the Fe-PGA was described, but it is necessary to show some of the implications of the method. The problem depends on several timings: the ADC clock which has an unknown phase with respect to the FPGA, the Fe-PGA clock itself which is the global clock of the board and the polarity chosen to capture the data at the Fe-PGA input.

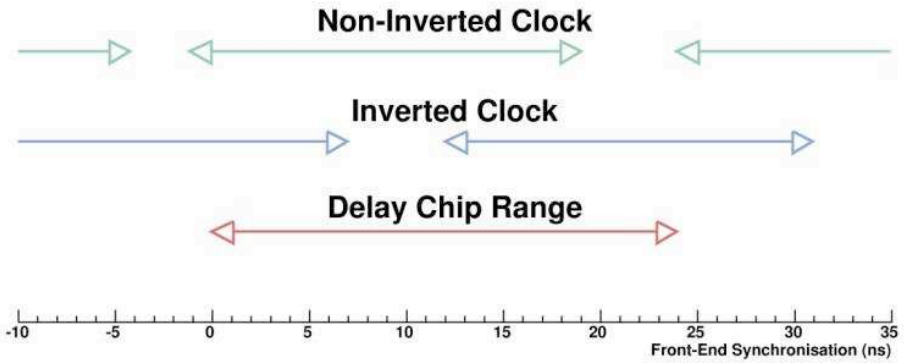

Figure 2.8: The allowed clock phase selection (called "delay chip range") for a proper sampling of the data by the Fe-PGA. A tuning of 20 can be acceptable only in inverted clock mode and would lead to a delay of 25ns with respect to a selection below 7 still in inverted clock mode.

The acceptable solutions for this problem, some of the configuration leading to a wrong sampling, is shown on figure 2.8 where the bottom x axis (called "delay chip range") is the adjustable phase applied to the ADC clock with the clock phaser component. This plot was obtained by spying inside the Actel AX Fe-PGA[2] and checking the different timing and clock polarity configurations. The allowed regions correspond to the horizontal arrows of the figure. The arrows are not joined which indicates the presence of instability gaps for some specific tuning of the two polarities. But, it is clear that whatever the timing, a polarity offers a good solution. Moreover, it should be pointed out that two consecutive ranges for a single polarity are sampled in two consecutive bunch crossings, i.e. would be seen as captured with a delay of 25ns with respect to each other; the setting "5ns-Inverted" is equivalent to "5ns-Direct" but is

[2]This possibility is offered on this FPGA from Actel using the Silicon Explorer tool which has proven to be excessively helpful.

more dangerous. The tuning of the latency in the pipeline of the Fe-PGA permits to correct, by steps of 25ns, the time alignment of the data for a group of 4 channels in a Fe-PGA.

The timing spread of the channels has been studied carefully during the conception of the boards, during the commissioning with cosmics, TED runs [3] and mainly with the first particles [66].

The timing spread mostly depends on the cable length differences, the $\cos\theta$ effect of the particles travelling from the interaction point to the surface of the calorimeter and the high voltage tuning of the PMT. The gain of the PMT is chosen so that the signal extracted is not a measurement of the energy deposited but of the P_t of the particle. This is necessary in order for the fast first level trigger information obtained from the cells to be directly the transverse energy. This value is easily converted back into the energy during reconstruction at the software level. Hence, the PMT high voltage is not constant over the calorimeter surface but matches the P_t trend with rapidity. A 100V increase of the HV leads approximately to a 1ns faster signal. This has to be taken into account, and summing up all the effect, the overall spread did not exceed 8ns, so that all the channels of the ECAL and HCAL have been eventually tuned in the "non-inverted" mode in 2010 and in a range of $[5, 16]$ ns[4]. The time tuning of the system is a complex optimisation which involves several degrees of freedom on the FEB and on the CROC that provides the clock and captures the data. This aspect will only be briefly mentioned at the end of the next chapter.

Latency and derandomization

The data are now ready to be sent to the LHCb acquisition through the CROC board. But only a fraction of the events is actually sent. The aim of the first level trigger is to reduce the bandwidth from 40MHz [5] to 1MHz. Before the L0 decision is made, the data are stored in a circular RAM. When this decision arrives, the data stored n clock beats before (n being a value loaded by slow control) are extracted from the RAM and injected into the derandomiser. This mechanism can clearly correct for 25ns step misalignment of different parts of the front-end, as explained above.

The L0 latency is at maximum 160 clock beat long and a comfortable 256 word deep RAM was used to store the data. 4 words of 20 bits (12 ADC and 8 trigger bits) are sent by each Fe-PGA to the Seq-PGA through the derandomiser.

A 32 word deep FIFO is used as a derandomiser to buffer the data to be sent to the Seq-PGA which drives the reading of this FIFO through command signals (see figure 2.9).

[3] TED is a beam absorber for injection (External). Before the first LHC beam circulations, the accelerator teams performed injection tests for which a low intensity bunch of protons was injected in the LHC and was stopped immediately by a screen. These "collisions" produce a flow of particles which are seen by LHCb (if the injection is done in the proper direction). Such "events" permit to perform a broad first relative time alignment of the channels of the detector.

[4] Notice that the HV and $\cos\theta$ effects partly compensate.

[5] The proton-proton collision rate is lower than 40MHz which is the LHCb trigger working frequency and depends on the beam focalisation at the interaction point, the LHCb bunch structure, the energy of the beam, etc ....

2.3.2 The sequencer

The Seq-PGA is an APA300 FPGA from Actel [2] (see section 5 for the justification of this choice). This is the event builder of the board. It gets from the CROC the trigger signal and the synchronous commands (also called Channel-B commands: reset, calibration, etc...) sent by the fast control of the experiment and drives the downloading of the 20 bit words from the Fe-PGA.

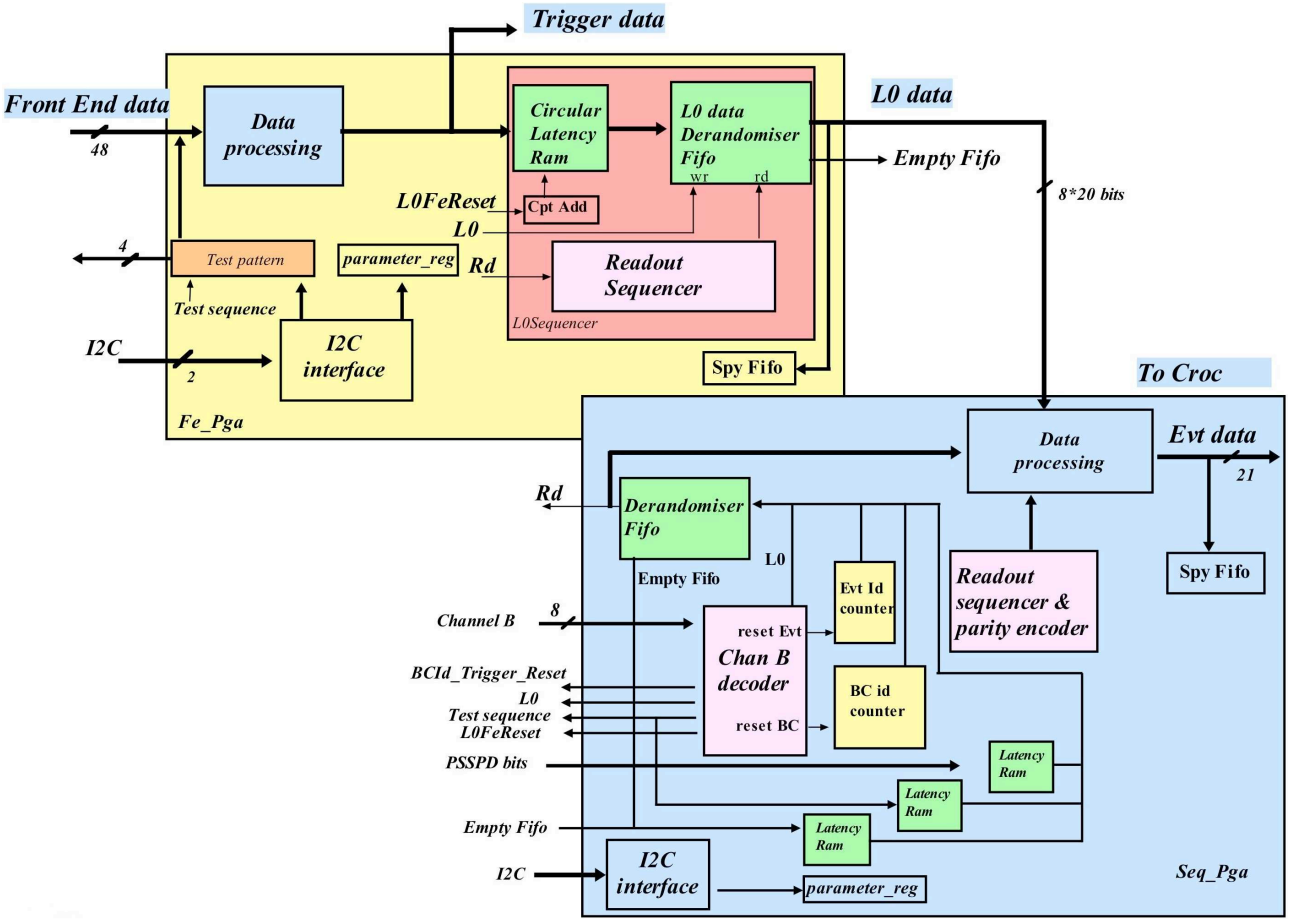

Figure 2.9: The interplay of the Fe-PGA and of the Seq-PGA is shown here with the main functional blocks. The Front-end FPGA is in yellow and the sequencer in blue. The L0 data exchange between the two FPGA is clearly seen altogether with the Sequencer output to the control and readout card (also called CROC and described at the next chapter).

Event building

The event building is done in the following way after a L0 "yes" is received:

1. A 20 bit wide header word is generated. Two counters incremented by the clock allow to generate a bunch and an event identification number. Those counters are regularly reset

by a specific channel-B or fast control command. The two words are joined together and serve at verifying the correct propagation of the data on the acquisition path.

2. A second 20 bit wide word, called control word, is built from:
   - Two bits corresponding to the state of the derandomiser FIFO (fifo empty bit) of the Fe-PGA and Seq-PGA.
   - Two bits indicating if the event is a calibration event (LED events are used to calibrate the calorimeter and are triggered by fast channel-B commands) and if the internal test sequence is enabled (a RAM is used to inject data patterns at the input of the front-end electronics (the tests tools implemented on the board will be mentioned in the chapter 4).
   - Two bits giving the parity of the clock used by the SPD and the PS. As mentioned previously, contrary to the ECAL and the HCAL, those detectors integrate their MAPMT signals with two interleaved integrators running at 20MHz. The Seq-PGA of the ECAL/HCAL is also included in the SPD/PS front-end boards with its original firmware. Moreover, the CROC that receives the data from the sequencer is used by the four calorimeters and not only the ECAL/HCAL system. Those 2 bits have been provided so that it is possible for any event to determine the integrator of the SPD/PRS very-front-end at the origin of the signal.
   - Finally, a word coded on 8 bits gives the number of clock beats since the previous L0 received.
3. The 32 channel words of 20 bits each are fetched from the Fe-PGA. A read command is activated by the Seq-PGA and in response the Fe-PGA present their data consecutively on their output bus. The Seq-PGA captures the data from the 8 Fe-PGA in circular permutation, starting by the channel 0 of Fe-PGA 0, then channel 0 of Fe-PGA 1,...

Each one of the words produced in the sequencer sees its length increased by a 21st bit which is its anti-parity. This is another protection that allows to check the correct transmission of the words on the data path or to flag words affected by single event upsets (see the chapter 5 discussing radiation problems). The reason for the extra bit to be the anti-parity of the word comes from the detection of the new event by the CROC. This board will receive the events from the Seq-PGA but will not use the L0 to decide on the arrival of a new one. From the CROC, a new event is defined by two empty words (21 bits long) followed by a non-empty one. This is assumed to be the header word. This definition requires any data word to be strictly different from 0. A parity bit would not permit such a logic. Notice that the data word 0 would lead to an anti-parity of "1". As will be described in the chapter dedicated to the CROC, this board compares its automatic event detection method described above to the L0 signal it receives to check the synchronization of the system.

As for the front-end electronics, the Seq-PGA sends its words to a derandomization stage that propagates the 36 words of an event (now the two extra empty words are part of it) at 40MHz. This leads to the overall LHCb front-end acquisition event rate of 1.1MHz. The words are serialised by a component converting the 21 bits into three signals 7 bits wide and a clock. The 4 differential signal are propagated on the backplane at 280MHz to the CROC that treats them.

Control and commands

The Seq-PGA receives three fast command signals from the CROC:

1. the L0,
2. the calibration command,
3. the front-end reset,
4. the bunch crossing identification reset.

As was described already, the L0 is used by the Seq-PGA to trigger its own generation of header and control words. It also leads to the synchronous production of the signals sent to the Fe-PGA in order to fetch the 32 channel data words.

The calibration commands are propagated to the Fe-PGA and are used for test purpose. Moreover an extra bit of the control word will contain the corresponding information.

The front-end reset is produced regularly (typically at each new bunch crossing number sequence, i.e. at the beam revolution frequency) in order to reset the electronics that requires it. This front-end reset is presently not used by our front-end electronics, but for test purpose (reset of the RAM pattern pointer).

Finally the bunch crossing identification reset is used to properly tag the events (in the header word). This signal is sent by the global fast control of the experiment and should be adjusted by every sub-detector depending on its latency. The purpose is to compare the bunch number from the front-end with the expected one just before the events are actually sent to the LHCb PC farm. A delay programmable through slow control permits to postpone the reset of the counter and to tune the bunch identification value sent in the data to the calorimeter electronics latency.

2.4 Test beams results

The front-end electronics prototype and (close to) final version have been put in a test beam at SPS (west area) twice since 2000. The particles used were electrons, muons and pions from tertiary beams at energies ranging from 10 to 50GeV . The setup was made of 3 to 9 HCAL and ECAL modules facing the beam on a movable table. The cells were equipped with PMT whose bases were connected to the front-end electronics and to a channel of a large time integration window Lecroy ADC, the signal being shared between the two parallel acquisitions. The trigger was given by a series of scintillating detectors on the beam axis providing a TDC measurement for every event. The available information was the arrival time of the particles, the Lecroy measurement and the data from the front-end electronics. The first test permitted to extract information on the modules themselves (resolution, optical fibre comparisons, etc...) and on the first front-end electronics prototype. It integrated a preliminary version of the shaper (the main differences with respect to the final version are the lower capacitance, 2pF instead of 4pF and the crosstalk between channels 3 and 4 which was not yet corrected) and only 16 channels.

Apart from the ADC, the digital part of the board (based at that time on a FPGA of type Altera[6]) was quite different from the final version.

The second test beam was performed with a close to final prototype of the front-end electronics. The shaper was part of the final production and most of the digital electronics components have been kept for the final production.

Here, the results given concern both tests as the second mostly confirmed the results of the first one and the operation mode was very similar.

2.4.1 Sampling window

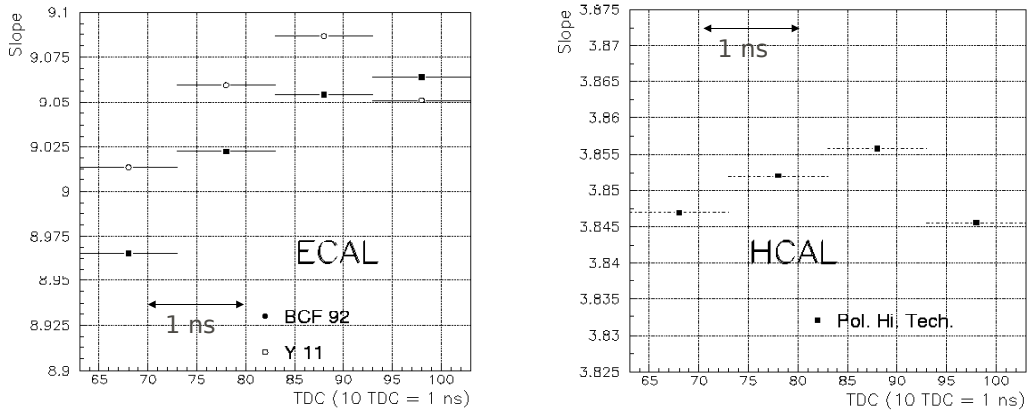

Figure 2.10: The data points give the slope of the correlation curve between the front-end electronics and the Lecroy integrator in TDC bins of 1ns. Two types of fibres, called BCF92 and Y11 have been used for the ECAL. The HCAL modules in test were made from Pol.Hi.Tech fibres.

The sampling width of the plateau depends on many effects that have been already described. The data stored during the two test beams at CERN have been used to measure the width in realistic conditions and showed the stability of the integrated signal on ± 2 ns. The figure 2.10 shows the slope of the correlation curve of the fast front-end electronics versus the slow Lecroy integrator with respect to the time arrival of the particles as measured with the TDC system. The left plot shows the evolution of the slope for two types of fibres (BCF92 and Y11) and for the ECAL. The right one is the result obtained for the HCAL cells. Let's recall that the Lecroy integration is a long time window integration of the signal and does not depend on any time scale while the fast front-end electronics depends on the sampling time of the shaper output. If the sampling is shifted in time, only a fraction of the PMT pulse is integrated which would reduce the overall gain of the system. This is what is seen on figure 2.10 where the slope is nevertheless stable at the per cent level in a time window of ± 2 ns.

[6]The final board is radiation tolerant which required a specific design of the digital part. This will be described in the section 5

2.4.2 Linearity

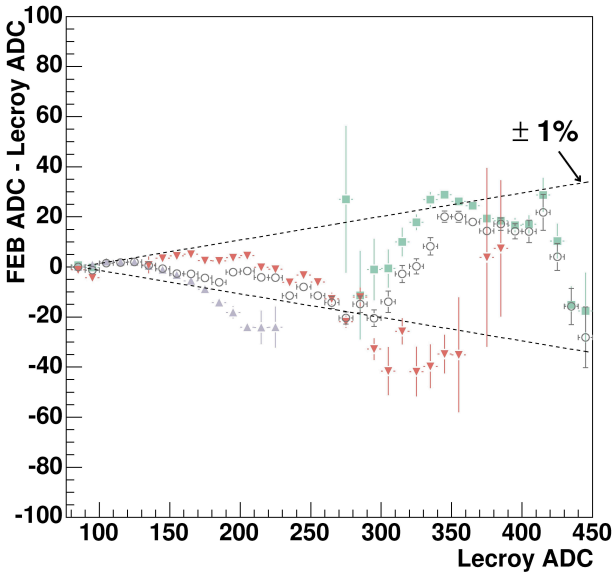

Figure 2.11: The linearity is measured by comparing the Lecroy integrator to the front-end electronics. The calorimeter energy is measured here in the central cell of a series of modules fired by the beam. By slightly moving the modules with respect to the beam, it was possible to split the shower energy between several cells and to scan the linearity in different energy regions. This is what is done on the blue (beam heading at the neighbouring cell), red (the beam is tuned to reach the border of the central and neighbouring cells) and green (the centre of the cell being read out is targeted) curves. The circles show the results for the full statistics accumulated during the test beam period.

The linearity has been measured by comparing the fast front-end electronics to the Lecroy integration after tuning the sampling of the shaper and for a specific time arrival of the particles window obtained from the TDC. The figure 2.11 shows the results obtained. In order to scan different energy ranges, the modules of the calorimeter have been installed on a moving table. Hence, it was possible to slightly shift them with respect to the beam and to split the energy deposited in the module between several cells. The central one was connected to the fast readout and the Lecroy integrator. The curve shows that the ± 1 % limit is reached.

Part of the events in blue and red on figure 2.11 show a linearity below 1%. Those events have been looked at more carefully. As the front-end electronics was able to perform the acquisition of a series of consecutive events, it was easy to show that for those events, a fraction of the energy had arrived at the beginning of the TDC time window. Thus, the non-linearity observed was most probably due to a time shift of the arrival of those particles.

2.4.3 Noise

The noise of the system was measured by running the electronics without input signal. The estimation showed that we may reached $\approx$ 1.3 ADC count as seen in the previous sections.

This is what is obtained after pedestal subtraction as seen on figure 2.12.

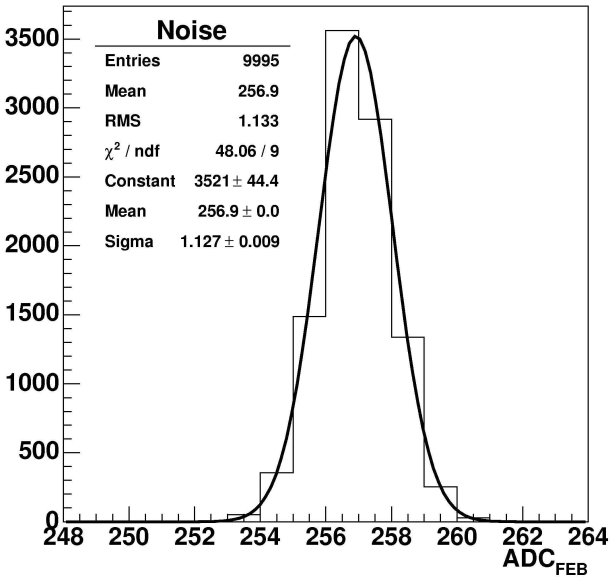

Figure 2.12: The noise measured on the front-end electronics after subtraction of the pedestal. A noise of ≈ 1.1 ADC is measured corresponding to the previous estimations.

Notice that without pedestal subtraction, the noise is integrated for a far longer time and we observed a fluctuation of the order of 17 ADC counts.

2.4.4 Crosstalk

The crosstalk had been measured on a test bench and was found satisfactory after the latest correction of the shaper. We tried to check it in test beam on the final system. The method used consisted in measuring the signal split between two cells. One cell (called channel 2 on figure 2.13) was connected to the fast electronics only and received the largest proportion of the energy. The second cell (channel 1 on figure 2.13) was slightly shifted and received only a small fraction of the shower. Moreover, the latter was connected to the neighbouring channel of the former on the same shaper and altogether to the Lecroy integration.

A calibration factor was previously determined in order to match the fast electronics and the Lecroy integration measurement, this is the α parameter indicated on figure 2.13. A sizable crosstalk at the level of the shaper would lead to a difference between the measurements on channel 2 done by the fast electronics and the Lecroy integrator. This is not observed on the data where we see that the effect is far below 1%.

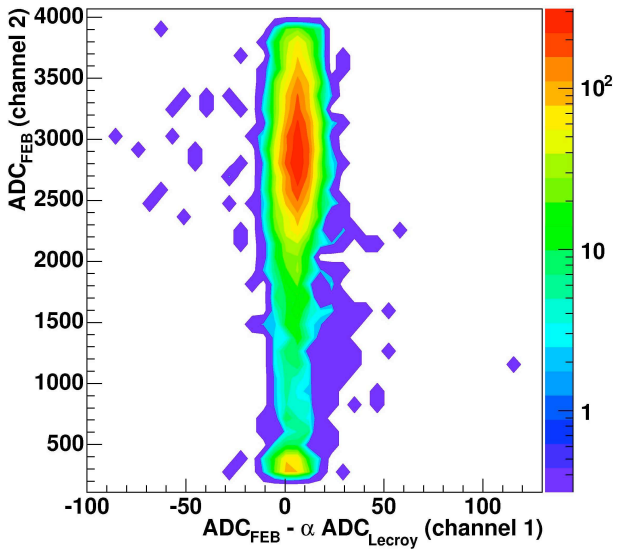

Figure 2.13: Measurement of the crosstalk between two adjacent channels of the shaper. A value of less than 1% is obtained.

Chapter 3

The calorimeter control card

Contents

3.1 Introduction 51
3.2 General Description 53
3.3 Data capture and treatment 54
3.4 Control of the crate 58
3.4.1 Trigger, time and fast controls (TTC) 58
3.4.2 Fault 60
3.4.3 The slow control 60
3.4.4 Resets 60
3.5 Tests performed on the CROC and shielding 61
3.5.1 Temperature measurements 61
3.5.2 Overall crate synchronisation 61
3.5.3 Bit error rates 63
3.5.4 1 MHz test at the pit 64
3.5.5 CROC shielding 66

3.1 Introduction

A calorimeter front-end crate contains up to 16 front-end boards [44, 40] (FEB) which perform the acquisition of 32 channels each. The data are stored at 40MHz in a cycling RAM located in the FPGA of the boards. If a L0-yes trigger occurs in due time, the corresponding data are sent altogether by the FEB in the crate through the backplane and to the calorimeter readout card (CROC) [38]. The overall data rate at the CROC input is 1.1 MHz

The CROC is able to:

- capture the data with its deserializers,

- detect the presence of a new event (header detection),
- synchronize its optical fibres output (GOL chips of the optical mezzanines),
- add 11 extra bits on top of the 21 bits provided by each FEB (data, FEB and crate identification),
- and finally send the data through its optical outputs.

Moreover, the CROC sends through the backplane of the crate the time, fast and slow control signals used by the various boards[47]:

- the 40MHz clock,
- the L0 trigger signal,
- the broadcast commands (channel B, fast control),
- the slow control signals.

Apart from the previous operations which are mandatory, the CROC has useful debugging capabilities. The user may:

- capture the data from the FEB and send them through the slow control path in order to perform a slow rate acquisition independently of the main path (LHCb DAQ path),
- trigger user-defined L0 triggers,
- send user-defined broadcast commands,
- provide an independent clock (external clock).

The DAQ path is made, by construction, independent from the slow control path in the sense that a slow control failure cannot affect the DAQ path. Among its debug capabilities, the CROC may run in two different modes:

- Spy mode: the data incoming from the backplane (as described above) are captured by the CROC Fe-PGA, filtered and sorted by the CROC Spy-PGA and sent through the slow control to an acquisition computer. This was mentioned above.
- Optical Pattern Generator mode: the RAMs of the CROC Fe-PGA are loaded with predefined patterns. When a specific trigger is received the optical fibres are synchronized and 34 words extracted from the RAMs at the current pointer position are sent to the optical outputs as for real data. This allows to check the optical connections down, to the counting room.

The spying capabilities of the CROC will not be described here. The interested reader may have a look at [38].

3.2 General Description

Figure 3.1 shows a picture of the CROC. The various parts of the board are clearly identified. Following the L0 data path (or from right to left on the picture), first, the CROC receives the event bits incoming from the FEB from the connectors plugged into the backplane. The data have been serialized at 7x40MHz. The first stage of the processing consists in de-serializing them, which is done by 16 deserializers or receivers. Each component is connected through the backplane point-to-point lines to one FEB slot of the crate.

The CROC supports 5 FPGA of two different types, called in the future Fe-PGA (4 copies on the board) and Spy-PGA. The formers are APA300 PGA from Actel and receive the data from 4 deserializers (or 4 FEB) each. Then, they perform the header detection of the incoming bits, add the header, control word or data identification two bits and finally send them to the optical mezzanines [52] which support "GOL" chips, Gigabit Optical Link transmitter ASIC [14]. Those are the optical transmitters used to send the data to the counting room and the TELL1 boards [50].

Each 8-channel optical mezzanine is dedicated to half a crate (up to 8 FEB) the sharing being done between its left and right parts. The Spy-PGA is an APA450 fromActel and is the conductor of the board and performs the actions which are not specific to a data channel. Hence, the optical mezzanine synchronisation is triggered by it. The Spy-PGA is also in charge of copying and sending through the slow control the data stored into the Fe-PGA for spying purpose (see reference [38] for more details on data spying with the CROC).

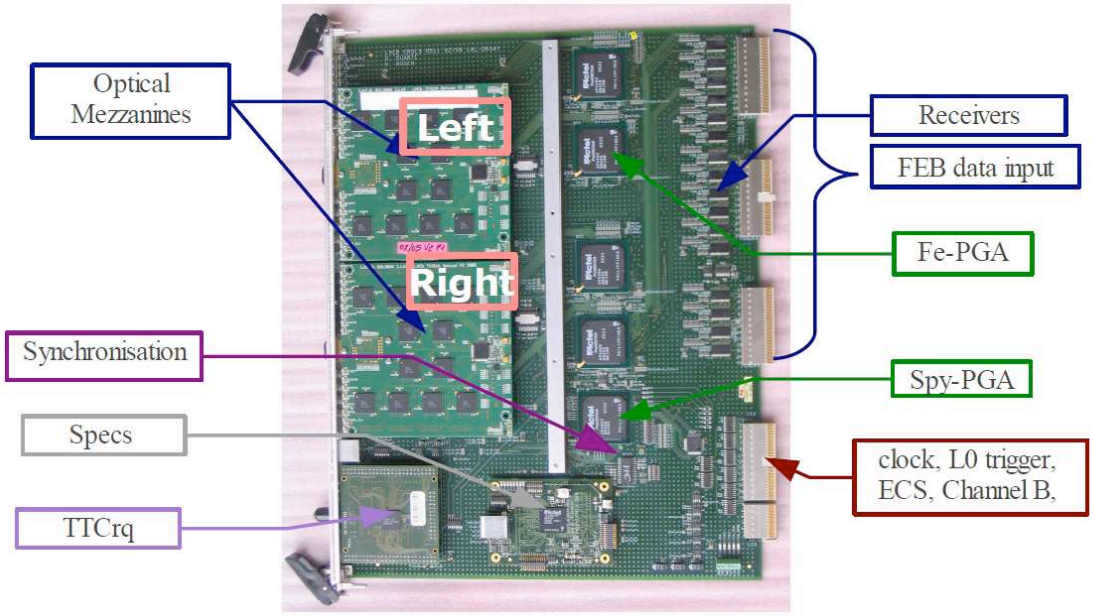

Figure 3.1: Top picture of the last version of the CROC. The main blocks of the board are identified. "Left" and "right" indicate the half crate concerned by each optical mezzanine plugged on the board.

The clock, L0 trigger and channel B signals are provided to the CROC by the TTCrq

mezzanine board [83]. This mezzanine supports a TTCrx chip developed at CERN [73]. The signals are sent to the Spy-PGA which propagates them to the backplane through the bottom connector which serves the facility bus of the crate.

The slow control is done by a SPECS[1] system [30, 31]. A SPECS mezzanine (slave) is plugged onto the board and provides the 16 bit parallel bus to control the 5 PGA of the card, two I^2C buses for the delay chip, the TTCrq and the Optical Mezzanines. Finally the SPECS signal is propagated down to the bottom connector in order to repeat the SPECS signal for the Glue PGA[2] of the front-end and validation boards.

Finally, a delay chip [12] is used to tune the sampling of the FEB data and to adjust the clock phase of the FEB in the crate.

3.3 Data capture and treatment

After a L0 occurred, each FEB sends 34 words, 21 bit wide, serialized by a factor 7 to the CROC. The data are received by a deserializer whose output is captured by the Fe-PGA. The sampling by the Fe-PGA may not be necessarily adapted and some instabilities may be expected if the phase of the clock sampling the data cannot be adjusted. A channel of the delay chip of the CROC is used to tune the timing for the capture of the deserializer output. This is done with a series of registers of the Fe-PGA (21 are needed for the 21 bits). Finally, the output of those registers has to be re-synchronized with the global clock of the CROC and this is done by a second stage of registers.

The format of the data at the CROC input is given in figure 3.2 (see also [45]) and consists first of two words, the header of the corresponding L0 trigger and the control word. Then, the 32 ADC (12 bits), trigger (8 bits) and anti-parity (1 bit, total of 21 bits) values for the FEB (32 channels) are sent[3]. As the time budget for an event is 36 words, the two last ones are empty and will be called in the future separation words. Notice that the use of the anti-parity as the 21^{st} bit for the 34 meaningful data of a L0 prevent them from being confused with the separation words.

Thus, the FPGA will capture the real information among the incoming bits by detecting the header of the L0 and without getting a direct trigger.

This is done by using the fact that a L0-yes is unambiguously identified as it cannot be made of 21 zeros. The beginning of an event can be detected by scrutinizing the output of the deserializer, performing sequentially a "OR" on the 21 bits of a board and accepting the first one-value preceded by two empty words observed: this is a header. The recognition of header is then disabled for the following 33 words corresponding to the L0 control information and the 32 channels sent by the FEB. The header recognition is then enabled again and the system is prepared for the capture of a new event.

The header detection decision requires some clock beats to be done and the deserializer bit

[1]Serial Protocol for the Experiment Control System, this is the hardware used to communicate with part of the LHCb electronics located in the not radiation safe area (detector zone).

[2]The Glue PGA was not discussed in the previous section. This FPGA is implemented on the FEB and is its slow control interface.

[3]The channel data format indicated here corresponds to the ECAL/HCAL electronics. It is different for the SPD/PRS data. Nevertheless, the data width is the same (21 bits).

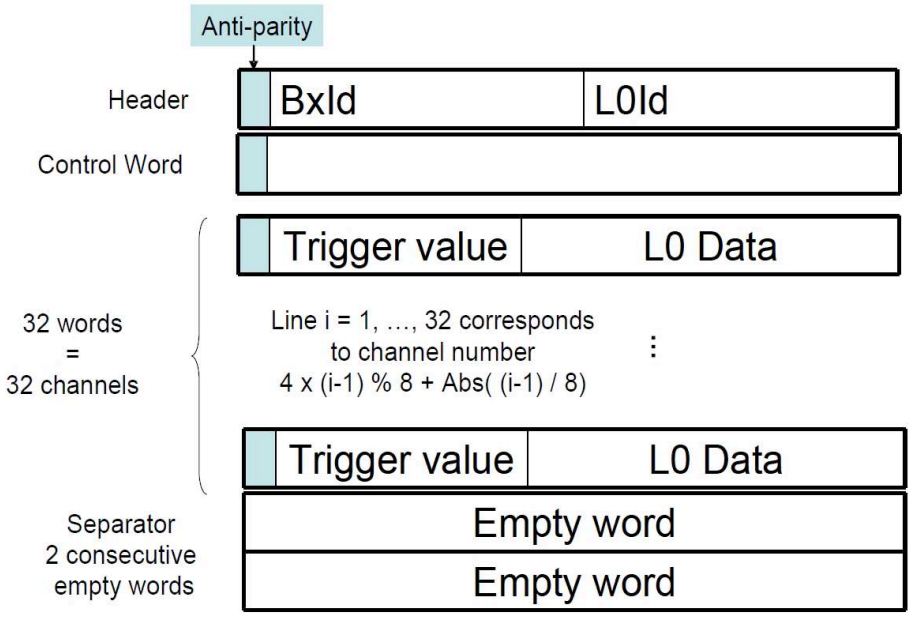

Figure 3.2: The LHCb front-end calorimeter data format.

flow (whatever the words, empty or not) has to be delayed in a first stage pipeline (header detection pipeline) of 2×25ns. Then, according to the decision, nothing has to be done (data are null) or the treatment proceed in the next pipeline. This processing is done for every FEB out of the 4 treated by a Fe-PGA. A control is performed at this stage in order to check that the header detections of the 4 FEB are identical and synchronized. If not, the Fe-PGA status register is flagged.

When the headers are detected for the 4 FEB, each Fe-PGA propagates its decision to the Spy-PGA which in turn checks the synchronisation of the 4 Fe-PGA. Let's recall that in a crate the functioning of the 16 potential FEB is synchronous. Once more, in case of error, the Spy-PGA status register is flagged.

The two protections mentioned above require to provide specific information to the PGA:

- Each Fe-PGA has to know which FEB are really connected. The control register of the Fe-PGA contains 4 bits which allow to mask each one of the 4 treated boards. This may be used to remove faulty boards or to mask unused inputs.

- The Spy-PGA has to be aware of the unconnected boards in order not to be confused by missing header detections from any unused Fe-PGA. This is tuned by 16 bits of the Spy-PGA control register.

A second pipeline (see figure 3.3, depth of 3×25ns) in the Fe-PGA allows to wait for the Spy-PGA processing which consists of checking the Fe-PGA synchronisation (as described above) but also in synchronizing the two optical mezzanines. This is done by acting on the "transmit enable" pins of the GOL chips of the mezzanines which are connected to the Spy-PGA. The synchronisation lasts 2 clock beats (corresponding to the two separation words if the

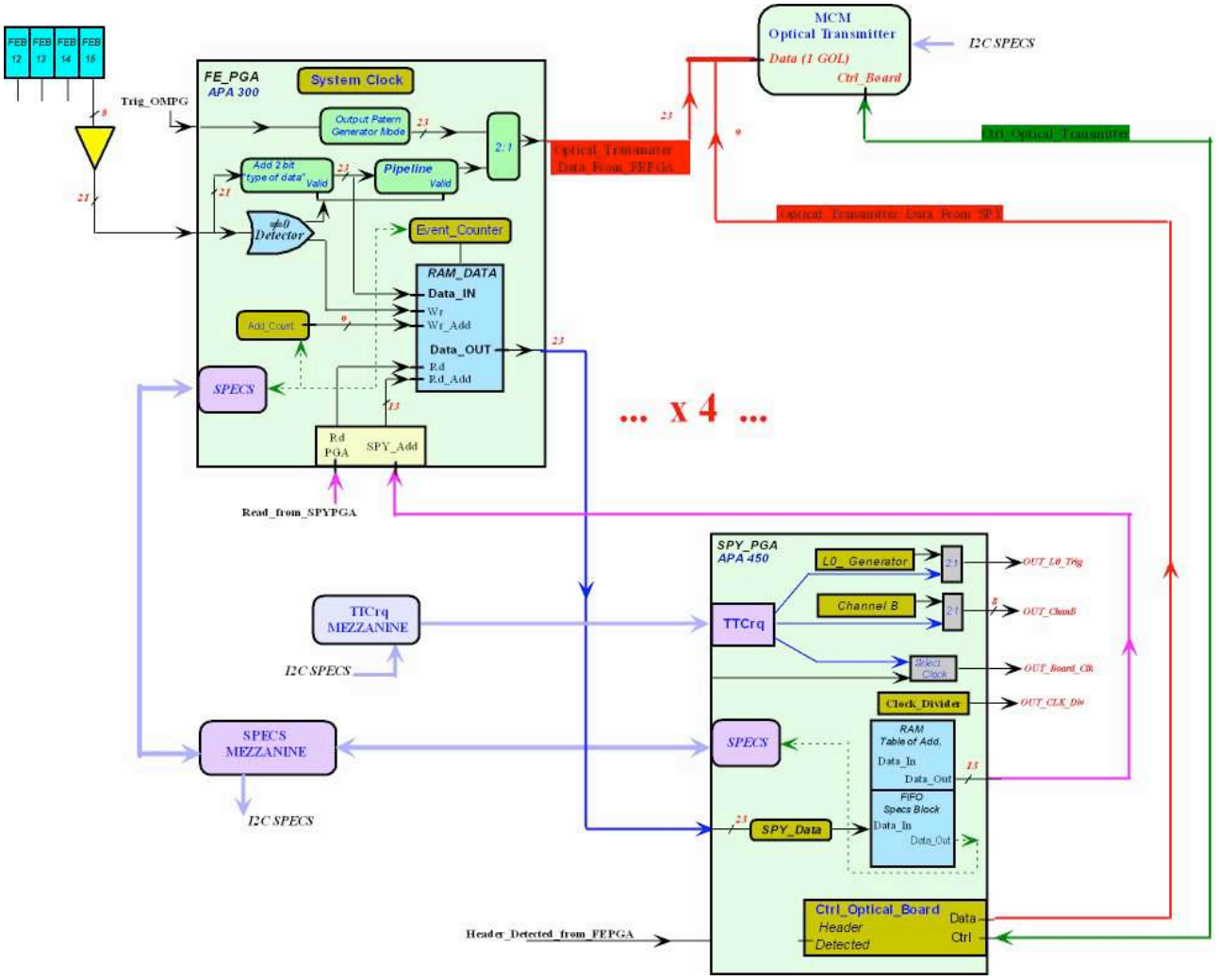

Figure 3.3: The treatment of the data by the CROC.

L0 triggers are consecutive). The length of the second pipeline of the Fe-PGA is such that its data are sent to the optical mezzanines when the already mentioned "transmit enable" signal is released by the Spy-PGA (see figure 3.4).

Notice that, at the input of the second pipeline i.e. after the header detection, each Fe-PGA adds two extra bits (data identification) to the 21 incoming ones. Those bits are of course '00' if the data word are empty (there was in fact no header detection), '11' for a header, '10' for a control word and '01' for the data corresponding to the calorimeter channels. This is done with a counter launched by the header detection and whose output is the selection of a multiplexer. The downstream data flow becomes 23 bit wide at this stage. A full data word for the LHCb DAQ (or at the CROC output) is 32 bit wide. The first 23 bits have been already described above, 4 extra bits are the FEB identification which is defined by pull-ups and downs soldered on the PCB (16×4 levels) and 5 bits define the crate identification which is identical whatever the optical output of the CROC considered and thus occupies 5 pins of the Spy-PGA.

The 9 extra bits soldered on the PCB (FEB identification, 4 bits) or sent by the Spy-PGA

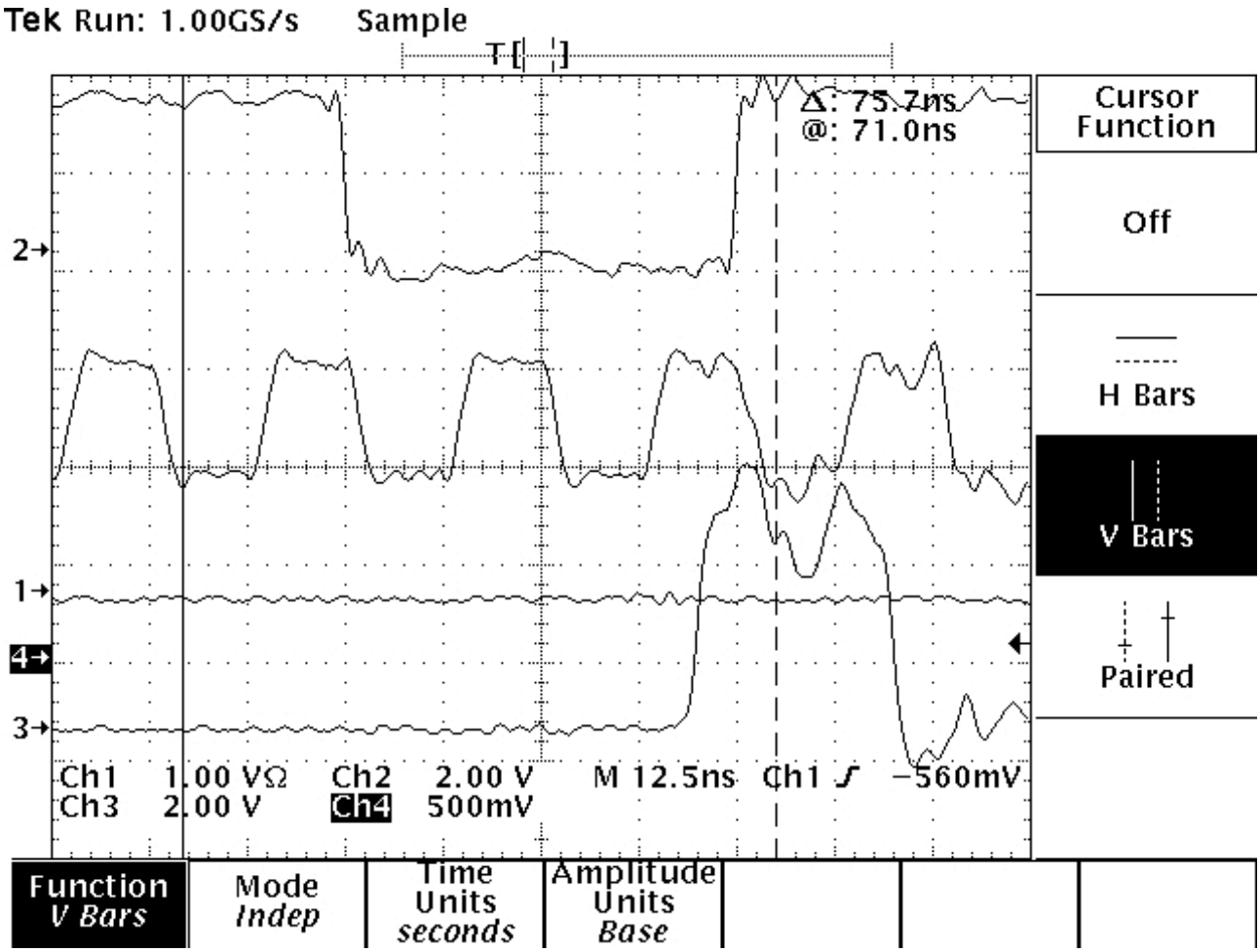

Figure 3.4: Clock (middle), synchronisation pulse (top) and first data bit (bottom) as seen from the input connector of the top optical mezzanine. The synchronisation of the fibres is triggered by the Spy-PGA and is followed by the data sent by the Fe-PGA.

(crate identification, 5 bits) are static and are maintained at their nominal value also during a fibre synchronisation. On the contrary, the 23 bits sent by the Fe-PGA are of course not static and the flipping may occur every 25ns. At the level of the GOL chip of the optical mezzanines, we cannot be sure that the clock and the signals have not their fronts close to each other or almost superimposed which may lead to some instabilities. The adopted solution consists in having the possibility to use either the direct or the inverted clock front to latch the data at the output of the Fe-PGA. One of the two alternatives has to be stable. This protection is also applied to capture the time and fast control signals (called TTC, see section 3.4.1).

3.4 Control of the crate

3.4.1 Trigger, time and fast controls (TTC)

The LHC clock (40MHz) is propagated from the counting room and altogether with the fast control signals (L0 and channel B commands) with an optical fibre plugged to the front-face of the CROC. The TTCrq mezzanine connected onto the CROC supports a TTCrx chip which decodes the optical fibre signals and provides the clock and fast controls to the board. The TTCrq may be controlled through I^2C in order to adjust the clock phase (steps of $\approx$ 100ps) and the coarse delay that shifts the L0 and channel commands by steps of one clock period.

At the CROC level, it is possible to adjust precisely the timing of the various clocks. This possibility has been heavily used for the SPD, PRS, ECAL and HCAL as it was giving an extra degree of freedom in adjusting the timing of the different parts of the system.

The CROC provides the TTC signals to the boards of the crate:

- the clock signal,
- the L0 trigger,
- the Broadcast commands (channel B[7:2])
- Bunch crossing Id and Event-Id (strobed with the clock by the CROC).

Clock

The propagation of the clock signal down to the backplane has been carefully done. Figure 3.5 shows the clock tree. The clock incoming from the mezzanine TTCrq board is first buffered by a LVDS (Low Voltage Differential Signaling) to LVDS converter. Two outputs are sent to the two optical mezzanines directly. The third output goes to the Spy-PGA. An internal multiplexer permits either to select the TTCrq clock as the global clock (this is the default mode) or to be in debugging mode and to select a clock provided by the user to the front panel (NIM input). Notice that the optical mezzanines become asynchronous to the CROC in this second mode and no DAQ acquisition may be envisaged. This is not thought to be a limitation in debugging mode.

The global clock is sent to the SPECS mezzanine whose configuration is such that it takes its clock from the CROC and becomes synchronous with the board.

The selected clock is also sent to the delay chip of the CROC. Two differential outputs of the delay chip are used in order to provide a clock to the boards of the crate that can be shifted by steps of 1ns over a 25ns range. The two others allow to tune the sampling of the FEB data with the registers of the Fe-PGA (see section called Data capture and treatment):

- The first tasks uses two outputs of the delay chip (that are configured accordingly through the slow control) that are multiplied up to 24 lines connected to the backplane connector of the card. This connector serves the 18 clock lines of the backplane (16 FEB and 2 validation boards for a typical calorimeter crate). The copy of the signal is done by LVDS to LVDS converter thus the critical paths of the clock propagated to the FEB are differential.

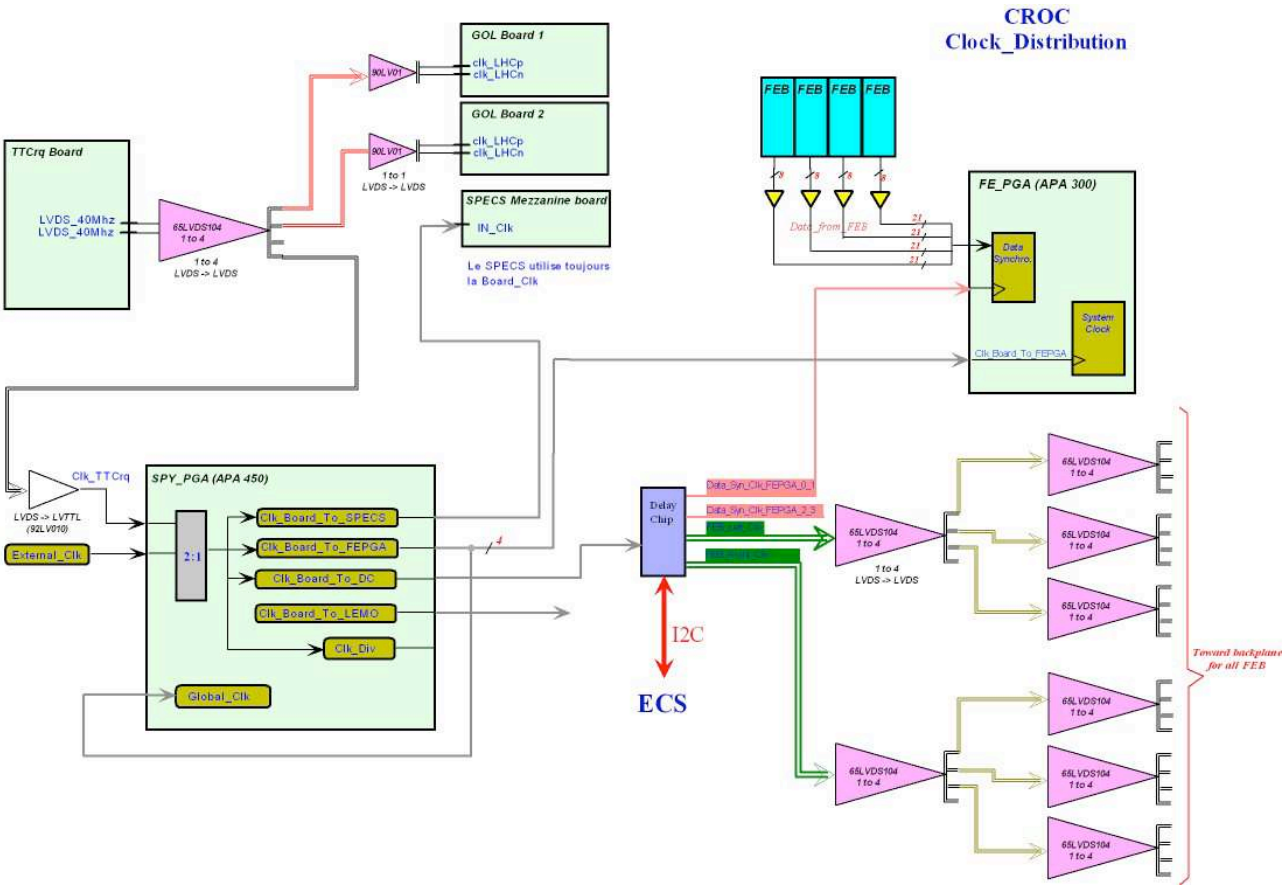

Figure 3.5: The CROC takes the clock signal either from the TTCrx chip located on the TTCrq mezzanine or from a user-provided clock (debugging purpose). The main clock phase may be adjusted before being propagated to the backplane through output drivers (bottom right). It is also sent directly to the optical and SPECS mezzanines. Two clock signals (an adjustable phase clock and the main CROC clock) are propagated to the Fe-PGA in order to capture the FEB data properly, in two stages.

- The data capture by the Fe-PGA is performed in two stages. We recall that the first one requires an adjustable clock. A delay chip output clock is sent to a pair of Fe-PGA, so that two outputs are used for the 4 Fe-PGA (a single output would have been too demanding) for this tuning. Notice that, the two delay chip outputs have the same configuration.

L0 Trigger

The L0 trigger signal is received from the TTCrq mezzanine board and is propagated to the Spy-PGA. The CROC has also the possibility to produce itself a debugging L0 signal for the crate. This is part of its debugging capabilities. After the input sampling of the TTCrq L0 by a register, a multiplexer allows the user to select either the TTCrq-L0 or the debug-L0 through a bit of the configuration register. Then, the signal is sent to the L0 bus of the backplane.

Broadcast Commands (Channel B)

The processing of the broadcast commands is similar to the L0 signal. The CROC has the ability to fake a channel B signal and a multiplexer allows the user to be in default (TTCrq broadcast) or debug (user defined commands) mode. The complication comes from the nature of the TTCrq broadcast signal which is static for 6 bits and 25ns long for the 2 reset bits (Bunch Crossing Id and Event Id reset). The clock of the TTCrq is used by the Spy-PGA to capture the static bits so that finally the 8 bits sent to the backplane are strobed or 25ns wide.

3.4.2 Fault

The FEB, the validation boards and the CROC itself (deserialisers only) are protected by delatchers MAX869 that detect a current increase that could be due, for example, to a single event latchup (SEL, see section 5). If such a situation occurs the current is switched off (during a few ms) and on again. The fault output line of the delatcher is pulled briefly to zero (the delatcher faults of a board are linked in parallel). The 18 lines of the 18 slots of the crate and the CROC protection switches are connected to 19 pins of the Spy-PGA which records any fault transition on those lines into its status register. The status register may be regularly checked in order to verify that no FEB has had a SEL and if this is the case, the corresponding FEB may be reloaded through the slow control.

The delatchers of the FEB and validation boards may also be commanded by the CROC. The same lines are used, but this time the CROC forces itself the line of the slot that requires a turn off to zero. The delatchers that see the line pulled down will switch off the current until the line is released. The line may be maintained down to have a prolonged stop of a board. The mechanism would be used in case of problems with the electronics and is triggered by a slow control command and the writing in a CROC register through the slow control.

3.4.3 The slow control

The configuration and control of the CROC is done with a SPECS mezzanine. The RJ45 connector of the front panel of the board receives the SPECS signal which is propagated with a bus down to the SPECS mezzanine bottom connector. A bus is used as the same SPECS signal is also sent to the backplane (slow control bus) in order to dialog with the SPECS slaves of the FEB (Glue PGA). According to the address encoded in the SPECS frame the corresponding slave will understand that it should read the data, the slave being either the CROC mezzanine or a Glue of a FEB.

Slow control transactions are done either through

- a parallel bus (FPGA),
- two I^2C buses (delay chip, TTCrq and optical mezzanines)

3.4.4 Resets

The main reset of the board is the SPECS reset signal. It is issued either from a slow control reset command or physically by pressing the reset button of the SPECS mezzanine (notice that

Location	Temperature (°C)
Black surface of the Agilent emitter , bottom of the OM(Right)	$\leq 49°C$
NIM converter M8 below OM(Right)	$\geq 54°C, \leq 60°C$
Fiber connector of the Agilent emitter , bottom of the OM(Left)	$\leq 49°C$
U4 GOL of the OM(Left)	$\leq 49°C$
U11 GOL of the OM (Left)	$\leq 49°C$
Clock driver U13 of the OM(Left)	$\geq 60°C, \leq 65°C$
Calorimeter FEB ADC facing the clock driver of the OM(Right)	$\geq 60°C, \leq 65°C$

Table 3.1: Temperature measurements on the CROC and in a ventilated crate. The GOL chips of the optical mezzanines (OM in the table) were configured in test mode for the measurements.

this second method also initializes the mezzanine itself).

The reset signal is propagated to the Spy-PGA. From the Spy-PGA, the reset is propagated (by combinatoric cells) to activate the reset of the major components/mezzanines of the board: the delay-chip, the four Fe-PGA, the TTCrq and the two optical mezzanines. Notice that from the Spy-PGA it is also possible to reset punctually one of those components or mezzanine (with a simple reset register slow control access) without affecting the others and the Spy-PGA.

3.5 Tests performed on the CROC and shielding

The CROC is the bottleneck through which all the data of the calorimeter system is flowing. I will describe here some intensive tests that have been performed to check that the board was functioning correctly. Some of these tests have been done at the experiment pit as their require the acquisition hardware (TELL1 boards) and a fraction of the PC farm to swallow the data sent by the CROC. We had also an LHCb acquisition board called TELL1 [50] that was connected to the LAL network. Hence, it was possible to perform acquisition in our laboratory.

3.5.1 Temperature measurements

The CROC has been heavily used without air flow cooling, on the table, with test bench power supplies. The heat released by the optical mezzanines and the NIM converters (see figure 3.6) pushed us to perform some temperature measurements in an environment closer to what we expect in the cavern.

Thus we plugged CROC in a crate full of 16 FEB until temperature stabilisation and after having glued temperature sensitive labels on the hotter parts of the board. The table 3.1 sums up the measurements and shows that we should not fear any over-temperature on the CROC.

3.5.2 Overall crate synchronisation

The CROC provides the clock to the boards of the crates and several important signals (first level trigger and fast commands). Moreover in return, it captures the data from the 16 FEB connected. The correct functioning of the system requires a proper tuning of the clocks, the

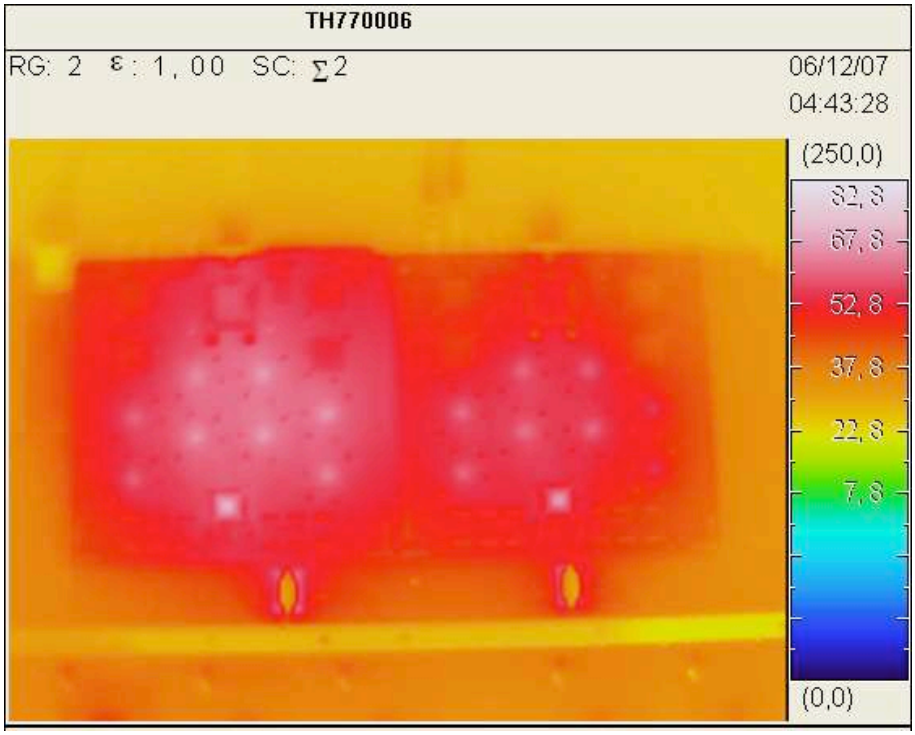

Figure 3.6: CROC temperature measurements with a thermic camera. The region showed is the optical mezzanine area where the GOL chips are clearly visible. On the PCB, below the mezzanine the NIM converters also contribute in heating the board.

degrees of freedom at the level of the CROC being the phase of the clock sent to the backplane (adjustable with a delay chip on the board) and the phase used to sample the data at the Fe-PGA inputs of the board. A 2D map was drawn in the space made from these two degrees of freedom. This map was re-evaluated for each CROC produced to verify it.

The FEB contain a memory to spy the data from the front-end. This memory can be used to feed the front-end with specific patterns. The synchronisation tests consisted in loading into the pattern memories of the FEB random but known values. The FEB are designed such that it is possible to loop on those memories.

The CROC was configured to produced 1MHz average frequency L0 triggers and to acquire the corresponding data. Errors are then counted in bins 1ns wide in the 2D map defined by the two clock degree of freedom of the board already mentioned. The structure indicates the forbidden regions corresponding to improper sampling of the signal.

As the CROC acquire a full crate, the "sum" of the 16 maps built from each of the FEB is plotted (see figure 3.7).

The stable region was required to be at least 5ns wide in all directions. This was demanding for the APA300 and APA450 components. The first plots measured had no stable region compatible with the 16 FEB inputs of a crate. This was due both to the fluctuations between the FEB outputs but also to the input drivers of the Fe-PGA of the CROC. Constraining the location of the registers responsible for the latching of the input data permitted to open

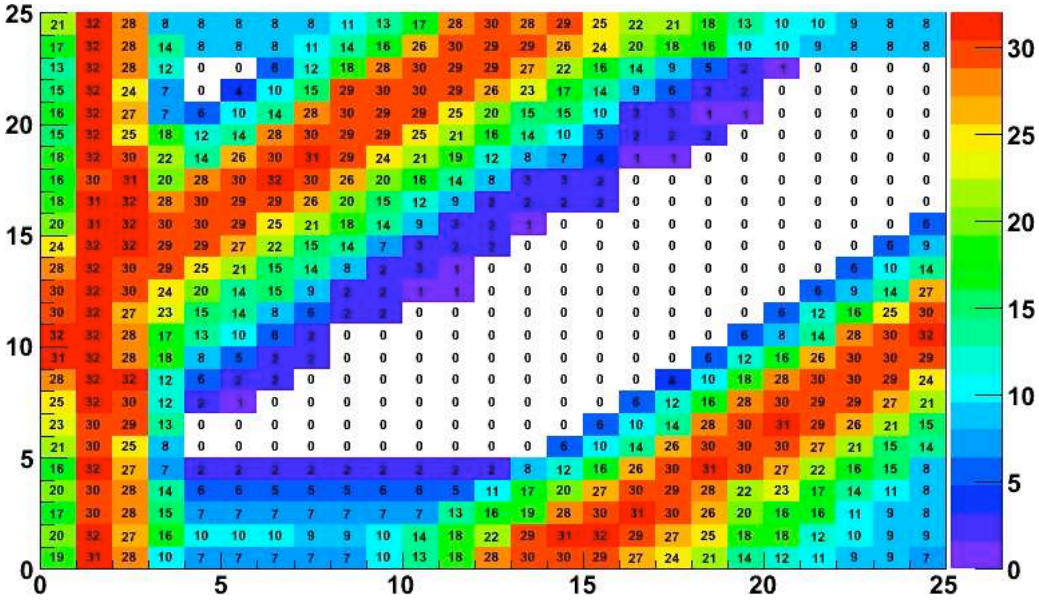

Figure 3.7: The stable and unstable timing regions of a CROC. The 2 axis are defined by the two degrees of freedom that are the phase of the clock sent to the FEB (y-axis) and the phase used by the board to capture the data sent back by the FEB. The numbers are coding of the errors seen. "0" means no error.

the stable region and to obtain satisfactory results. This measurement was part of the test production of the CROC.

Three regions appear on figure 3.7, one horizontal band and two diagonal ones. The width of the bands is mainly due to the only partial overlap of the allowed regions from each FEB.

- The horizontal band is due to the fact that a specific clock phase tuning of the FEB does not allow a stable sampling of the L0 trigger propagated (or generated) by the CROC at the level of the FEB.

- The diagonal band corresponds to the wrong capture of the data by the CROC. It is clear that changing the phase of the FEB modify the time arrival of the data at the input of the CROC and can be compensated by shifting the phase for the capture of the data. The two bands seen on figure 3.7 are in fact the extension of a single one over the full time period of 25ns.

3.5.3 Bit error rates

The TELL1 board receives the data from the CROC through 16 optical fibres gathered in two 8 fibre ribbons. Each ribbon corresponds to the left and right parts of a crate. The TELL1 are located in the LHCb counting room and dispatch the events to the large PC farm of the experiment. The data transmission between the CROC and the TELL1 was tested by performing bit error rate (BER) measurements.

Conditions	Bit Error Rate (transf. bits)
8 fibres (no attenuation)	148×10^{12}
16 fibres (no attenuation)	66×10^{12}
16 fibres (no attenuation)	130×10^{12}
8 fibres (6db)	15×10^{12}
8 fibres (9db)	30×10^{12}
16 fibres (6db + 9db)	350×10^{12}
16 fibres (9db + 6db)	350×10^{12}

Table 3.2: Examples of fibre transmission tests performed with different combinations of attenuator and without error.

This was possible by programming the CROC so that the fibre outputs were simple counters. The TELL1 that we had a our disposal at LAL was configured in order to check the counters. Any error was recorded in a TELL1 register.

The test has been done without light attenuators and with attenuators of 6db and 9db. The typical attenuation expected with the multi-mode fibres used is of the order of 2.8db/km, the distance between the CROC and the cavern being of about 100m. A patch panel is used on the fibre path, nevertheless 9db is far from what is expected at the pit.

The level of accuracy reached (no error recorded) with 9db attenuators (test performed on the left and right fibre ribbons) is of the order of several 10^{14} (see table 3.2). This test was also part of the production test performed on the boards.

3.5.4 1 MHz test at the pit

The CROC processing speed depends on the L0 trigger rate. The maximum average speed reaches 1.1 MHz. This limit permits to the CROC to run with a 40MHz clock, an event requiring 36 clock beats to be readout:

- 2 empty words for the fibre synchronisation,
- the header,
- the control word,
- 32 channels words.

Hence, the "effective" read out of the CROC is performed at 40MHz for 16 FEB. This is a huge among of data swallowed by 4 Fe-PGA. The frequency and the number of bits flipping per FPGA is a major concern and was a difficulty in the design of the firmware of the board.

The first test showed that when running in extreme conditions, the data transmitted were rapidly corrupted. This is shown on figure 3.8 were the input data were 34 oscillating values followed by the 2 empty words for fibre synchronisation. Such a pattern sent on all the input caused the FPGA to react in a strange way. Redirecting an input bit towards an output driver showed that the emulated clock rapidly changed its duty cycle until the data became corrupted

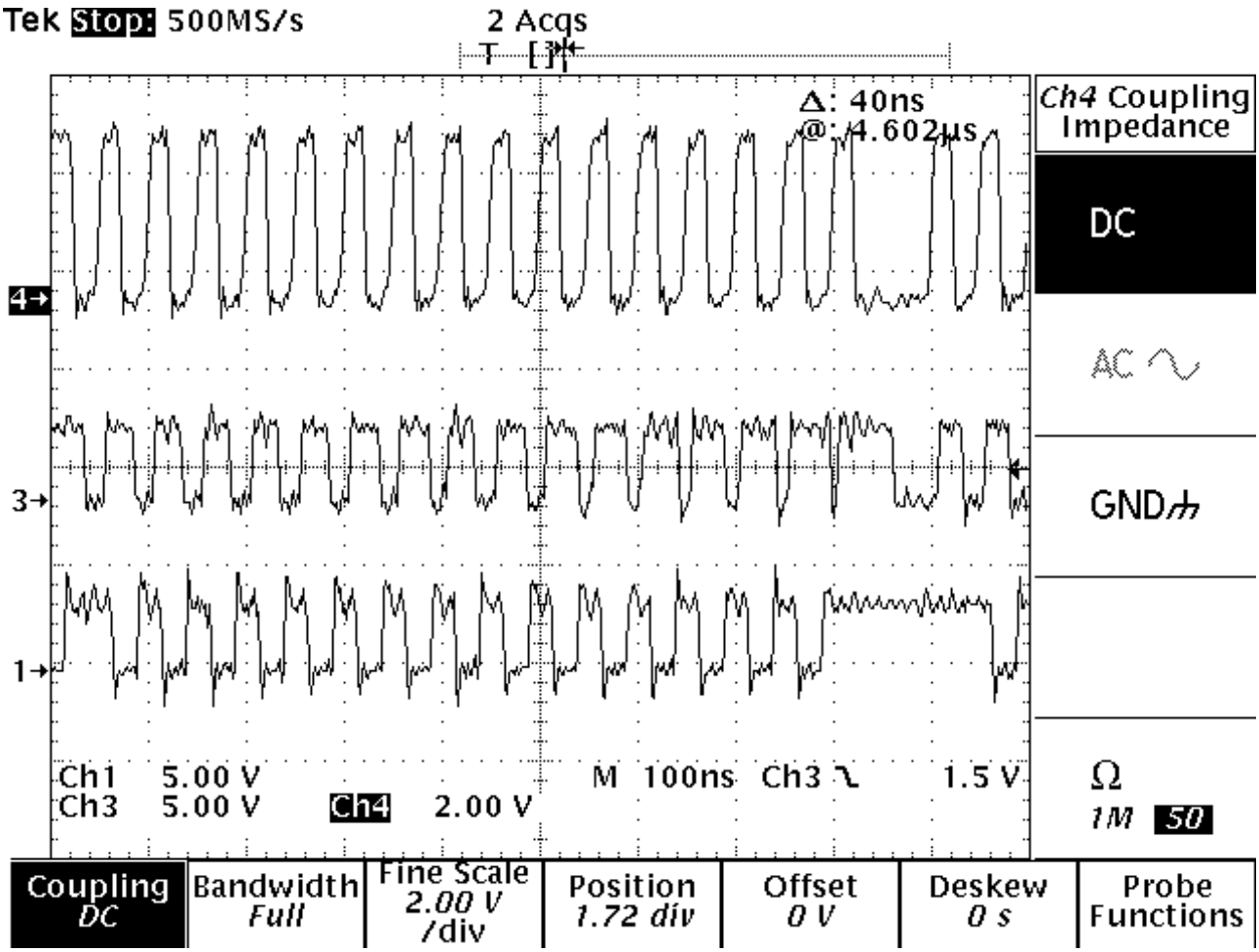

Figure 3.8: The three curves show the signal injected (top), the input data redirected towards an output buffer (no processing, middle curve) and the processing by the CROC of the input data. It is clear that even without any processing by the boards, the data are corrupted (second line).

and could not be properly sampled (second line of 3.8). This was identified as being probably caused by a drift of the internal power levels used to acquire the bits[4]. The package bonding of an FPGA may be modelized with an inductance L. The internal levels may shift by a quantity $V = L\frac{di}{dt}$. A rapidly oscillating current i (due to the flipping of the bits) may lead to a large drift of the internal levels.

This problem for such components is known but scarcely advertised or documented by the manufacturer. Moreover it is very specific to an application and cannot be easily predicted. Two solutions have been applied to cure it.

- The registers responsible for the latching of the bits have been split apart on the chip surface.

[4]The FPGA input is made of a comparator of the input bit level with a fraction of the component power level.

- The timing of the output bits has been modified so that all the bits were not flipping at the same time. This was possible by inserting a combinatoric cell just before the output drivers.

The solutions have been first verified on test bench. A second test was performed early at the LHCb pit as soon as a large enough PC farm was installed. We cabled a few TELL1 and emulated 1.1MHz triggers. The acquisition with the farm at the fastest speed did not permit to see any error for several hours.

No error was observed at the pit and the solutions were validated.

3.5.5 CROC shielding

The FEB noise is expected to reach 1.2 ADC count. This was measured with several FEB in a crate, but not with an average trigger rate of 1.1MHz and on a long time scale. Such an acquisition could not be done in our lab. At the pit, the PC farm being installed, it was possible to perform more intensive noise measurements. No deviation from this estimation have been seen but for the one FEB located on the left slot of the CROC.

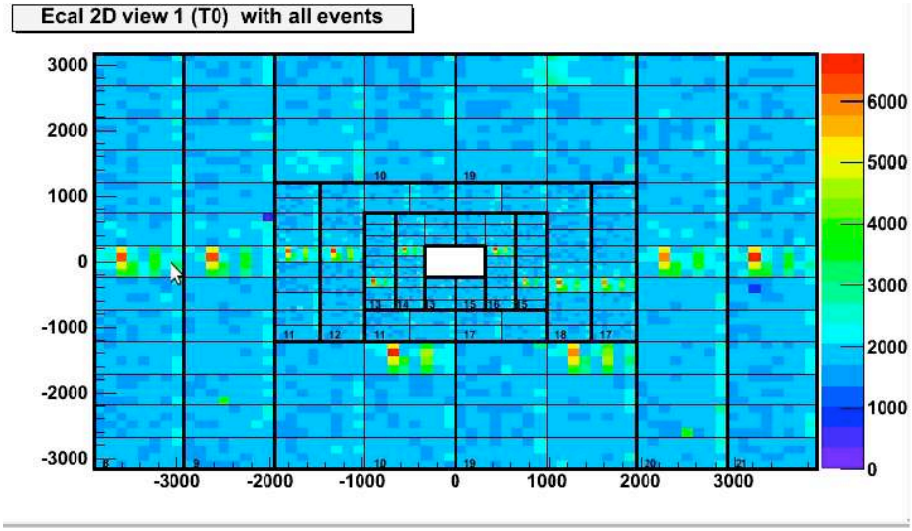

Figure 3.9: Summing the calorimeter signals of many events over the detector surface showed a regular pattern. This was interpreted has a slightly larger noise on every FEB located at the left of the CROC. Notice that the events are exclusively noise events, and the excess had only an amplitude of a fraction of ADC.

The figure 3.9 shows the result of summing the channels outputs over the full detector surface and on a large data sample. The data are only noise events. The average being subtracted, the increasing of this sum is slow. The channels having a noise in excess will have this sum increasing slightly faster. This is observed here.

Notice that the extra noise amount is very small and we have never been able to observe it on test bench with a sophisticated oscilloscope even when we tried to track it. All the tests have been done at the pit where we could have fast and long enough acquisitions to exhibit the

effect. Should the acquisition not be performed on noise only, the z axis of figure 3.9 would be smashed and the regular pattern observed would completely disappear. Nevertheless, we tried to get rid of it.

The origin of the problem was finally identified as being a crosstalk between PCB lines on the CROC bottom face and the neighbouring FEB. The FEB shaper requires, to filter fast frequency noise, to use a large value capacitance (of the order of a few nF). Such a capacitance cannot be easily made in an ASIC and the shaper signal between the buffer and integrator had to be extracted out of the chip to be filtered and injected again. The location of this capacitor was right at the level of a few CROC PCB lines used to feed the GOL chip. The high frequency test performed at the pit was done again after having covered the CROC lines with a shielding made of a conductive layer connected to the ground.

The noise measured disappeared and no regular pattern could be seen afterwards[5]. Then, it was decided to have all the CROC modified in July 2009. A PCB layer covered with 35μm of copper was designed and manufactured to shield the CROC PCB lines. The shielding was screwed and soldered on the ground of all the boards during summer 2009.

[5]The effect has never been directly seen. It was first expected to come from the interplay of the capacitance with the CROC PCB lines. This was proven by the final tests.

Chapter 4

Control and acquisition software

Contents

4.1 Software for the electronics 69

4.2 Tests of the front-end boards 71

The development, test after production, installation and commissioning of the electronics required a specific software that was written from 2004. This software will be briefly presented here. Its usage to test the front-end board production will be also described.

4.1 Software for the electronics

The first prototype for the electronics of LHCb was running in a VME crate and was controlled with an old MAC computer. It was rapidly necessary to develop another software that would be compatible with the platforms chosen for LHCb: Windows and Linux. Moreover, the electronics of the calorimeter was including different interconnected systems, from the very front-end, to the front-end, the control boards, the trigger validation boards, the LED calibration electronics, the Cockcroft-Walton [34] power, etc ... The development of a single framework that could control all these pieces was a great help. It reduced the overall work for the different groups involved, as a large fraction of the software was common. Moreover, from 2005, many integrated tests had to take place at CERN and it was easy to interconnect the electronics boards of the different calorimeter groups through a single computer and a single software, able to run automated acquisitions, to trigger events, to perform scans, to react to some situations or to check online that the data were not corrupted.

The program used by the LHCb calorimeter group is called CAT for "Calorimeter Acquisition and Task". This program runs under Windows and Linux and includes several interfaces to the electronics: USB, SPECS[1][30][31] and GPIB. It may communicate through these interfaces to the electronics using either parallel or I^2C bus.

[1] The SPECS interface was developed at LAL to perform slow control operations on some part of the electronics located in the cavern where the radiation levels did not permit to use, for example, credit card PC systems.

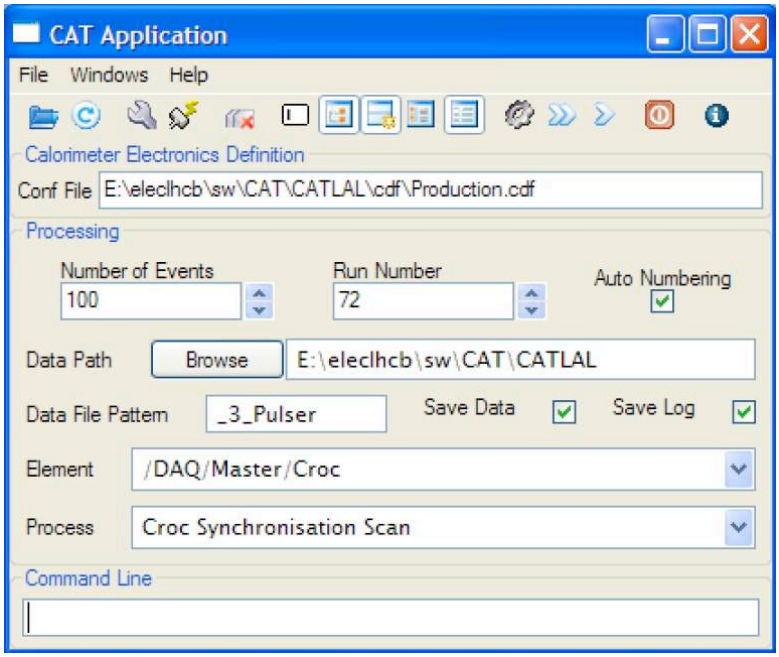

Figure 4.1: The main application window of the CAT program. The control of the program is performed on the top lines. The configuration file loaded at start up is indicated below. The processing part permits to launch runs of acquisitions, tests or measurements.

The program may be used in two different modes: graphical[2] and text. The graphical mode contains several windows:

- The main application window to control the program, load configuration files for the electronics or launch automated sequences of operations (see picture 4.1).
- The configuration window shows configuration panels for the electronics parts under control. It is possible to check the internal configuration and to perform manual adjustments.
- The graphical window shows the results of the automated sequences as curves or histograms (see figures 4.2 and 4.3).
- The log window is the text output of the program and can be used to display tables of results.

The graphical interface is mainly useful for development and debugging of the electronics. The text mode can be used to launch automated operations that do not require any online control or to work remotely on a low bandwidth network. The user types commands instead of pressing buttons in order to control or run its systems. The text mode output is identical to the graphical mode log window output. CAT uses the "ROOT" analysis package for data storage [87].

[2]The graphical implementation is based on wxWidgets[93]

The CAT program is written in C++. The latest version, that is now used for the development of the electronics for the upgrade of the calorimeter, includes a full interfacing with python [86] so that the electronics can be controlled from the python console[3] or as before with a full graphical interface. Nevertheless, the processing that requires speed is still done in C++.

The program CAT consists of a set of libraries having a dedicated purpose. A few ones are mandatory and are the core of the software (the framework, a list of generic objects, the interfaces to the electronics, ...). The user may load at run time any other necessary library for the specific tasks he wants to perform. A library usually contains the definition of electronics systems (boards, for example), the tasks that may be launched on it and the description of the corresponding configuration graphical panels. Such a library defines a user library whose objects should inherit from the generic objects included in the core part of the program.

The development of the user libraries has given the possibility to different groups (CERN, Spanish, Russian, Annecy, Clermont-Ferrand and Orsay) to contribute to CAT, the core software and the libraries written being hosted at CERN.

CAT was used for the development of the electronics and the production tests. During installation and commissioning, it allowed to test the cabling of the trigger and the good connections among the different types of boards. The FEB includes a pulse injection system at the board signal input. The pulse reflections can be easily used to test the connections between the front-end boards and the photomultipliers. The control of the functioning of the boards using RAM patterns is also done with CAT. Many communications (between the FEB and Trigger Validation boards, for example) require the tuning of local clock phases with delay chip. CAT is routinely used to extract the actual correct phase adjustment by performing time scans.

Although the control of the electronics by the shift crew during data taking uses PVSS[4], the control of the good performances of the electronics is still largely done with CAT at the pit.

4.2 Tests of the front-end boards

The electronics produced for the LHCb calorimeter systems have been mostly tested with CAT. This is the case of the front-end of the calorimeter system.

The tests of the 300 ECAL/HCAL boards were done with a crate containing up to 8 boards [5]. Such a group of boards was tested in 8 hours on average. The control of the production was fully automated, the operator had to give some information on the boards at start-up for future tracing of the tests. At the end of the run the output was kept altogether with the root data files and a summary was printed. Three runs where launched per days. The acquisition of the front-end boards was done by a control board (CROC) whose debugging and acquisition capabilities will not be presented in this document (see [38]).

- Slow control: The proper control of each board was the first aspect of the electronics to

[3]The integration of the C++ libraries into the python script is done with the BOOST libraries [11]

[4]PVSS is the slow control program used by the LHC experiments[85].

[5]A crate contains up to 16 front-end boards, but the test of the trigger processing was more conveniently performed on half a crate, leading to this choice.

be checked. All the registers of the FPGA and phasers were randomly written and read out. The RAM were also tested by loading large amount of data and controlling that no error occurred.

- Synchronisation: Two main clock domains are used in parallel on the front-end electronics and permit an optimum running of the acquisition of the FEB. To set and thoroughly control the FEB timing and the phasers, the two dimensional plots explained in section 3.5.2 are produced.

- ADC bit connection: From time to time a pin or bit of an ADC was not properly soldered. This problem is particularly obvious to track when the larger significant bits are affected. The lowest ones could sometimes be more difficult to identify. On the FEB a pulser system is implemented and can be triggered by a slow control command to the FPGA. The pulse is injected at the physics signal input of the FEB and fakes a photomultiplier charge injection. The ADC connection test consists in sending several consecutive L0 and triggering a pulse for one of them. For each one of these pulses the number of "0" and "1" of every bit of the 32 ADC are stored. In order to reach each bit, the test is performed several times with different delays between the pulse and the capture of the corresponding integration by the ADC. This allows to sample the maximum of the integration curve and its borders and to fake many signal amplitudes with a single original pulser amplitude and reach all the bits.

  In fact, the bit 12 could not always be tested as the maximum amplitude of the pulser do not systematically reach 2048. This limitation reduced the power of the test for this particular bit.

- Noise: The noise was systematically measured on the boards tested. Figure 4.2 shows the results of the tests on a full crate. Each column is the result for a slot (or a FEB). The top line corresponds to the data recorded during the test, the middle one is the average value per channel and the bottom line is the standard deviation per channel. The values obtained are compared to reference measurements.

- Pulser: The acquisition of sequences of 5 consecutive events was performed, a pulse being triggered at the position of the third event. The average amplitude measured per channel and their standard deviation for the 5 consecutive pulses was stored and compared to reference values. Another recurrent problem identified with this test was due to broken delay line leading to a bad reset of the shaper integration. Figure 4.3 shows the data measured for every slot of the crate (a slot is a column on the figure), the row being from top to bottom the event $(t0 - 1)$, the central event $t0$ with the pulse, the following one $(t0 + 1)$ and finally at the bottom the events $t0 - 2$ and $t0 + 2$ superimposed.

- RAM test: A RAM pattern is implemented on the FEB and allows to inject, at the input of the Fe-PGA, values faking the ADC outputs. The final test that was also the longer one consisted in loading the RAM with well-known patterns and to loop on those RAM. L0 were triggered by the CROC that performed the acquisition of the corresponding data. The PC could then compare the data recorded with that expected from the processing of the RAM patterns originally loaded in the FEB under test. The comparison was

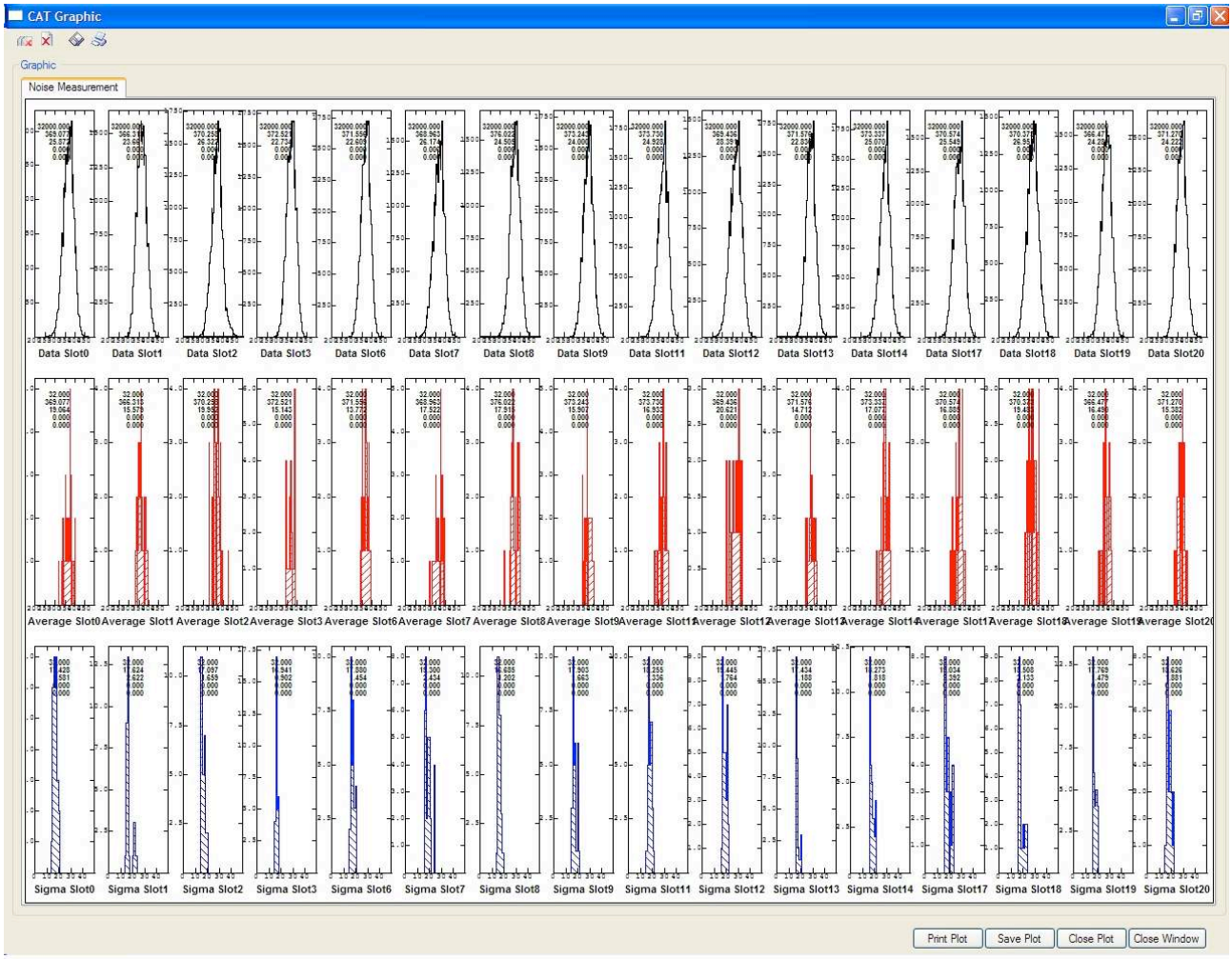

Figure 4.2: Result of a noise test in a full crate. The columns correspond to the FEB or slots. The top line is the accumulation of the data. The second and third rows are the average and standard deviation per channel.

interrupted from time to time in order to load into the RAM a new set of random but well-known patterns. The full numerical processing could be checked down to the CROC board.

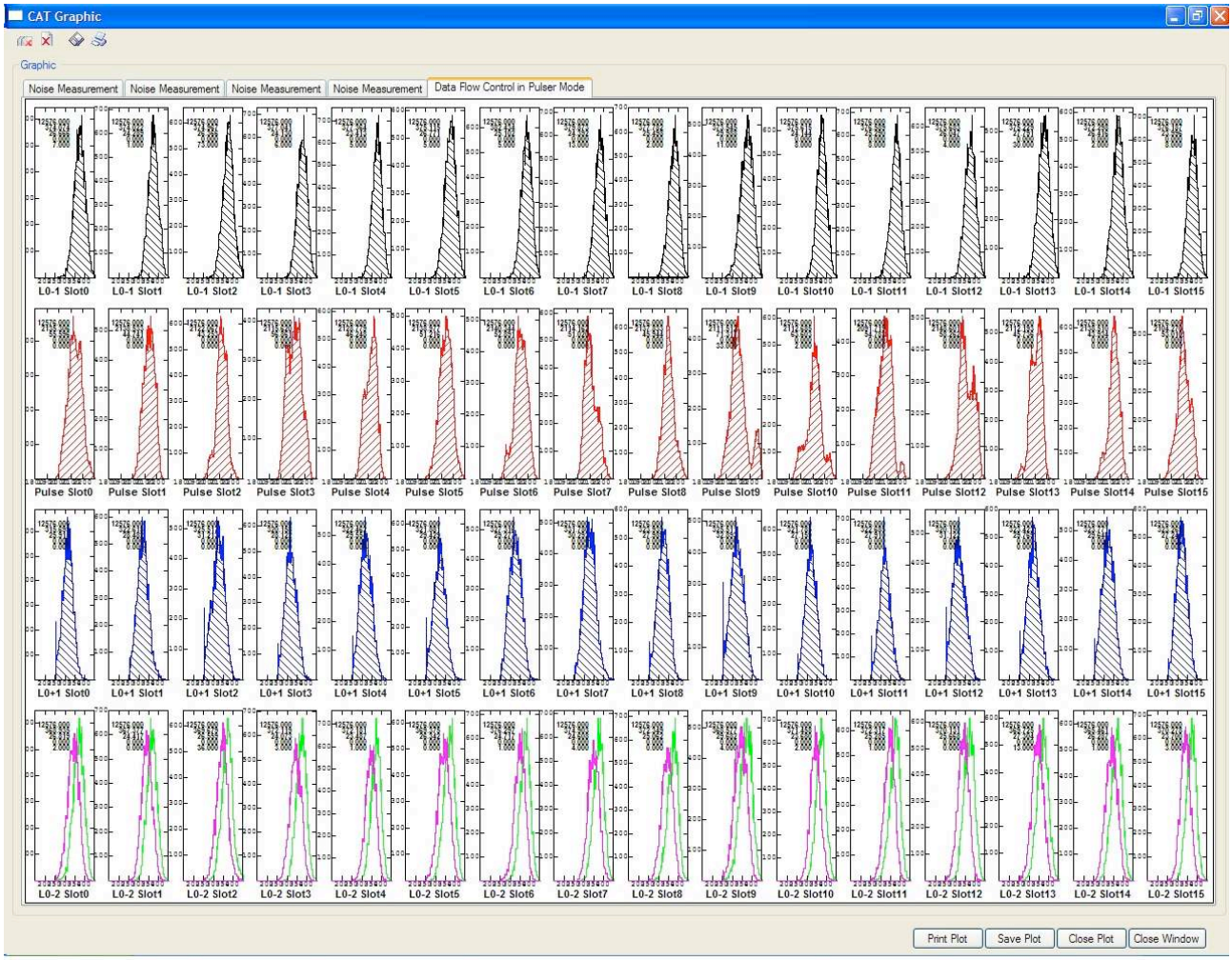

Figure 4.3: The final result of a pulser test performed on a full crate. Each column corresponds to a slot. From top to bottom, the rows are the event $t0-1$, the $t0$ event when the pulse occurred, the $t0+1$ one and on the last row the two events $t0-2$ and $t0+2$.

Chapter 5

Radiation tolerance of the electronics

Contents

5.1 Introduction 75
5.2 LHCb environment 76
5.2.1 Particle flux 76
5.3 Irradiations of the calorimeter front-end shaper 79
5.3.1 Irradiation at the Centre de Proton Thérapie 79
5.3.2 Irradiation at GANIL 81
5.4 FPGA radiation tolerance 87
5.4.1 Dose, single event latchup and single event dielectric rupture 87
5.4.2 Single event upset cross-sections 89
5.4.3 Single event upset and clock upset rate estimations 90
5.4.4 LHCb front-end FPGA sensitivity and protections foreseen 93
5.5 Summary table and conclusion 97

5.1 Introduction

Two types of radiation effects could potentially affect the LHCb calorimeter front-end electronics: cumulative dose and single event effects (SEE). The former has two contributions:

- Total ionizing dose: the creation of electron-hole pairs in the component degrades its behavior.
- Displacement damage: atoms are displaced from their initial position because of non-ionizing energy losses. The characteristics of the component are progressively degraded.

The SEEs are due to a single incident particle interacting with the component medium. The main manifestations of SEEs are the following:

- Single Event Upset (SEU): the medium energy incident particle breaks a silicon nucleus and produces a highly ionizing nuclear recoil. The consequences for the component may be bit flips (RAM-FPGA) and modifications of the configurations (FPGA). This problem is solved by a reload of the corrupted bits.
- Single Event Latchup (SEL): the incident particle breaks a silicon nucleus. The debris of the reaction trigger a short-circuit in the chip which may be destroyed. The SEL could potentially affect both commercial parts and the calorimeter front-end shaper.
- Single Event Transient (SET): likewise, the incident particle indirectly causes the ionization of a region of the component. Then, charge collection leads to the production of a fake signal in the part.

Section 5.2 will be devoted on the evaluation of the flux of particles in the electronics zone. Then, the results of the front-end shaper irradiation tests performed at the Centre de Proton Thérapie of Orsay (CPO) and at the Grand Accélérateur National d'Ions Lourds (GANIL) are given. In the last section, the SEE risks is evaluated for the AX1000 FPGA and transposed to the front-end electronics design.

5.2 LHCb environment

5.2.1 Particle flux

Radiation doses at the position of the calorimeter crates have already been estimated (see references [59, 91, 62]). The predicted level reaches 100 rad per year and no serious cumulative radiation damage of electronics are expected.

Non-ionizing effect at the level of the calorimeter is not a problem either, as the flux of neutrons and the corresponding cross-sections (see figure 5.1) are such that no effect should be expected during the full life of the experiment[4].

The only serious problem of concern for the calorimeter electronics is the one of single event effects [68]. The estimation of the SEE risk requires the determination of the particle flux and energy spectra in the region of the front-end electronics. The corresponding curves have been calculated from a Monte Carlo pp interaction sample of 5000 events[1]. The processes selected for the production were QCD processes, as defined by PYTHIA (MSEL=2). They are listed in table 5.1 together with the cross-sections, as calculated during the generation.

The flux has been normalized to a luminosity $\mathcal{L} = 5 \times 10^{32}\text{cm}^{-2}\text{s}^{-1}$. This value is rather large compared to the nominal luminosity which is currently expected to be $2 \times 10^{32}\text{cm}^{-2}\text{s}^{-1}$. Figure 5.2 shows the particle (π and K mesons, protons and neutrons) flux ($\text{cm}^{-2}\text{year}^{-1}$) at two depth values along the z direction: 12.30m (at the level of the front of the SPD/PS) and 13.32m (at the level of the back of the ECAL). The red box gives a rough indication of the crate position; the black box shows the area (1m high and 4m wide) located 3.5m above the proton beam on which the particle flux is averaged to determine the energy spectrum. This last area is not the rack zone, but it is a region around the point of the electronics where the flux is expected to be the largest (i.e. at the bottom center).

[1] The Monte Carlo sample has been produced with SICBMC v245r1 [77].

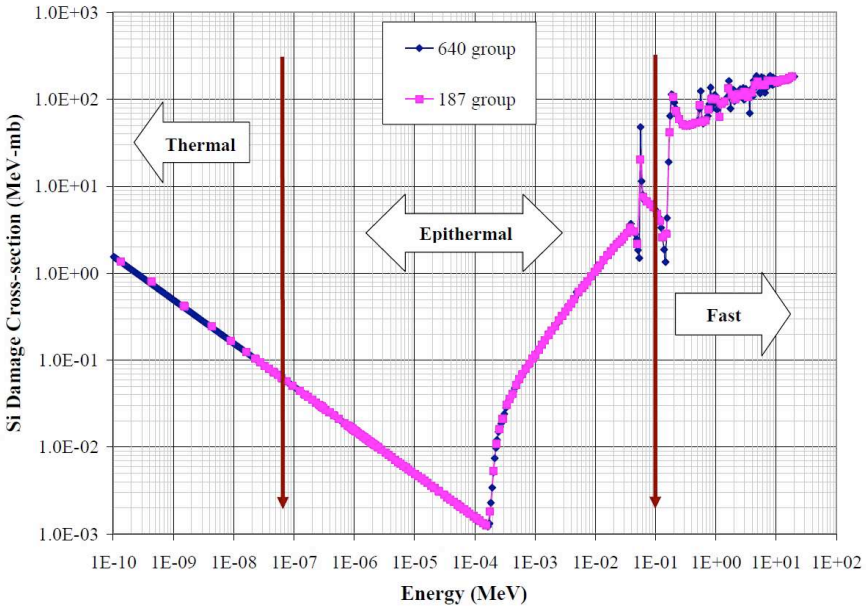

Figure 5.1: Silicon damage cross-section as a function of neutron energy (from [4]).

Sub-processes	Cross-Section (mb)
$f + f\prime \to f + f\prime$	11.12
$f + \bar{f} \to f\prime + \bar{f}\prime$	0.0
$f + \bar{f} \to g + g$	0.0
$f + g \to f + g$	10.74
$g + g \to f + \bar{f}$	0.5752
$g + g \to g + g$	32.79
Elastic scattering	22.21
Single diffractive (XB)	7.151
Single diffractive (AX)	7.151
Double diffractive	9.779
low p_t scattering	0.0
All included subprocesses	101.5

Table 5.1: Processes generated by PYTHIA (MSEL=2) to evaluate the particle flux in the electronics area of the calorimeter [77].

The flux estimation does not take into account any Hubner factor, but more simply relies on the 10^7s running of the machine hypothesis[2].

Figure 5.3 shows the obtained energy spectrum for π and K mesons, protons, neutrons at $z = 12.30$meters. Among the various contributions, neutron's is by far the dominant one below

[2]A more realistic scenario foresees 7 months of data taking in a year, with a Hubner factor of 0.2, leading to 3.7×10^6s.

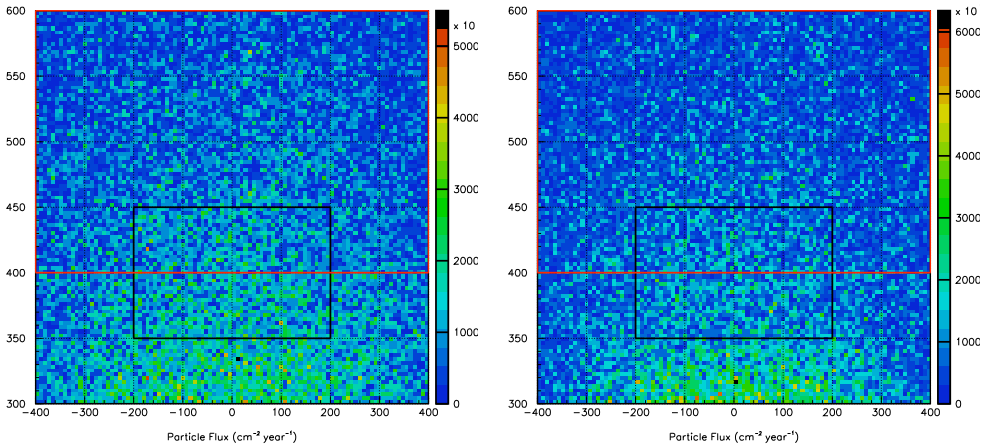

Figure 5.2: Particle flux ($\mathrm{cm}^{-2}\mathrm{year}^{-1}$) in two rectangular areas (left plot at $z = 12.30$m, right plot at $z = 13.32$m) above the proton beam (x and y axis in cm). The red box roughly indicates the position of the electronics; the black one shows the area where the flux has been averaged to produce figure 5.3.

100MeV.

A fit has been performed on the total energy spectrum at the two different z depths. The function

$$f(x) = Ae^{-Bx} + Cx^D \tag{5.1}$$

was used, where the exponential describes the low energy part and the power law corresponds to higher momentum particles. The parameter values are given in table 5.2 and the curves are shown on figure 5.3.

parameter	$z = 12.30$m	$z = 13.32$m
A ($\mathrm{cm}^{-2}\mathrm{year}^{-1}\mathrm{MeV}^{-1}$)	2.2×10^9	1.8×10^9
B (MeV^{-1})	0.27	0.28
C	0.43×10^9	0.49×10^9
D	-0.87	-0.89

Table 5.2: Fitted parameters for the total energy spectrum evaluated at the two z positions, 12.30 and 13.32m. The function used is (5.1).

Two populations are observed in the electronics region. Low energy particles are isotropic neutrons produced in the matter of the detector. A second population consists of higher energy particles moving forward and produced close to the interaction region.

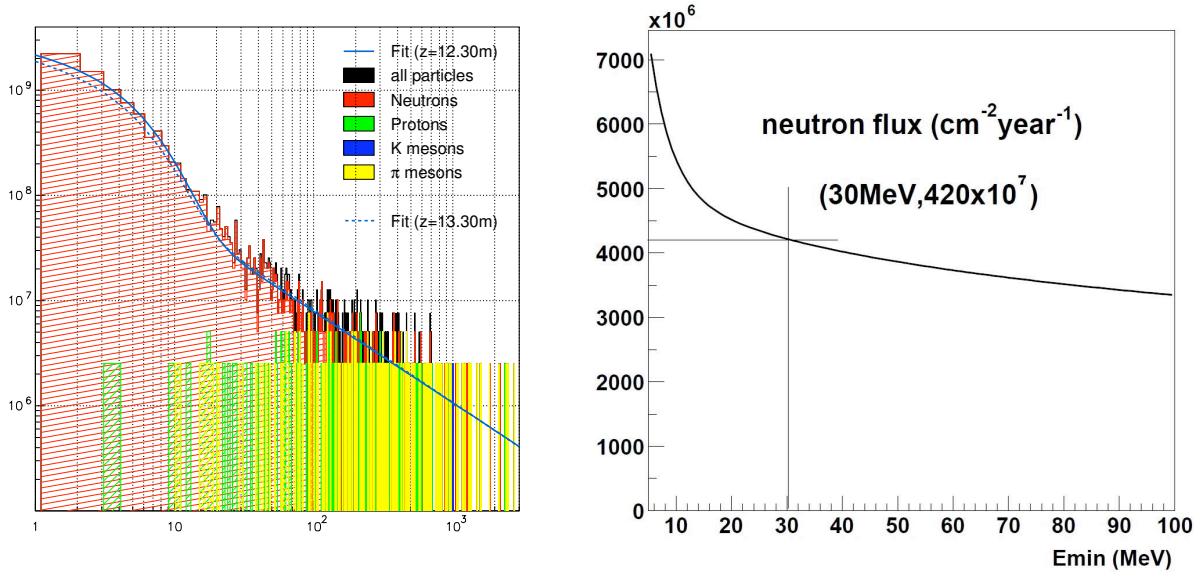

Figure 5.3: Left: the figure shows the particle spectrum ($\mathrm{cm}^{-2}\mathrm{year}^{-1}\mathrm{MeV}^{-1}$) in the rectangular region defined on plot 5.2 (empty black box) and in the text. The position where the histograms have been calculated is $z = 12.30\mathrm{m}$. Two fits have been performed on the total particle spectra, for $z = 12.30\mathrm{m}$ and $z = 13.30\mathrm{m}$. Right: the integrated number of neutrons above a certain kinetic energy. From the SEL/SEU cross-section which have been measured on typical components, neutrons below 30MeV are not supposed to have an effect on the electronics. 4.2×10^9 neutrons above this threshold are expected per year and per square cm in the vicinity of our electronics.

5.3 Irradiations of the calorimeter front-end shaper

Although they are not concerned by SEU, analogic chips can potentially be affected by SEL. Two irradiation tests have been performed at the Centre de Proton Thérapie d'Orsay (CPO) and at the Grand Accélérateur National d'Ions Lourds (GANIL) in very different conditions (CPO provides protons at 200MeV and GANIL is a heavy ion accelerator) on the calorimeter front-end shaper to evaluate the sensitivity of the chip [39].

5.3.1 Irradiation at the Centre de Proton Thérapie

The Centre de Proton Thérapie at Orsay (CPO) is an institute for the treatment of patients suffering from cancer. The cells located in the brain or in the eye are killed by an intense proton beam. This type of treatment has the advantage of making the most of the Bragg peak of the particles: the energy deposit is limited to the tumor region and avoids irradiation of healthy tissues.

The conditions of the test were a flux of $10^8\mathrm{cm}^{-2}\mathrm{s}^{-1}$ and a kinetic energy of 200MeV. The diameter of the beam was 4cm. Assuming that a 200MeV proton deposits $4\mathrm{MeV.mg}^{-1}\mathrm{cm}^2$, the dose accumulated reaches $6.5\mathrm{rad.s}^{-1}$. The setup is shown on figure 5.4 with a description of the system.

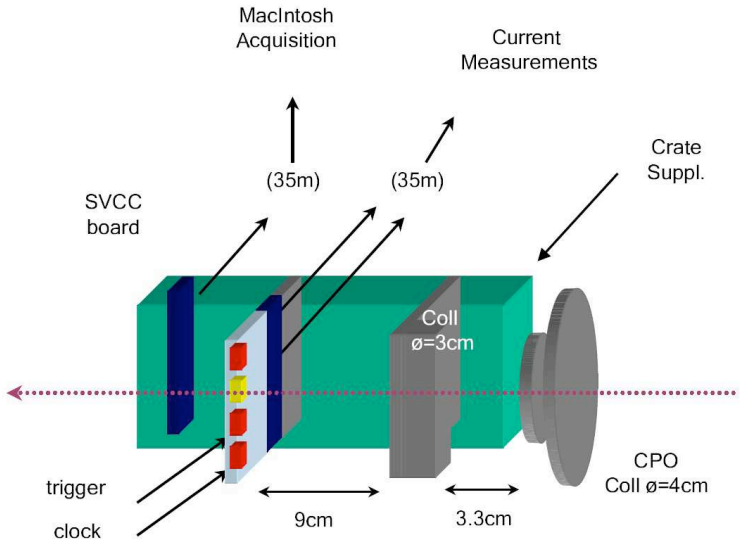

Figure 5.4: Schematics of the shaper irradiation test at CPO. The color code chosen is the following: the crate is in green, the inactive parts (collimators, extension board) are in gray, the tested electronics is in red and yellow (yellow for the chip presently showed in the beam) and the sensitive electronics for the acquisition is in dark blue. The dotted magenta line is the proton beam. The height of the crate was adjustable so that the four chips could be presented to the beam. Two signals (40MHz clock and trigger) were brought to the board. The acquisition was performed by the front-end board itself and by a SVCC board (interface between the crate and the acquisition computer used during this specific test) located in the same crate. To move the acquisition electronics away from the beam the front-end board was plugged on an extension.

The measurements performed during the irradiation were:

- pedestal runs (no input signal),
- calibration runs: a signal is generated on the board and injected at the signal input,
- front-end shaper current measurements.

A SEL should manifest itself by a large increase of the current of a chip. In the same time, a malfunction should be detected from pedestal and/or calibration runs. During the irradiation and in spite of the duration of the test, we observed

- no variation of the supply currents of the chips,
- no variation of the signal noise,
- no variation of the recorded calibration signal.

Supposing that the SEL cross-section is negligible below 30MeV (see [46, 54] and the justification given at the end of the next section 5.3.2 devoted to the GANIL irradiation) and using

the estimation for the neutron flux above this threshold (see previous section), a year of data taking with LHCb is roughly equivalent to 40s of test at CPO. A summary of the irradiations for the four tested chips is given in table 5.3.

Component	Duration (s)	Dose (krad)	Equivalent exposure (year)
1	3479 (~ 1h)	22.6	87
2	1643 (~ 1/2h)	10.7	41
3	1896 (~ 1/2h)	12.3	47
4	1800(~ 1/2h)	11.7	45

Table 5.3: Irradiation duration, dose accumulated and equivalent exposure at LHCb (a year is supposed to be 10^7s) for the four tested front-end shapers.

The dose accumulated (from 10.7 to 22.6krad) was by far larger than what we can expect in 10 years of functioning of the detector. A total of 220 years[3] has been tested without any SEL.

The four chips have since been thoroughly tested on the LAL test bench. The following points have been looked at:

- output buffer/integrator tensions,
- rise/fall time of the integrator,
- output signal plateau,
- linearity,
- crosstalk,
- noise.

The four chips had the same characteristics after the test as before the irradiation.

In spite of the good results obtained, it is important to notice that the sample is very limited. 2000 chips are used on the calorimeters, and 220 years for one chip is roughly 40 days for the electromagnetic and hadronic calorimeters. Although the result was very encouraging, this limitation was the motivation for an irradiation at GANIL in different conditions and leading to a better resistance estimation.

5.3.2 Irradiation at GANIL

GANIL (Grand Accélérateur National d'Ions Lourds) is an accelerator located at Caen in Normandie, whose purpose is to provide heavy ion beams reaching energies up to 90MeV/A for nuclear physics experiments. At CPO, the incident particles interact with the silicon nucleus and produce a ionizing fragment capable of triggering a SEL. At GANIL, the incident particle is the ionizing fragment which explains the efficiency of the test.

[3] A year is 10^7s.

Although it is far easier to get high proton fluences, the probability for a proton to produce a ionizing fragment from a collision with a silicon nucleus is of the order of $10^{-7}\mu\text{m}^{-1}$ (see plot 5.7). This will explain the relative inefficiency of the CPO experiment and the power of the GANIL tests where the projectiles are the ionizing fragments. Although the fluences at GANIL are far lower the "equivalent LHCb operation time" is by far longer.

It should also be pointed out that proton tests may lead to relatively fast dose deposition although, in our case, the danger comes mainly from SEE. An unadapted test with protons may lead to the death of the component by the cumulative dose before the statistics is large enough to extract relevant SEE measurements.

We took the opportunity of a foreseen run at GANIL with Krypton ions at 58MeV/A that were particularly well-adapted to our requirements to perform parasitic irradiation tests. Our needs were to deposit in the chip an energy along the path of the ion (called LET for Linear Energy Transfer, in the following), equivalent or slightly larger than what we could indirectly get with neutrons at LHCb, i.e. roughly $15\text{MeV.mg}^{-1}\text{cm}^2$.

We had three hours at our disposal for the test and we divided that time interval in two periods. During each period two chips were simultaneously irradiated, each period being divided into four runs corresponding to four different deposited LET. Between two consecutive runs, the LET was modified by introducing different layers of aluminium between the vacuum pipe aperture and the irradiated chips. Four chips have been used during the test: two during the first period and two during the second one. The run conditions of the two periods and the

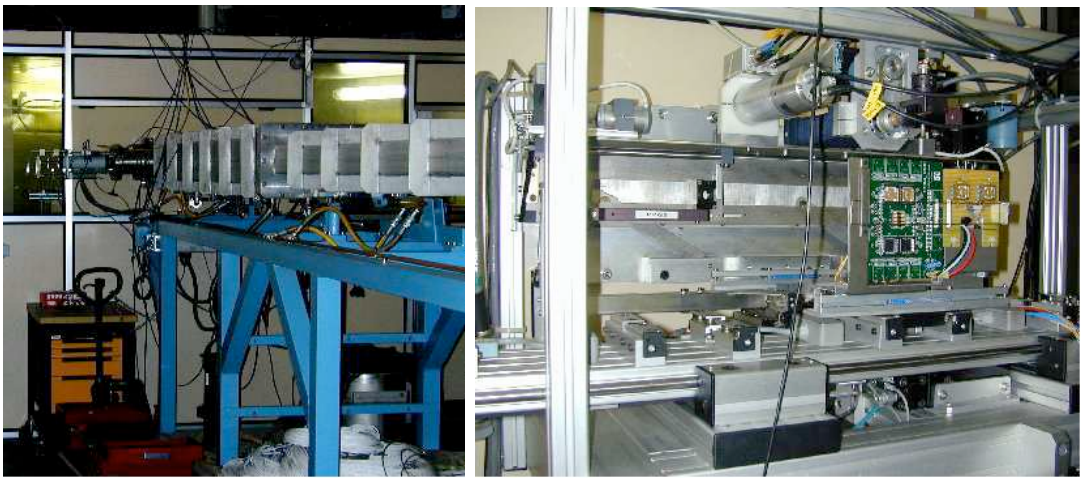

Figure 5.5: The picture on the left shows the vacuum pipe in the experiment hall. The pipe ends in the room in the background and is closed by an inox window. The picture on the right is taken from inside the irradiation room and shows the tested boards facing the inox window. Two boards are visible: the one on the left supports two front-end shapers for the ECAL and the HCAL. The one on the right is the PRS very front-end board from Clermont-Ferrand.

accumulated fluences are given in table 5.4.

The tension and the current of the power supply were monitored continuously in order to detect any SEL. No variation of these parameters has been noticed except for a slow and

Run	Al Thickness (μm)	LET (MeV.mg^{-1}cm^2)	Fluence (cm^{-2}) Period 1	Period 2
1	0.	11.4	2.4×10^7	2.4×10^7
2	250	13	2.4×10^7	3.0×10^7
3	500	15	2.4×10^7	2.3×10^7
4	750	20	2.4×10^7	2.4×10^7

Table 5.4: The run conditions for the two periods with the corresponding fluences and LET.

regular increase from 43mA to 52mA of the current of the supply during the run 4 of the second period. After shutdown of the ion beam, the current slowly returned to a nominal value. This phenomenon doesn't appear to be the consequence of a SEL, but is more certainly due to the accumulated dose which reached 23 and 24 krad for the chips of the period 1 and 2 respectively (see table 5.5).

Run	Accumulated Dose (krad) Period 1	Period 2
1	4.4	4.4
2	9.4	10.7
3	15.2	16.2
4	22.9	23.9

Table 5.5: Accumulated dose (krad) at the end of each run of the two periods.

As for the CPO test, the irradiated components characteristics have been carefully measured on a test-bench at Orsay and fulfill the specifications.

Interpretation of the GANIL experiment

To produce a latchup, we assume first that the ionizing particle should at least deposit an energy of 6MeV.mg^{-1}cm^2 ($\sim$ 1.5MeV.μm^{-1}), value that is slightly above the LET threshold to trigger a SEU in a standard commercial part and that is obtained from the cross-section curves for SEU [6, 54, 51, 75].

Neutrons cannot directly produce a SEL. In fact, the incoming neutron must first brake a nucleus and produce a ionizing fragment whose LET will be large enough to trigger the SEL.

In a neutron-silicon interaction, the fragments produced have an atomic mass ranging from hydrogen up to silicon. Any of the associated isotopes may appear. The program SRIM [96] was used to determine the dE/dx of those ions in silicon. The results are shown on figure 5.6.

Apart from the ion's LET, the probability to produce any of those elements has been extracted from [46] and is shown on figure 5.7 where it was calculated for 1 GeV kinetic energy neutrons interacting with silicon. In the region of the electronics of the calorimeter, most of the neutrons will have a lower energy. Nevertheless, in the following the values of figure 5.7 are used whatever the incident neutron energy. This is a safe and rather pessimistic assumption for the estimation of the tolerance of our electronics.

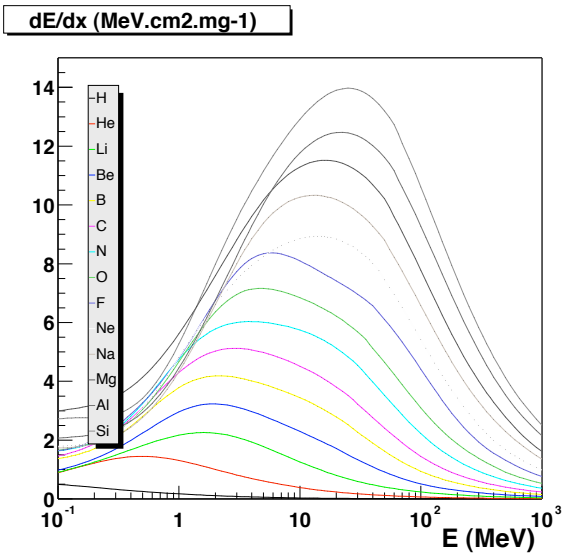

Figure 5.6: LET of several ions which can be produced by neutron-Si collisions with respect to their kinetic energy. Only ions heavier than nitrogen can have a LET greater than 6MeV.mg^{-1}cm^2 (1.5MeV.μm^{-1}). The maximum LET that can be reached with silicon fragments is 15MeV.mg^{-1}cm^2 [46].

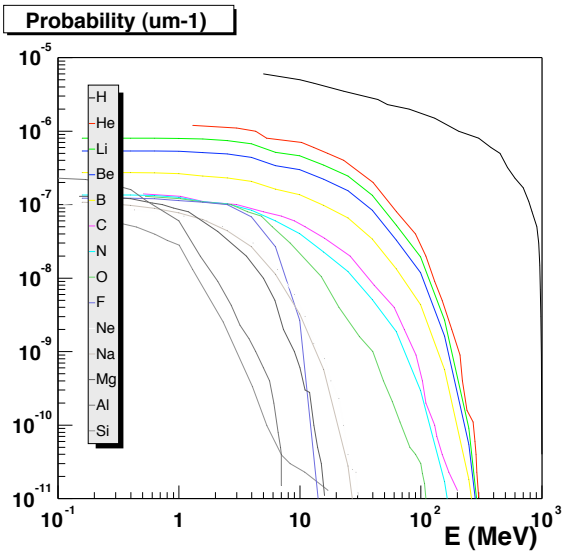

Figure 5.7: Probability (μm^{-1}) to produce a fragment with a energy greater than E in MeV from neutron-Si collisions. Here, the incident neutron energy is 1GeV [46].

From figure 5.6, only fragments heavier than nitrogen can reach a LET large enough to trigger a SEL. Moreover their kinetic energy should be greater than 1 or 2MeV. The probability to produce such an ion from neutron-silicon collisions is below $10^{-7}\mu$m^{-1} (see picture 5.7). Taking into account the SEL sensitive thickness of the component that is evaluated to 10μm

and summing up over the various ion species that can be obtained by collisions, the total probability to get a ion capable of triggering a SEL reaches 2×10^{-6}. If the active thickness is larger than 10μm, then the limiting factor that must enter the total probability evaluation is the range of the ion which is of the order of 10μm or below (see picture 5.8). Thus, the previous estimation is rather conservative. Out of the incident neutrons only a small proportion have the potential to produce a SEL.

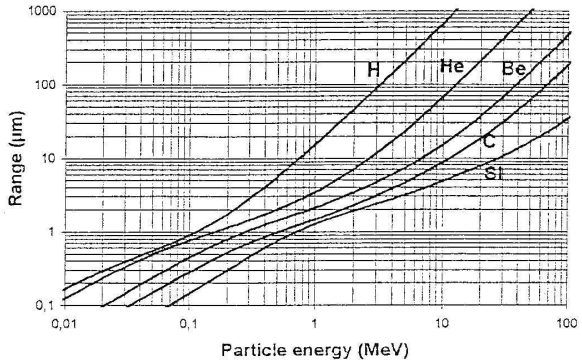

Figure 5.8: Ranges (μm) of several types of ions with respect to their kinetic energy[46].

Let's define the total sensitive area s_{SEL} of the component and the area s_{Kr} affected on average by an incoming krypton ion. If these areas are expressed in proportion of the total active surface of the chip, the probability that an incoming ion doesn't hit a sensitive zone is roughly $1 - s_{SEL} - s_{Kr}$. From the actual number of SEL detected, 95%CL exclusions contours can be drawn in the $[s_{SEL}, s_{Kr}]$ plane (see picture 5.9).

At GANIL, no SEL was detected and two regimes are identified:

- $s_{Kr} > 10^{-8}$: the component has been completely scanned by Krypton and no SEL sensitive zone (at $LET \leq 15\text{MeV.mg}^{-1}\text{cm}^2$) exists.
- $s_{Kr} < 10^{-8}$: only part of the component has been scanned and if the sensitive area is smaller than s_{Limit} it may have escaped scanning. From picture 5.9, $s_{Limit} = 8.9 \times 10^{-9}$ at 95%CL.

Whatever the true regime, the most conservative is the second one and we keep the pessimistic statement that the SEL sensitive zone of the shaper is less than $8.9 \times 10^{-7}\%$ of its active surface.

Hence, the probability to trigger a SEL with a Krypton ion is below 8.9×10^{-9}. The probability to produce an ion with a LET greater than $6\text{MeV.mg}^{-1}\text{cm}^2$ was estimated to 2×10^{-6}. Thus, the probability to trigger a SEL with neutrons reaches a maximum limit of 1.8×10^{-14}. The flux of neutrons above 30MeV[4] is $4.2 \times 10^9 \text{years}^{-1}\text{cm}^{-2}$ and is calculated by integrating

[4]We recall here the assumption that a neutron must have at least 30 MeV to produce a sufficiently ionizing ion. This is motivated by the fact that only a small fraction of the energy of the neutron is given to the heaviest fragment of the collision neutron-Si. The minimal energy to produce a pair of N^{14} ions from a silicon nucleus Si^{28} is $\Delta Q = 29$MeV. So we assume that the probability to produce such a fragment is non zero from 30MeV. But, keep in mind that the value used from 30MeV is the one which is estimated for 1GeV.

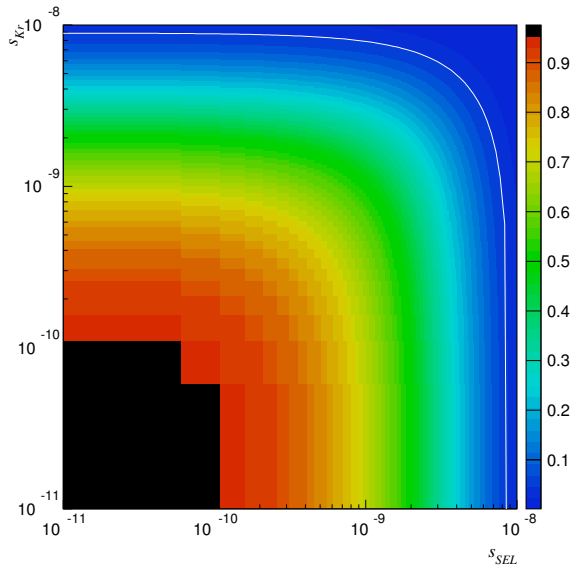

Figure 5.9: The $[s_{SEL}, s_{Kr}]$ plane is shown with the corresponding probability not to have seen any SEL with the front-end shaper. The white line is the 95%CL exclusion contour in the $[s_{SEL}, s_{Kr}]$ plane.

the spectrum of picture 5.3. If we assume that the probability to produce a heavy and energetic enough ion is the same at 1 GeV (value at which it was initially evaluated) and at lower incident neutron energies, the equivalent resistance of the chip is greater than 14 thousand years per chip (see table 5.6).

Component	# SEL	Cumul. time (s)	s_{Limit} 95% CL	s_{min} 95% CL	SEL resistance ($year.chip^{-1}$)
Shaper	0	16000	8.9×10^{-9}	-	>14000
RAM	0	4000	3.9×10^{-8}	-	>3205
Serialiseur 215	2	2521	1.3×10^{-7}	4.0×10^{-8}	>961
Serialiseur 216 (drv)	9	1682	5.0×10^{-7}	1.3×10^{-7}	>250
Serialiseur 483	7	2254	3.1×10^{-7}	5.7×10^{-8}	>403
Serialiseur 484 (drv)	13 (?)	13 (?)	8.1×10^{-5}	2.7×10^{-5}	>1.5 (?)

Table 5.6: Results of SEL resistance obtained from GANIL measurements. s_{Limit} is explained in the text. s_{min} is the minimum size of the sensitive area compared to the total silicon surface of the component. This last parameter can be extracted only when SEL really occurred. The assumed probability to produce a sufficiently ionising ion from silicon-neutron interaction is 2×10^{-6} and the value taken for the neutron flux is $4.2 \times 10^{9} \mathrm{cm}^{-2} \mathrm{year}^{-1}$. The last component tested (last row) suffered almost instantaneous SEL when in the beam, so that the resistance time interval was difficult to estimate. This is emphasized by the question marks added for this row.

This second test is by far more powerful than the CPO test and clearly proves the SEL resistance of the ECAL/HCAL front-end shaper.

Apart from the front-end shaper, many other digital components, that were good candidates to be used on the front-end board of the LHCb calorimeters, have also been tested at GANIL in the same conditions as for the front-end shaper. Some have also been put into the CPO beam of protons.

Table 5.6 shows some of the results obtained at GANIL. The last row gives the example of a component that did not resist to the test and that was not selected to equip our boards.

Apart from irradiations performed at CPO and GANIL, the LAL irradiated many components from 2002 until 2007 at many different facilities : CPO, GANIL, CERN and PSI (Paul Scherrer Institut in Switzerland) [15]. The table 5.13 given at the end of the section list the components that have actually been tested.

5.4 FPGA radiation tolerance

Some intensive irradiation measurements had already been performed by Actel [2] and NASA at Brookhaven National Laboratory [53, 75] on the Actel FPGA AX. This component is an anti-fuse FPGA of the AX family and is adapted to the front-end boards of the calorimeter electronics. They associate a high number of combinatorial and register cells with a large memory. Moreover, the carry-logic implementation increases the efficiency for arithmetic calculations.

We use here some of the results obtained by NASA at BNL [7, 8, 9, 6] to estimate the tolerance of the AX components that are used on our front-end boards in the LHCb cavern environment [81].

5.4.1 Dose, single event latchup and single event dielectric rupture

The Actel AX has been irradiated up to 200 krad (accumulated) at a dose rate of 33 rad/sec with γ particles. No change in the signal propagation delays had been seen. A small increase of the input current had been observed[53]. The dose expected at LHCb in the electronics area is of the order of 200 rad per year, so far below the limits reached by the previous tests.

Apart from the cumulative dose, two effects can permanently destroy the FPGA: the SEL and Dielectric Rupture (SEDR, rupture of an anti-fuse connection due to a local ionisation). The SEL and SEDR immunity has been checked at BNL with several types of ions (I-127, Br-81, Cl-35, F-19, C-12) at LET up to 120 MeV.cm^2.mg^{-1}. No SEL or SEDR was recorded confirming the resistance of the chip in the LHCb environment. We can expect that neutron-silicon interactions produce debris whose maximum LET is 15 MeV.cm^2.mg^{-1} (see figure 5.6), i.e. far below the values tested at BNL.

In order to estimate the resistance of the chip, the same method as the one applied on the front-end shaper is used. A SEL/SEDR sensitive area of the component s is defined together with the area affected by an incoming ion s_{ion}. These areas are expressed in proportion of the total surface of the active area of the component and the probability that an incoming ion doesn't hit a sensitive zone is $1 - s - s_{ion}$. From the number of SEL/SEDR, or from the fact that no SEL/SEDR was recorded, 95% confidence level exclusion contours can be drawn in the $[s, s_{ion}]$ plane.

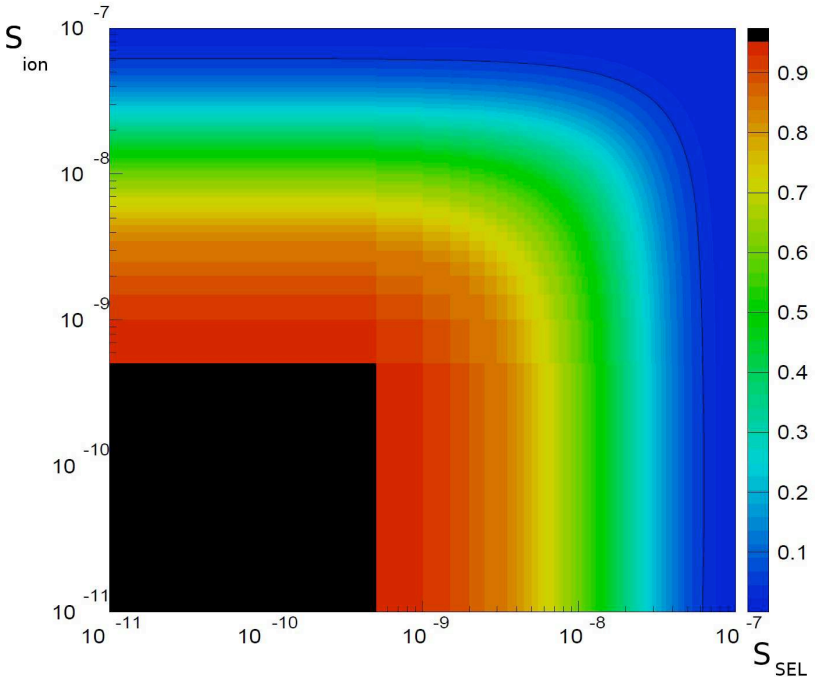

Figure 5.10: Probability not to have any SEL/SEDR with the AX1000 component in five runs of fluence 10^7 ions each. The black curve is the 95% CL contour in the $[s, s_{ion}]$ plane.

Such a contour has been calculated for SEL/SEDR on the AX1000 component. 5 runs of 10^7 ions each had been performed at BNL and are used to obtain the plot of figure 5.10.

Two regimes are identified:

- $s_{ion} > 6.2 \times 10^{-8}$: the component has been fully scanned by the ions of the beam. There exist no sensitive zone at LET tested in the part.

- $s_{ion} < 6.2 \times 10^{-8}$: the component has not been fully scanned, but a limit can be extracted on the size of the sensitive area, $s_{limit} = 6.2 \times 10^{-8}$, which may have escaped the ions of the incoming beam.

As in the previous section, the safest and most pessimistic assumption consists of supposing that the sensitive area is smaller than 6.2x10^{-6} % of the surface of the active area of the component. The probability to produce an ion with a LET greater than 6 MeV.cm^2.mg^{-1} was estimated[5] to 2x10^{-6}. We conclude that the resistance is greater than 1920 years per chip at 95% CL. A neutron flux of 4.2x10^9 year^{-1}.cm^{-2} was assumed as described earlier.

[5]We suppose that below a LET=6 MeV.cm^2.mg^{-1}, it is not possible to trigger a SEL (see section 5.3.2 and [39]).

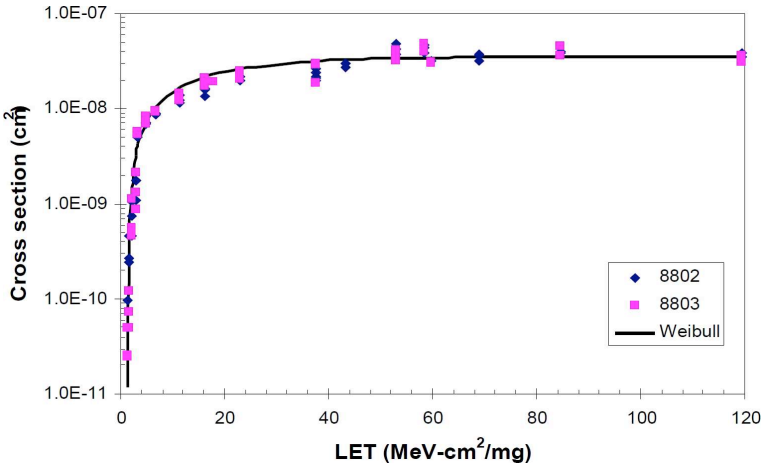

Figure 5.11: AX1000 SRAM SEU cross-section (cm^2) and Weibull curve for two runs.

5.4.2 Single event upset cross-sections

Unlike the SEL or the SEDR, the single event upset or the clock upset are not destructive. The user looses the functionalities of the component until a power reset is done. The SEU is due to an ionising particle that changes a(several) bit value(s) in the RAM or in registers. The clock upset is a glitch on a clock line distributed in the component that desynchronises (part of) the component. The AX components include 4 hardwired clocks and 4 clocks that can be routed by the user.

In this section, some of the measurements performed at BNL are shown [75], [74]. The single event upset cross-sections are given for the SRAM and the registers, respectively. The last curves concern the clock upset cross-sections. All these measurements and the figures of this section are extracted from [53].

SRAM

Figure 5.11 gives the SRAM sensitivity to particles.

R-Cell

"0" and "1" patterns have been used for test purpose, as showed on figure 5.12. "0" pattern seems to be more sensitive than "1" pattern at least for large LET which are far above the LET values reached in our environment. In the following, the measurements obtained with the "0" configuration, which correspond to the largest set of data, will be used only.

The cross-section point of figure 5.12 ("0" pattern) have been used to extract the parameters of the corresponding Weibull functions defined by

$$f(E_{LET}) = \sigma_0 \left(1 - e^{\left(\frac{E_{LET} - E_{L_0}}{W} \right)^s} \right) \tag{5.2}$$

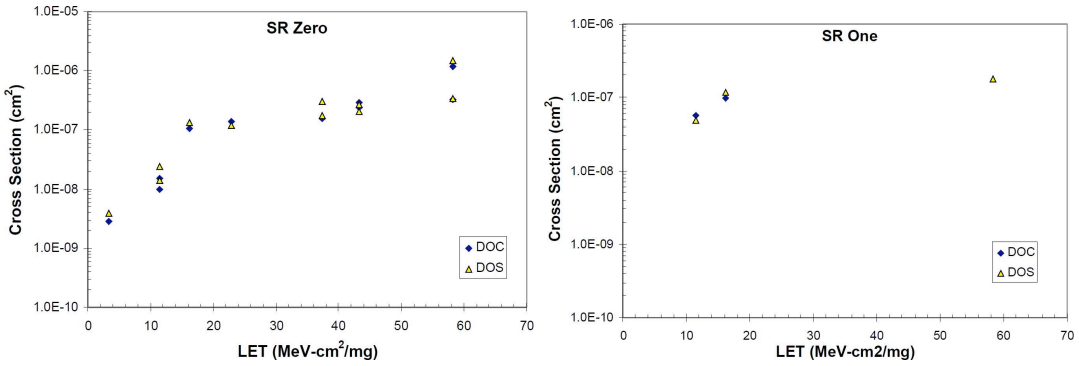

Figure 5.12: AX1000 R-Cell SEU cross-section (cm^2) for "0" (left) and "1" (right) patterns. "DOC" and "DOS" are two different configurations of the 100 bit long registers used for the tests. The results are equivalent in both configurations.

	σ_0	L_0	Width	Shape
S-RAM	$3.5 \times 10^{-8} cm^2$	$1.44 MeV.cm^2/mg$	$15 MeV.cm^2/mg$	1
R-Cell("0" pattern)	$1.0 \times 10^{-6} cm^2$	$3.00 MeV.cm^2/mg$	$30 MeV.cm^2/mg$	2

Table 5.7: Weibull curve (defined by equation 5.2) parameters used in the following for SRAM and R-Cells.

and that is often used to modelize such a processus. The results of the fits are given in table 5.7.

Clock upset

Figure 5.13 gives the clock upset cross-section as measured by BNL.

5.4.3 Single event upset and clock upset rate estimations

Method

In the previous sections, the necessary information has been gathered in order to evaluate the sensitivity of the calorimeter electronics with respect to SEU and clock upset.

The simplest technique to calculate the SEU and clock upset rates consists of integrating the neutron flux multiplied by the upset cross-section expressed in term of the neutron kinetic energy:

$$\int_0^\infty \phi_{\text{neutron}}(E) \times \sigma(E) dE \tag{5.3}$$

In our case, the cross-section is given with respect to the LET of the ions and the previous method cannot be applied directly. The neutron spectrum extracted before allows to derive the flux of ions of type i and of energy E MeV produced by neutron-silicon interaction in a thickness of silicon t,

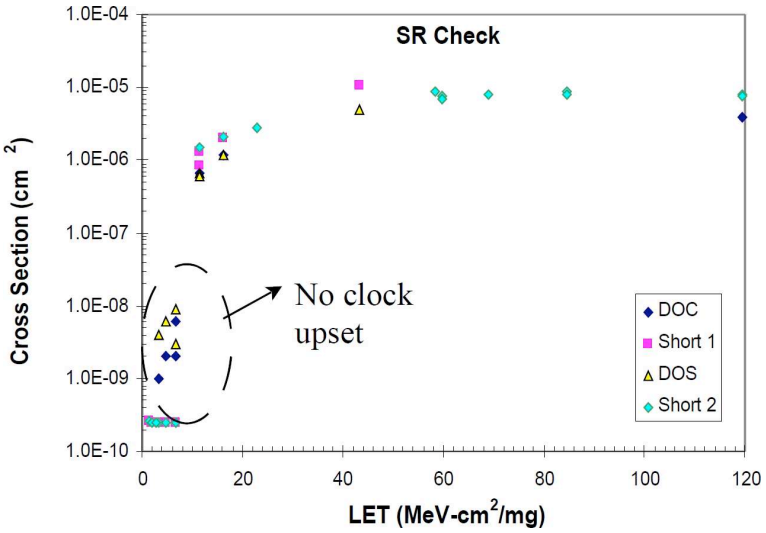

Figure 5.13: AX1000 clock upset cross-section (cm^2) measurements. At low LET, no clock upset have been observed and the values are maximum limits. As for figure 5.12, "DOC" and "DOS" are two types of 100 bit long registers. "Short1" and "Short2" are short, 4 bit long registers. Whatever the registers used, the results are consistent.

$$\phi_i(E) = \int_0^\infty \phi_{\text{neutron}}(E')p_i(E,E')tdE' \tag{5.4}$$

where $p_i(E,E')$ is the probability to produce a fragment of energy E MeV per μm from an incoming neutron of energy E'. As we suppose that this probability is independent of E', the term $p_i(E,E')$ can be extracted from the integral and the total neutron flux enters the $\phi_i(E)$ determination. This is technically done by taking variations of the probability from figure 5.7 in energy bins times the neutron flux and the thickness. We suppose in the following that the active thickness of the components is of the order of t=20 μm. The range of the ions that can potentially trigger a SEU is lower than this value [46]. Hence, the flux $\phi_i(E)$ evaluated this way is rather pessimistic.

The correspondence of the LET of the ions versus their energy can be obtained from figure 5.6.

At this point, the complication comes from the fact that along its way in the silicon of the component, the ion will lose energy. If the initial energy of the fragment i is below the energy for which the LET is max (LET_i^{max}), we assume that the LET keeps its initial value in matter. This is a safe assumption that will lead to pessimistic estimations. On the contrary, if the energy of the debris is high, its LET will first increase while crossing the component. In this case, the LET taken all the way through the thickness t is LET_i^{max}. Once again, this is a safe (and pessimistic) statement. The total SEU rate is calculated by integrating over the full LET range the product of the cross-section (expressed in terms of the LET) by the ion flux (in LET) and summing over the ion species at reach:

$$\sum_{\text{ions}} \int_0^{\infty} \phi_i(E_{LET}) \times \sigma(E_{LET}) dE_{LET} \tag{5.5}$$

or, in our estimation by summing the extracted flux of each ion leading to a certain LET (as described above) times the known cross-section on the full LET range at reach. The contributions over all the ions is summed up and a factor 5 is applied on all the rate estimations to take into account the isotopes of the species.

This method has been used to evaluate SEU for SRAM, R-Cell ("0" pattern) and clock upset.

In the rest of this section, the calculated upset rates per incoming neutron ($s^{-1}.cm^{-2}$) are given. The total upset rate is determined by multiplying this rate by the total incident neutron flux[6].

SRAM

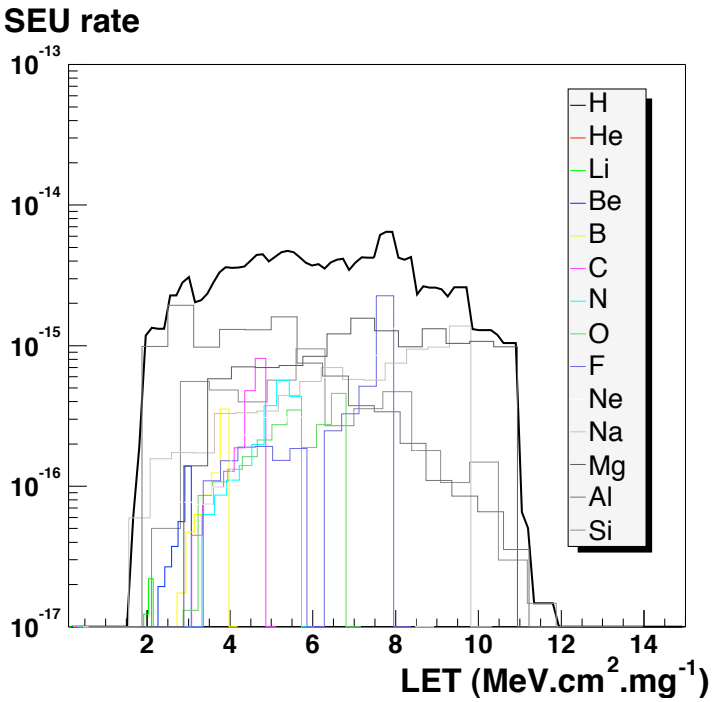

Figure 5.14: Cross-section (see figure 5.11) multiplied by the flux of the possible ions in LET bins. The black curve is the sum over the various ion species.

The cross-section for SRAM can be multiplied by the flux of the reachable ions in LET bins. The final integration of sum (see formula 5.5) leads to a SEU rate per incoming neutron (cm^{-2}) of $6.5 \times 10^{-13} s^{-1}$ per bit (figure 5.14).

[6]This is possible because the probability to produce an ion at a certain energy is supposed to be independent of the energy of the incoming neutron. Moreover, we assumed that the neutron energy had to exceed 30 MeV to be able to produce any type of fragment (see section 5.3.2).

R-Cell

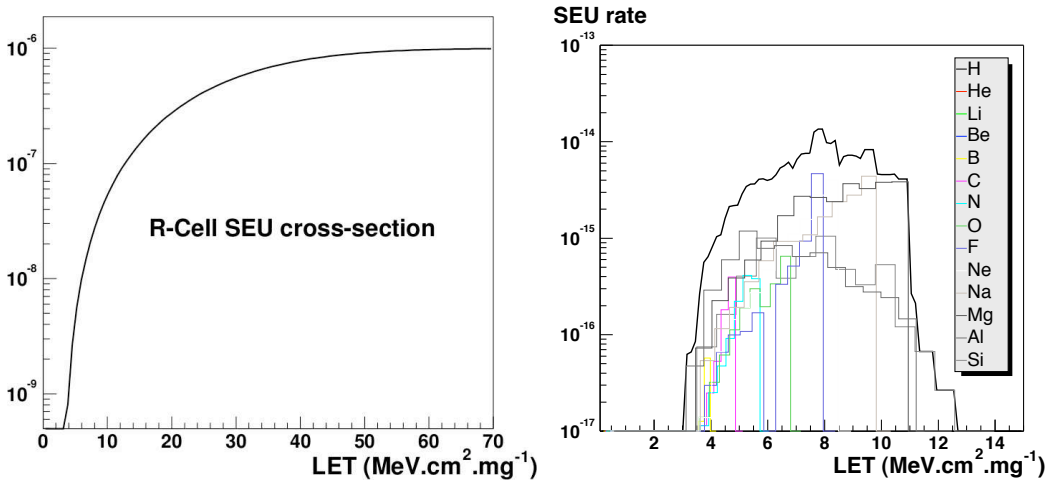

Figure 5.15: On the left, the cross-section (in cm^2) used in the integration of formula 5.5 for R-Cell is given. The right plot is the cross-section multiplied by the flux of the possible ions in LET bins. The black curve is the sum over the various ion species.

The estimation of the SEU cross-section per incoming neutron (cm^{-2}) leads to a R-Cell SEU rate of 5.5×10^{-13}s^{-1} per bit (figure 5.15).

The SEU rate per incoming neutron is slightly higher for SRAM than for register-cell. This could seem paradoxical regarding the asymptotes of the cross-section curves, 3.5x10^{-8} and 10^{-6} cm^2 respectively. The reason is in the shape of the two curves. In the SRAM case, the fragments leading to a low LET can still trigger a SEU when registers need a larger ionisation. Fewer ions species can contribute to SEU in R-Cells and a larger neutron energy is necessary (see picture 5.16).

Clock upset

No clock upset Weibull function was given in reference [53] and we estimated the corresponding parameters from the data. The values of the cross-section have been extracted directly from figure 5.13. Below a LET of 11.4MeV.cm^2.mg^{-1} the points of this figure are limits on the cross-section due to the lack of statistics. We used these limits as measured quantities to perform the fit (the cross-section used are listed in table 5.8).

The parameters obtained from the fit are in table 5.9.

As seen from figure 5.17, the estimation of the clock upset cross-section per incoming neutron (cm^{-2}) is 35.5×10^{-13}s^{-1} per clock .

5.4.4 LHCb front-end FPGA sensitivity and protections foreseen

No protection is planned for the SRAM. The high frequency data related to the measured signals are stored in RAM and a SEU would affect a very limited set of information.

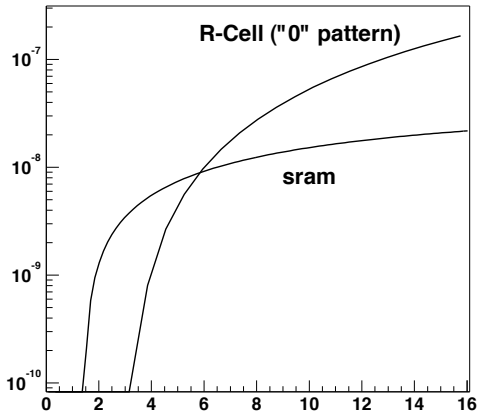

Figure 5.16: Comparison of the SEU cross-section Weibull curves for RAM and R-Cell.

LET (MeV.cm^2.mg$^-$1)	Cross-section (cm^2)
5	10^{-9}
6	5×10^{-8}
11	10^{-6}
20	3×10^{-6}
40	10^{-5}
100	10^{-5}

Table 5.8: Clock upset cross-section (cm^2) values extracted from figure 5.13[53] and used for the Weibull curve parameter estimation.

	σ_0	L^0	Width	Shape
Clock upset	10^{-5}cm^2	5.0MeV.cm^2/mg	20MeV.cm^2/mg	2

Table 5.9: Weibull curve parameters obtained for the AX1000 clock upset cross-section (cm^2).

The registers will keep critical data (calibration values, counters, ...) that will be reloaded typically once a day. Two protections were foreseen for registers:

- Triple Voting Registers (TVR): the information is stored three times and a vote is done on the three copies. The majority is kept.
- Horizontal and Vertical Parity (HVP): the values are stored in a table and horizontal and vertical parities are calculated. When the values are needed the parities are checked. An error can be corrected. When two errors occur in the table, the problem is known.

The TVR mitigation is a stronger protection, but consumes more registers (3N registers versus $\left(\sqrt{N}+1\right)\left(\sqrt{N}+1\right)$ to protect N bits). TVR was nevertheless chosen to protect all

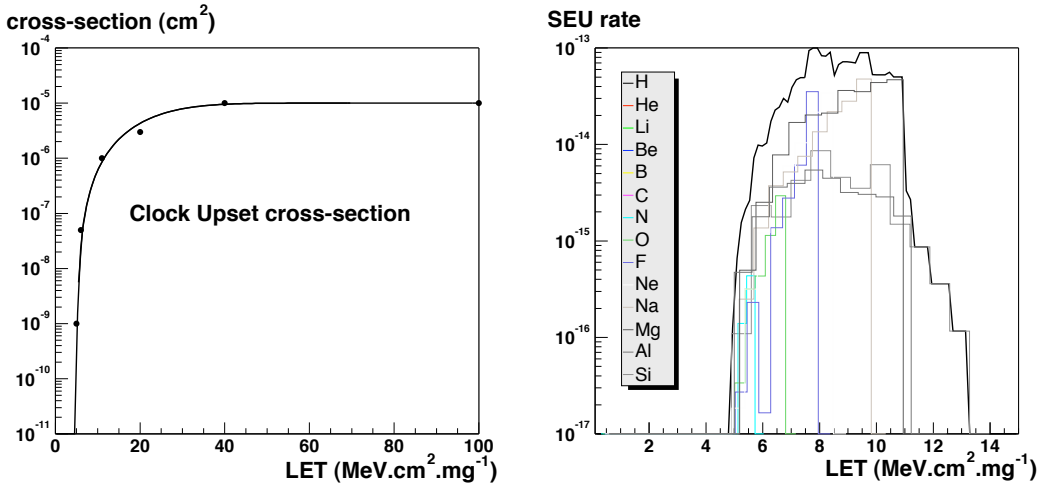

Figure 5.17: On the left, the cross-section used in the integration of formula 5.5 for clock upset is given. The right plot is the cross-section multiplied by the flux of the possible ions in LET bins. The black curve is the sum over the various ion species. The integration of this curve leads to a clock upset rate per incoming neutron (cm^{-2}) of $35.5 \times 10^{-13} s^{-1}$ per clock.

	Registers	
	TVR (N=1 bit)	HVP (N=4x48=192 bits)
SEU rate	5.5×10^{-13}	
Flux	$420 s^{-1}.cm^{-2}$	
Reload	1 day	
LHCb SEU rate (/Reload/N bits)	1.2×10^{-9}	7.3×10^{-6}

Table 5.10: The SEU rate for registers is given for two mitigation techniques: TVR and HVP. The TVR rate is evaluated per bit. The HVP rate is given for a 4x48=192 bit table.

our configuration registers and it is the mitigation technique evaluated below.

The LHCb calorimeter (ECAL/HCAL) sensitivity can be evaluated after a recall of the requirements of the systems. The following numbers are given for a AX250 component based electronics of 2048 FPGA (256 boards with 8 FPGA, 4 channels per component, an AX1000 being roughly equivalent in resources to 4 AX250 parts). The AX250 and AX1000 are based on the same technology. We consider of course that there is no difference between having our registers gathered in a single chip or in 4 ones.

There are two types of registers protected by triple voting:

- Constants refreshed on the every day basis:
  - clock front inversion (1 bit / channel)
  - subtraction control switch (1 bit / FPGA)
  - second subtraction scheme value (2 bits / FPGA)

SRAM	
SEU rate	6.5×10^{-13}
Flux	$420 s^{-1} cm^{-2}$
Reload	$16 \mu s$
LHCb SEU rate (/Reload/bit)	4.4×10^{-15}

Table 5.11: SRAM SEU rate for a typical reload of the L0 derandomiser events of 16 μs.

  - No subtraction selector (1 bit / FPGA)
  - L0-latency address (8 bits / FPGA)

  The error frequency for those 16×2048 bits is 3.9x10^{-5} per day (see table 5.10), i.e. once every 214 years[7].

- Values updated at 40MHz:

  - counter for the write address in the RAM (8 bits / FPGA)
  - L0-Yes position in derandomiser (4 bits / FPGA)

  We still assume 2048 AX250 FPGA. The numbers of table 5.11 are evaluated for high reload frequency. The error rate obtained is 7.3x10^{-14} errors per year. Of course, the reason for such a small number is the constraint that two errors[8] have to occur in coincidence in a very short time.

Nevertheless, notice that these evaluations are probably underestimated. We could imagine that a large charge deposit due to a significant LET may flip altogether geographically close registers. Thus, two of the 3 registers used to protect a value by TVR could potentially flip in coincidence and lead to a fault of the system more often than the simple uncorrelated register flipping estimation done here.

The calorimeter (both ECAL/HCAL and PRS/SPD) will produce 2.9×10^5 bits per event. The error rate in the $L0$ derandomizer will be 7.9×10^{-5} per event at the $HLT1$ input, i.e. one event out of 1.6×10^7 stored on disk will have an affected bit. This is not a limiting factor. Let's recall that a bit-flip on a configuration registers may systematically affect all the data until reload by the slow control.

The estimated frequency of clock upset is 7.5 per year[9] (48.5 consecutive days) for the HCAL/ECAL. This estimation is done with safety factors. Simply taking the correct flux determined with the proper Hubner factor and data taking period duration reduce it to 2.8 per year.

[7]Here, a year is 10^7 seconds and equivalently 120 days.

[8]The TVR technique corrects a single bit but cannot cope with two

[9]This is evaluated from the clock upset rate per clock given in table 5.12 and taking 512 clock paths of AX1000 type. A year is still assumed to be 10^7s.

Clock	
Clock Upset rate	3.5×10^{-12}
Flux	$420 s^{-1} cm^{-2}$
Clock upset / clock	1.47×10^{-9}

Table 5.12: Clock upset rate per incoming particle and for the LHCb cavern expected particle flux.

5.5 Summary table and conclusion

A large number of components have been tested by the LAL group in many different conditions. Table 5.13 sums up the irradiations performed and the doses received.

Part	Irradiation conditions	Dose (krad)	Observations
Calo FE Shaper	CPO (Orsay) Proton 200 MeV, $10^8 s^{-1}.cm^{-2}$	22.6	No effect
		10.7	No effect
		12.3	No effect
		11.7	No effect
	GANIL (Caen) Krypton 58MeV/A	22.9	No effect
		23.9	Small current increase (from 43mA to 52mA) observed at the end of the run (22krad). After shutdown, current returned to nominal value
Transmitter DS90CR215	GANIL (Caen) Krypton 58MeV/A	6.5	No effect
Receiver DS90CR216		6.5	No effect
Transmitter DS90CR483		6.5	No effect
Receiver DS90CR484		6.5	No effect
FPGA Actel A54SX32A		6.5	No effect
FPGA Xilinx XCV50		6.5	No effect
Test RAM IDT71V016SA		6.5	No effect
Delay Chip	GANIL (Caen) Krypton 78 73MeV/A	28.8	2 parts irradiated simultaneously. No effect
		24.2	2 parts irradiated simultaneously. No effect
DS92LV010A		28.8	2 parts irradiated simultaneously. No effect
		24.2	2 parts irradiated simultaneously. No effect
SN65MLVD200		28.8	2 parts irradiated simultaneously. No effect
		24.2	2 parts irradiated simultaneously. No effect
Transistor NPN NE856		24.2+28.8 =53.0	4 parts irradiated simultaneously. No effect
	Russia (Moscow)	125	Small current increase at high dose level (?)
QuadBuffer 74F125	GANIL (Caen) Krypton 78 : 73MeV/A	24.2	2 parts irradiated simultaneously. No effect
PROM AT17LV65		28.8	2 parts irradiated simultaneously. No effect
Current Amplifier AD 8011	GANIL (Caen) Krypton 86(43.5MeV/A)	91.0	2 parts irradiated simultaneously. No effect
Power Switch MAX 869L		91.0	2 parts irradiated simultaneously. No effect
Oscillator 40MHz JAUCH 0-40.0-VX3MH	PSI (Zurich) Proton 60 MeV $10^9 s^{-1} cm^{-2}$	147	Component failure at 16krad. Consumption drops to very small value. No recovery after beam shutdown.
PROM PCF 8582		147	Continuous current increase at 14krad Slow recovery observed if the beam is switched off.
SN65LVDS32		147	Continuous current increase at 30krad. Slow recovery observed if the beam is switched off.
DS92LV090		147	No effect.
SN65LVDS104		100	2 parts irradiated simultaneously. No effect.
		400	2 parts irradiated simultaneously. No effect.
DS90LVDS001		100	2 parts irradiated simultaneously. No effect.
		400	2 parts irradiated simultaneously. No effect.
ACTEL APA 150	CPO Protons 187 MeV	40	Bad functioning appeared after 30 krad. Program reloading seems to break the components after 20krad (One week in an oven at $\sim 100°C$ leads to recovery).
ACTEL APA 300		40	Bad functioning appeared after 30 krad. Program reloading seems to break the components after 20krad (One week in an oven at $\sim 100°C$ leads to recovery).

Table 5.13: List of components which have been tested by the LAL group. The components are grouped according to the various irradiation periods performed which are emphasized by colours. The observations only concern the dose effects. Some of the listed components suffered from SEL and could not be used on our electronics.

The accumulated doses reached during the irradiations easily overtook what we expected

in the cavern in the vicinity of the electronics of the calorimeter [10]. Proton beams (CPO or PSI) allowed us to go even beyond 100krad. This has been punctually necessary in order to test some components that were supposed to be used on the SPECS electronics [30, 31] that equip other and more exposed systems than the calorimeter (up to several tens of krad over the lifetime of the experiment). Apart from a few current drifts, most of the parts (commercial or not) had a good behaviour regarding the dose.

The APA FPGA from Actel equips both the front-end electronics of the calorimeter and the SPECS mezzanines. This is a flash type component. This means that the program may be reloaded in the part as many times as needed [11] and that it cannot be affected by SEU. Moreover, the manufacturer already performed measurements of the resistance of the component to SEL and showed that it can survive LET greater than $100\text{MeV.mg}^{-1}\text{cm}^2$. At LHCb, the environment is such that the maximum LET does not overtake $15\text{MeV.mg}^{-1}\text{cm}^2$. Nevertheless, we had no reliable information on the dose resistance of this chip. The irradiation mentioned in table 5.13 (bottom lines) was supposed to measure its resistance in term of dose. It was also planned to test regularly the re-programming of the component. The FPGA started to have a bad behaviour above $20 - 25$krad as any attempt to reload the program apparently broke the chips tested. Moreover, for those that were not re-programmed, malfunctions appeared after $30 - 35$krad. After the irradiation, we have been advised to put the component in an oven at 100°C for one week. This was supposed to help and accelerate the diffusion of any default in the part. This was successful, as all the faulty components could be re-programmed and became again functional. We may imagine that the limits measured during our irradiations are severe as a slow irradiation lasting several years would lead to some annealing. This was not the case during our tests. Moreover, the SPECS is a mezzanine board and can easily be replaced when a significant accumulated dose is reached.

As was already emphasized in this chapter, the single event latchup (SEL) caused more problems and several components (commercial ones) that were good candidates have been rejected from the list of used parts. This is the case of the transmitter and receiver DS90CR-483 / DS90CR484, the former triggering a latchup almost immediately after the irradiation beam was on. This was also the case of the 40MHz JAUCH Oscillator that was foreseen to equip the CROC. Finally, it was decided not to put any 40MHz oscillator on the CROC and to systematically use the TTCrq mezzanine board. GANIL irradiation, as opposed to proton beams, permitted to reach interesting limits on SEL before the accumulated dose was critical for the components.

The components have been chosen for their low sensitivity to the type and level of radiations expected in the vicinity of the calorimeter electronics. The single event effect rates extracted in this chapter are low. Moreover, those estimations have integrated safety factors or pessimistic hypothesis. Finally, let's mention that the LHCb experiment equipped the cavern both with passive and active dosimeter in order to monitor the level of radiations, their type and the accumulated dose. Some of the dosimeter are located on the platform supporting the crates of the calorimeter.

[10] The dose expected on the gantry above the calorimeter, where the crates are localized is 200rad per year.

[11] Let's recall that, the other type of FPGA from Actel, also used on the calorimeter electronics are called AX and are anti-fuse type components. They can be loaded only once.

Part II

Photon identification and calorimeter calibration

Chapter 6

Photon identification

Contents

6.1 Introduction 101
6.2 Definitions 101
6.3 Acceptance 103
6.4 Reconstructed tracks removal 103
6.5 The method 104
6.6 Performances 111

6.1 Introduction

Detector calibration and physics analysis require the selection of photons with a high efficiency and the smallest possible contamination. This is the purpose of the algorithm that is presented in this section and that associates to the calorimeter clusters an estimator based on probability density functions for several variables of interest. The clusters are selected and considered as photons depending on the cut applied by the user on this estimator [82].

6.2 Definitions

The particles that reach the calorimeter may be of different types. The background is made of electrons, hadrons, etc.... Another type of particle that we consider here as background is due to photons not incoming from the interaction point [70]. This specific case may be studied independently as will be explained later on.

To summarize, the categories are defined as follows with the correspondences in the Monte Carlo truth information:

- Signal: a calorimeter cluster

1. associated[1] to a Monte Carlo true photon,
2. whose energy is correctly measured in the interval,

$$\Delta E = \frac{|E^{\gamma}_{Rec} - E^{\gamma}_{MC}|}{E^{\gamma}_{Rec}} \leqslant 25\% \tag{6.1}$$

3. whose associated Monte Carlo true photon originates from the interaction region defined by the cylinder

$$\begin{cases} \Delta r \leqslant 10mm \\ \Delta z \leqslant 150mm \end{cases} \tag{6.2}$$

- Background: the other calorimeter clusters.

The justification of the second criterion in the "signal" definition is used to reject the merged π^0 from the list of the possible signals. Indeed, at LHCb, a fraction of the neutral pions produce two photons which are not separated at the level of the calorimeter; this is more frequent above a transverse energy of the pion of the order of 2.5GeV. This case is treated specifically, as described in [57]. Moreover, pile-up may affect the energy measurement; this is taken into account here as a badly measured photon would be considered as a background. This makes sense as the four-momentum of the identified particle is essential in any physics analysis.

The third criterion, will put in the background category the bremsstrahlung photons as their identification can be more easily done starting from the track being at their origin. The bremsstrahlung photon is supposed to start tangentially to the electron and most probably at the z position of a detector equipment where it occurred.

Two cases appear then:

- the bremsstrahlung took place before the magnet,
- it occurred after (in z) the magnet.

Let's recall that since the LHCb detector optimisation (performed in 2004), there is no matter in the volume of the magnet.

In the first situation, the track followed a straight line until the radiation took place and the extrapolation of the track trajectory as measured from its first hits (VELO and tracker turicensis) leads to the bremsstrahlung photon cluster [90].

The second situation is simpler. If the bremsstrahlung occurred after the deviation of the charged track by the magnet, the electron and the bremsstrahlung photon coincide at the level of the calorimeter and the electron reconstruction does not require any specific treatment.

An intermediate situation appears when the bremsstrahlung emission is done sufficiently close to the magnet so that its effect is not fully negligible on the track. A refinement can be imagined to recover those cases by giving for example a certain tolerance in the distance between the track extrapolation and the closest calorimeter cluster.

[1] The link is derived from the LHCb software associators that evaluate the energy contributions of the MC-true particles to the cluster energy reconstructed. A photon is associated to the cluster if it has the largest contribution.

6.3 Acceptance

The geometrical detector acceptance is defined in table 6.1. The photons are supposed to be identifiable if the position of their impact on the calorimeter surface is on the equipped cells, the border cells of the detector being excluded. This is based on the typical photon shower size that extends from 3×3 to 2×2 cells in the inner and the outer regions. The energy loss for a photon absorbed in the last cell of the border will probably not be correctly measured. From the beginning we exclude this case.

z position	Inner Acceptance (mm)		Outer Acceptance (mm)	
12.696m (Shower maximum)	|x|>363.6	|y|>363.6	|x|<3757.2	|y|<3030.0
12.490m (ECAL front-face)	|x|>360.1	|y|>360.1	|x|<3721.3	|y|<3001.1

Table 6.1: Geometrical acceptance for MCTruth and reconstructed photons.

In the previous part, it was pointed out that the calorimeter measurement is done at the electronics level in P_t. This is the most relevant information to characterize the photons incoming from the interaction point. At very low P_t, several problems appear. The "background" (made by any type of particle among which the photons that are not produced in "physics" processes of interest) increases drastically. The electronics noise, at the level of 20MeV/c maximum, is not really a problem compared to the particle background expected.

The 2D zero suppression performed at the reconstruction level removes all the isolated cells whose transverse momentum is lower than 50MeV/c. Moreover, the cluster reconstruction algorithm requires that the central cell of the cluster, called "seed" in the following, has a transverse momentum also larger than this threshold [56].

The physics analysis showed that trying to use very low P_t leads to a large contamination and a bad energy reconstruction. The lower P_t threshold was the subject of an optimisation based on the study performed for the particle identification algorithm presented here and for the reconstruction of the B decay channel $B \to \pi^+\pi^-\pi^0$ [55], where the photons produced by the neutral pion have a low transverse energy. 200MeV/c is now the adopted threshold used for the analysis in LHCb summing the energy over the 9 cells of the 3×3 cluster and will be used as the minimal P_t of the photons called "reconstructible" according to the Monte Carlo and used in the future efficiency and purity calculations.

The clustering algorithm used here is described in [56] and consists in identifying local maxima to which are associated the neighbours. A cluster is built from 9 cells centered on the local maximum and having a square 3×3 shape. The complications linked to the borders of the calorimeter regions will not be described here. The details may be found in [56].

6.4 Reconstructed tracks removal

The selection of the photon candidates relies first on the proper elimination of the reconstructed tracks as many of them will deposit energy in the calorimeter and produce a cluster. Those clusters should be removed from the list of potential photon candidates.

The method used here to achieve this first selection consists in extrapolating all the reconstructed tracks to the calorimeter and evaluating their bi-dimensional position, $\vec{p}_{tr}$, at the "shower-maximum" (roughly at $6X^0$) z position. Likewise, the cluster position, $\vec{p}_{cl}$, is evaluated taking into account the shower shape corrections [56].

The following χ^2_{2D}:

$$\chi^2_{2D}(\vec{p}) = (\vec{p}_{tr} - \vec{p})^T \mathcal{C}_{tr}^{-1} (\vec{p}_{tr} - \vec{p}) + (\vec{p}_{cl} - \vec{p})^T \mathcal{S}_{cl}^{-1} (\vec{p}_{cl} - \vec{p}) \tag{6.3}$$

is then minimized according to all the tracks and the quantity $\vec{p}$, $\mathcal{C}_{tr}$ being the covariance matrix of the extrapolation $\vec{p}_{tr}$ of each track and $\mathcal{S}_{cl}$ the second-order cluster momenta. The obtained value of χ^2_{min} gives the proximity of the closest track extrapolation and the considered cluster. The figure 6.4 shows the distribution of χ^2_{min} for all the clusters, the clusters from charged particles and the clusters from electrons.

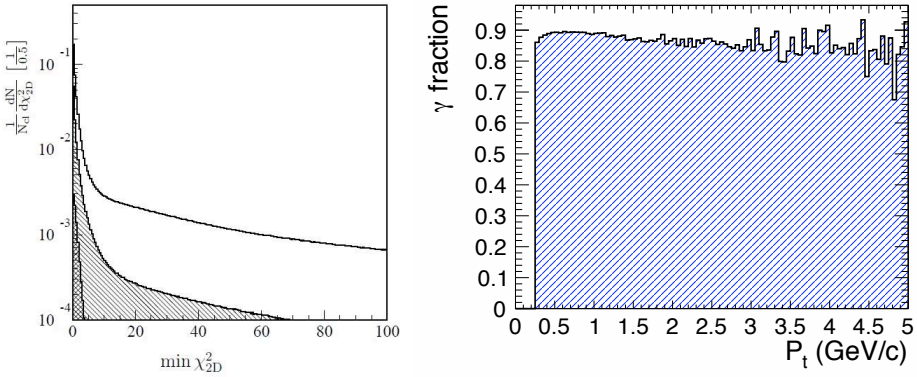

Figure 6.1: Left: χ^2_{min} distributions for all the reconstructed clusters (open histogram), clusters from charged particles (hatched histogram) and clusters from electrons (cross-hatched histogram). Right: The fraction of photons passing the cut at 4 on χ^2_{min} depending on the P_t of the particle.

A cut at 4 on χ^2_{min} permits to remove the major fraction of the charged track background. The effect on the background and signal is showed on figure 6.1 either with respect to the χ^2_{min} parameter or to the photon P_t. The "reconstructible" photons (the term was already introduced above) should also pass this criterion. The overall χ^2_{min} cut efficiency is of 88.2%. All the future efficiencies and contaminations extracted in the following sections are extracted from the sample selected at this stage of the analysis.

6.5 The method

The technique used to identify the photon signal consists in extracting a photon hypothesis likelihood from the signal and background probability density functions (pdf) of several variables.

Three variables are used, sorted out from the most powerful to the least one :

- The PRS energy deposited in the cells facing the 9 ECAL cluster cells. Electromagnetic objects (photons and electrons) will have a large energy deposition in the PRS layer (see figure 6.3). Hadrons should not deposit a sizable energy.

- The χ^2_{min} parameter already introduced still contains a valuable information after the applied cut as the electrons are not removed at all by taking into account the PRS energy deposition (see figure 6.4).

- The ratio of the energy in the central cell (seed) to the energy of the cluster evaluated from the sum of the deposition measured in the 9 cells of the cluster. This quantity is sensitive to the transverse photon shower shape and is also different for electrons and photons (see figure 6.5). This ratio is in average larger for photon than for the background particles. Moreover, photons not incoming from the interaction region will have a distorted shower shape. This will be taken into account in the pdf used.

The variables listed above characterize the photon signal and the background. But their shape evolves significantly with the energy of the incoming particle and of the cluster. Hence, the shape that is used to build an estimator has to be energy dependent[2]. This dependency is highly non-linear. Indeed, the variation of the shapes is rapid in the low energy regime and is slow in the large energy region. This leads to the construction of probability density functions (pdf) per variable and per energy bins, the width of the bins being narrow to wide from low to large energies. The normalisation of the functions is done per energy bin both in the signal and the background cases.

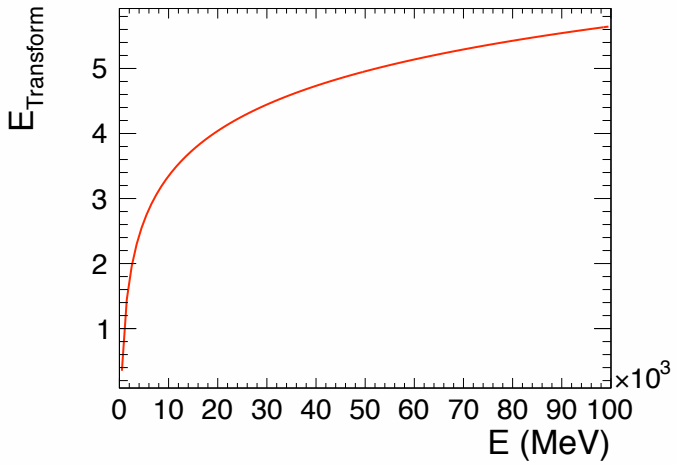

Figure 6.2: The transformation applied to the energy and used to take into account the evolution of the shape of the variables used for the photon estimator.

[2]The probability density functions of the variables mentioned have also been built with respect to the transverse energy. The final performances of this algorithm was equivalent or slightly degraded compared to what is presented in this document.

To define the variable bins, regular intervals are used on a transformed value of the energy. The transformation used is

$$E_{\text{Transformed}} = \ln(1.4 \times E(\text{MeV})) - 6.2) \tag{6.4}$$

and is showed on curve 6.2.

The number of pdf is already large, as 3 variables are used in the signal and background cases, and the description of the variables is done in 10 (transformed) energy bins in the two cases.

Moreover, two types of photons are part of the signal. The photons that reach the calorimeter without being converted and the photons that interact with the detector matter and produce two electrons that propagate to the calorimeter surface. The most powerful criterion to separate the two categories is the energy deposited in the cell of the SPD that faces the ECAL seed of the photon candidate cluster. Any charged particle should deposit a mip in the SPD scintillator layer. The large majority of photons that did not yet convert will not deposit any energy. The SPD is a single bit value detector that compares the signal in its cells with a threshold. This threshold is tuned slightly below the mip, but largely above the noise. The efficiencies and contaminations of the SPD are indicated in table 6.2.

MCTruth γ	No SPD hit	SPD hit
$\gamma \rightarrow e^+e^-$	8.2%↓ - 23.7%→	72.9%↓ - 76.3%→
$\gamma \nrightarrow e^+e^-$	91.8%↓ - 90.3%→	27.1%↓ - 9.7%→

Table 6.2: Contributions from converted or not-converted MCTruth photons and SPD hit or no SPD hit type clusters in the signal sample. The percentage indicated must be read according to the direction of the arrow (with respect to the sub-total in the corresponding row or column). For example a photon reconstructed without hit in the SPD has 8.2% chance of being converted according to the Monte Carlo truth information (first column). But a Monte Carlo truth converted photon would be seen in 23.7% of the cases without hit in the SPD (first row).

Nevertheless, it appears in table 6.2 that sometimes, a photon does have a hit in the SPD cell in front of the ECAL seed although it did not convert. Two main reasons are at the origin of this signal,

- a charged particle triggers a coincidence with the photon and has an impact on the SPD cell,
- back-scattered particles originating from the PRS or the ECAL corrupt the SPD information.

The total amount of not converted photons seen with a hit in the SPD reach 10%. On the contrary, a fraction (less than 25%) of the converted photons do not deposit energy in the SPD cell facing the ECAL seed the impact being most probably at the edge of the cell. In general this is due to the fact that, although the SPD/PRS/ECAL system is projective, the correct SPD cell to look for the hit is not the one facing the seed. It was tried to extend the region to

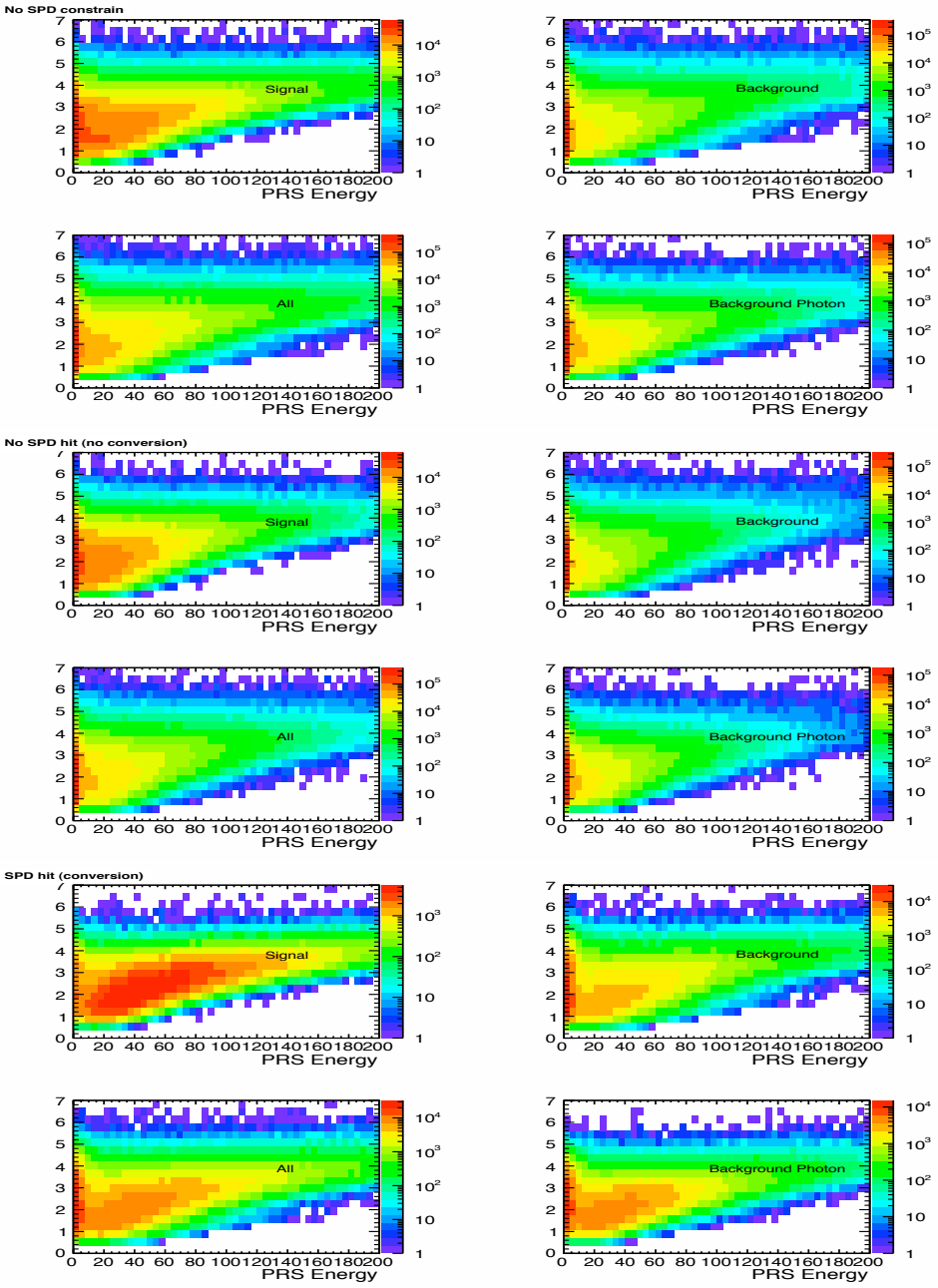

Figure 6.3: The PRS energy in the cells facing the ECAL cells of the photon candidate cluster. The middle four plots are built from the sample of clusters having no hit in the SPD cells facing the ECAL seed, the four bottom plots require that a hit was seen in this SPD cell and the four top ones integrate no constraint on the SPD. Each group of four shows the signal, background distributions, the overall signal and background and finally the background made from photons. The x-axis parameter is the PRS energy, the y-axis one being the transformed energy as described in the text.

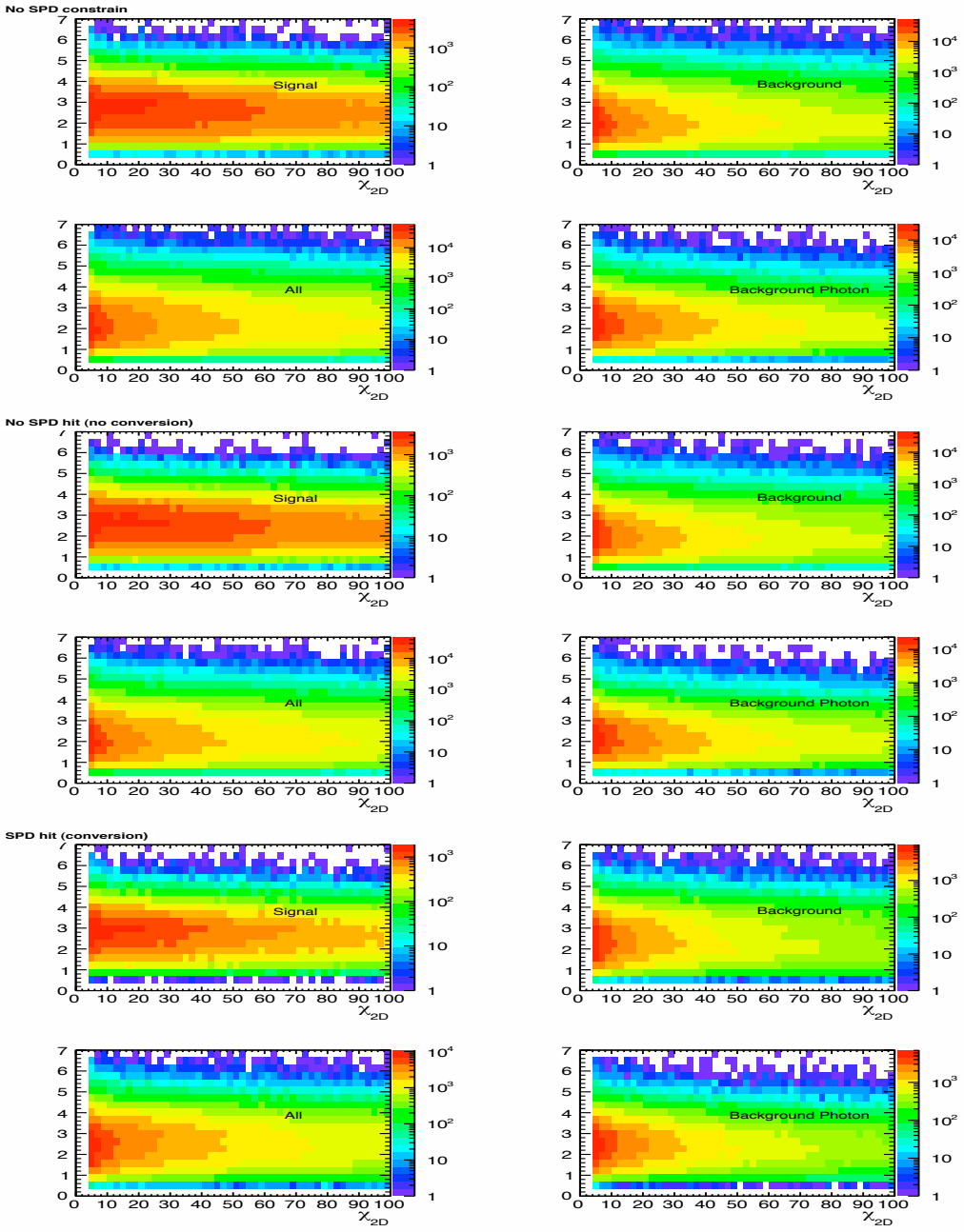

Figure 6.4: The χ^2_{min} evaluated for the photon candidate cluster. The middle four plots are built from the sample of clusters having no hit in the SPD cells facing the ECAL seed, the four bottom plots require that a hit was seen in this SPD cell and the four top ones integrate no constraint on the SPD. Each group of four shows the signal, background distributions, the overall signal and background and finally the background made from photons. The x-axis parameter is χ^2_{min}, the y-axis one being the transformed energy as described in the text.

look for a hit in the SPD: the fraction of converted photons having no hit is reduced drastically, but it leads to a larger contamination of not converted photons having a hit. This path was

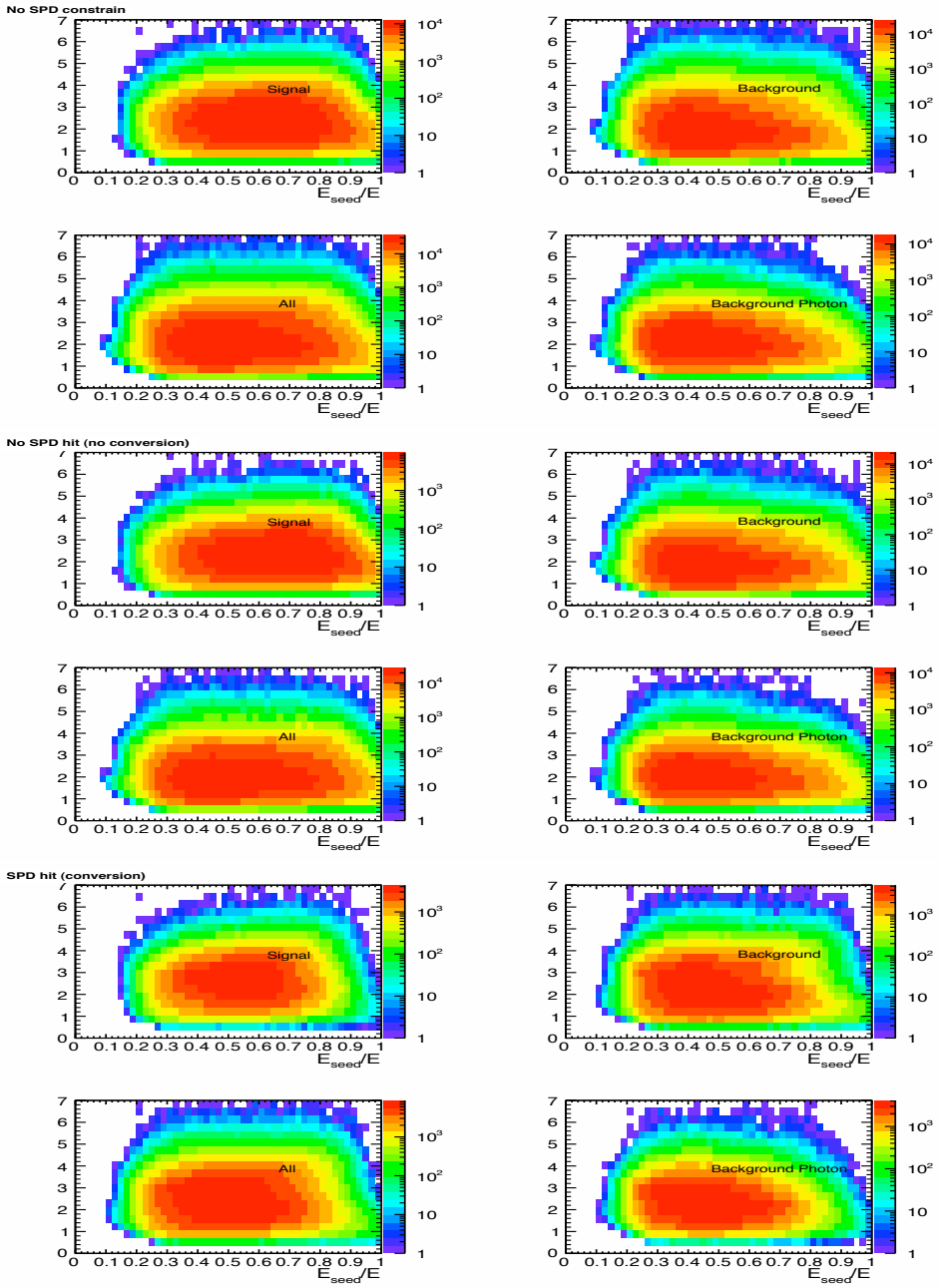

Figure 6.5: The ratio $E_{\text{seed}}/E_{\text{Cluster}}$ evaluated for the photon candidate cluster. The middle four plots are built from the sample of clusters having no hit in the SPD cells facing the ECAL seed, the four bottom plots require that a hit was seen in this SPD cell and the four top ones integrate no constraint on the SPD. Each group of four shows the signal, background distributions, the overall signal and background and finally the background made from photons. The x-axis parameter is the ratio $E_{\text{seed}}/E_{\text{Cluster}}$, the y-axis one being the transformed energy as described in the text.

not followed further and the two converted and not converted categories below correspond to the SPD deposit in the cell in front of the seed.

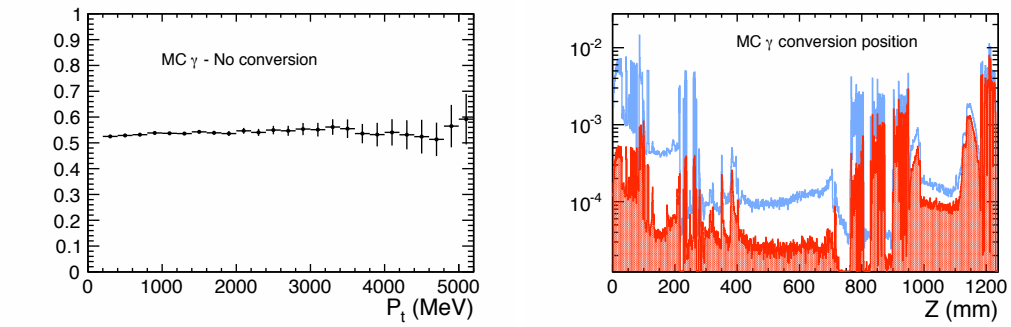

Figure 6.6: Left: Proportion of MCTruth photons that did not convert before the calorimeter among the photons originating from the interaction point versus their transverse momentum. Right: The blue histogram shows the repartition of the photon conversions along the z-axis. A bin corresponds to 1cm and the main structures of the detector may be clearly identified. The red histogram shows, among the previous converted photons, those that can be associated to a single cluster in the calorimeter and whose energy equals the MCTruth photon energy ±25%.

From figure 6.6 (left), it appears that 45% of the photons convert in the detector. Among those, the early conversions (before the magnet) will be identified as background as the two electrons will produce two separated impacts at the level of the calorimeter surface. In general, none of the two clusters will have an energy in the ±25% allowed range to define a signal photon. On the contrary, the late conversions (after the magnet, where the magnetic field has no effect anymore on the charged particles) may still produce a single cluster on the calorimeter surface. The measured deposit may coincide with the original photon energy in the ±25% interval. The shower shape characteristics on those late conversion will be different than in the not converted case and this is taken into account by having two sets of probability functions for the converted and not-converted cases, whatever the variables.

Another complication that was not mentioned yet comes from the granularity of the SPD / PRS and ECAL that varies depending on the rapidity. The shower shape, the ratio E_{seed}/E and less significantly the quantity χ^2_{min} depend on the granularity and separate probability distributions have to be build for each of the three granularity regions (details on the calorimeter system geometry may be found in chapter 1.5).

Hence, the number of probability density functions normalized and stored in the LHCb condition and simulation databases in the form of histograms is given by the two converted/not-converted categories, the 3 regions, the 3 variables, the 10 transformed energy bins and the signal and background cases.

The figures 6.3, 6.4 and 6.5 show the distributions of the variables. Here, the three regions are merged in the same bi-dimensional plots, the distinction being kept between converted and not-converted [3], signal and background.

[3] As mentioned, the criterion is the SPD information.

The estimator is evaluated for each candidate by evaluating the likelihood from the 3 pdf corresponding to the three variables of interest both in the signal and background hypothesis. The difference in log-likelihood ($\Delta \log \mathcal{L}$) under the two cases is calculated and is used to select photons.

6.6 Performances

The estimator output is a quantity roughly distributed between -10. and +10 as showed on figures 6.7. The building of such a $\Delta \log \mathcal{L}$ estimator is simple and allows to conveniently introduce new variables at a later stage if needed.

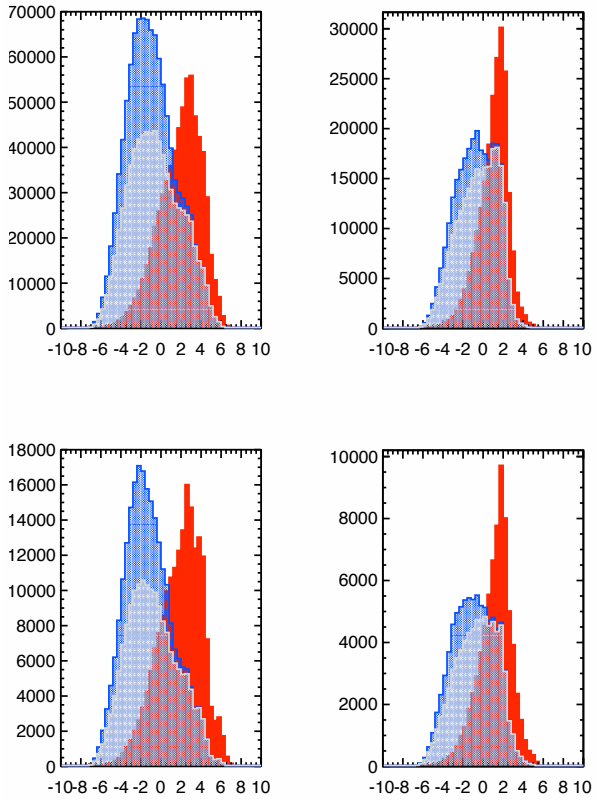

Figure 6.7: The four plots show the $\Delta \log \mathcal{L}$ output in the not-converted (no SPD hit) and converted (SPD hit) cases on the left and right respectively. The top plots correspond to a minimum P_t of the photons of 200MeV. The P_t cut applied for the bottom distributions is 500MeV. The photon signal is in red, the background is in blue. The gray histogram shows the photon background $\Delta \log \mathcal{L}$.

Two large B inclusive Monte Carlo samples have been used to produce the probability density functions and to test the algorithm. The former is a Monte Carlo set of 258998 events, the latter is a different set of 110999 events. The probability density functions have been compared

in different case (min-bias samples, B inclusive, $B \to K^*\gamma$, $B \to \pi^0\pi^+\pi^-$). No sizable difference was noticeable in the distributions as the pdf are calculated and normalized in different energy bins. The $B \to K^*\gamma$ sample is slightly specific as the signal photon P_t is here very large and a fraction of the background comes from merged π^0. A dedicated analysis is done in this case [57]. Finally, it was also tried to apply the first level trigger to the events before identifying the photons. But the trigger selection effect is marginal.

The figure 6.7 shows the $\Delta \log \mathcal{L}$ calculation for the signal, background and photon background in the converted and not-converted cases. The $\Delta \log \mathcal{L}$ being $\mathcal{L}_\gamma - \mathcal{L}_{\text{background}}$, the signal gets a larger value the maximum being reached at 2. The background is mostly centered around -2. The contribution of the photons in the background is not evenly distributed, the larger the result, the larger its fraction. Above 0, the background is essential made of photons.

Cutting on the $\Delta \log \mathcal{L}$ permits to select the candidates. The efficiency and purity of the selection are used to evaluate the performances of the algorithm[4]. In the specific not-converted(converted) cases, the definition chosen for the corresponding efficiency and purity is

$$\begin{cases} \epsilon_{\not{\text{SPD}}/\gamma \not\to ee} = N^{\gamma}_{Rec(\not{\text{SPD}})} / N^{(\gamma \not\to ee)_{MC}} \\ \\ \epsilon_{\text{SPD}/\gamma \to ee} = N^{\gamma}_{Rec(\text{SPD})} / N^{(\gamma \to ee)_{MC}} \end{cases} \tag{6.5}$$

$$\begin{cases} \rho_{\not{\text{SPD}}} = N^{\gamma}_{Rec(\not{\text{SPD}})} / (N^{\gamma}_{Rec(\not{\text{SPD}})} + N^{\text{bkg}}_{Rec(\not{\text{SPD}})}) \\ \\ \rho_{\text{SPD}} = N^{\gamma}_{Rec(\text{SPD})} / (N^{\gamma}_{Rec(\text{SPD})} + N^{\text{bkg}}_{Rec(\text{SPD})}) \end{cases} \tag{6.6}$$

where $N^{\gamma}_{Rec(\not{\text{SPD}})}$ ($N^{\gamma}_{Rec(\text{SPD})}$) is the number of reconstructed photons identified having no hit (having a hit) in the SPD. N^{bkg} is the corresponding number for the background and $N^{(\gamma \not\to ee)_{MC}}$ ($N^{(\gamma \to ee)_{MC}}$) is the number of Monte Carlo true photons being not converted (converted), according to the Monte Carlo truth information and reconstructible (i.e. having an associated cluster whose χ^2_{min} is larger than 4 and whose P_t is larger than 200MeV).

The plots of figure 6.8 have been calculated from those definitions and the test B inclusive Monte Carlo sample described before. Notice that although the efficiency is stable whatever the different types of Monte Carlo sample used, the purity may slightly vary (especially for $B \to K^*\gamma$ samples as explained above). The not-converted photons are the easiest to select (red on 6.8).

In the case of a B inclusive sample, a cut at $\Delta \log \mathcal{L} \leq 0$ would lead to an overall efficiency and purity of 81% and a purity of 61%. Considering the fact that the sample is already selected according to $\chi^2_{\text{min}} \leq 4$, the global efficiency is reduced to 70%. Those quantities for reconstructible photons are 84% and 61% (73% and 61%) in the not-converted case (converted one).

The effect of the selection is highly visible when selecting low P_t neutral pions as showed on figure 6.9. Four situations are plotted corresponding to four cuts applied on both photons $\Delta \log \mathcal{L}$ at values $-\infty$ (no cut), -2, 0 and 2.

The Monte Carlo versus data agreement is being looked at presently. The figure 6.10 shows the comparisons for the three variables of interest used in the estimator algorithm. The PRS

[4]The efficiency and purity are defined respectively by $\epsilon = N^{\gamma_{MC}}_{Rec} / (N^{\gamma_{MC}})$ and $\rho = N^{\gamma_{MC}}_{Rec} / (N^{\gamma_{MC}}_{Rec} + N^{\text{bkg}}_{Rec})$

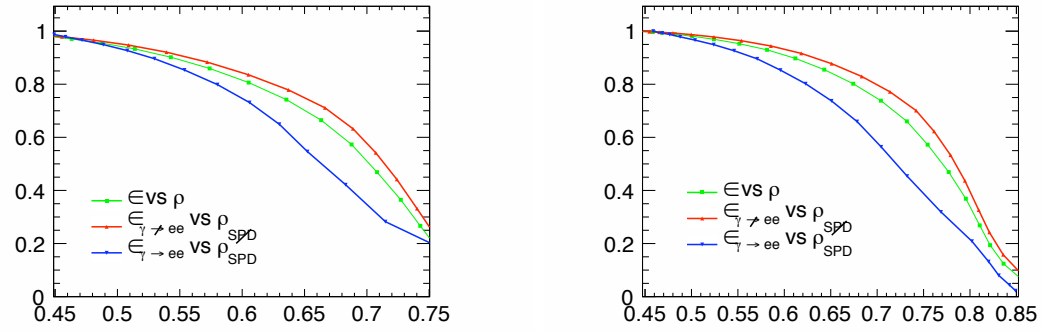

Figure 6.8: Left: efficiencies (ordinate) versus purities (abscissa) as defined in the text for the overall photon sample, the not-converted and converted case. Each point correspond to a specific cut on the $\Delta \log \mathcal{L}$ estimator. The efficiency is evaluated for "reconstructible" photons. Right: the same plot as on the left, but here the P_t cut for the reconstructible photons is increased to 500(MeV).

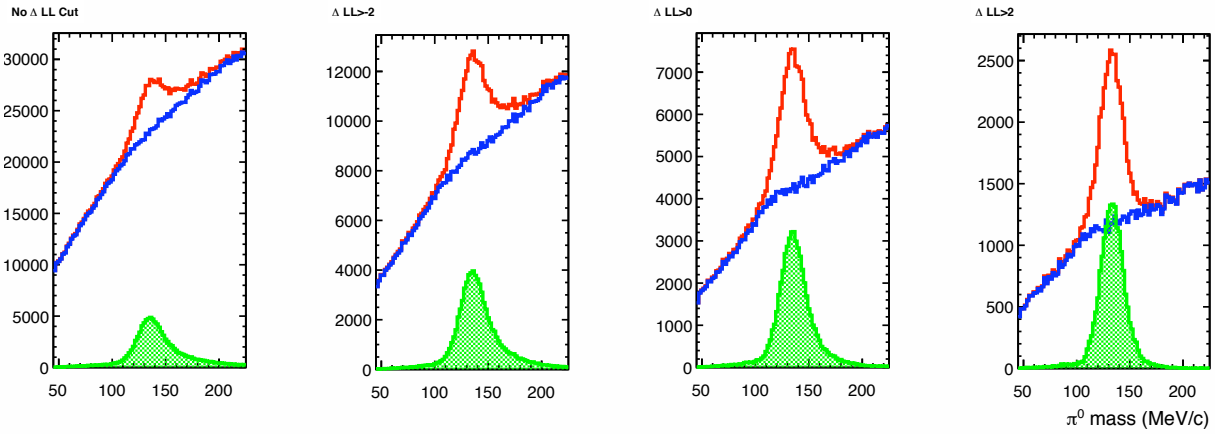

Figure 6.9: The histograms show the effect of the photon identification of the π^0 mass distribution. Four cuts have been applied from left to right : no cut, a but at -2, at 0 and at 2 respectively. The red histogram show the full π^0 candidate sample, the green being made of reconstructed π^0 associated to a true Monte Carlo neutral pion.

energy and the track-cluster distance parameter χ^2_{min} do not seem to show any significant disagreement. The ratio E_{seed}/E of the energy of the cluster seed by the total energy of the cluster looks is less well reproduced by the Monte Carlo. This is especially true for the "SPD hit" candidate sample.

It is not easy to identify the reasons for this as in the photon case it is difficult to extract a pure and unbiased test sample from the data. The unexpected beam conditions since August 2010 make difficult any Data-Monte Carlo comparison. The beam focusing at LHCb should be such that the average number of interaction per crossing should be of $\mu = 0.4$. In 2010 and

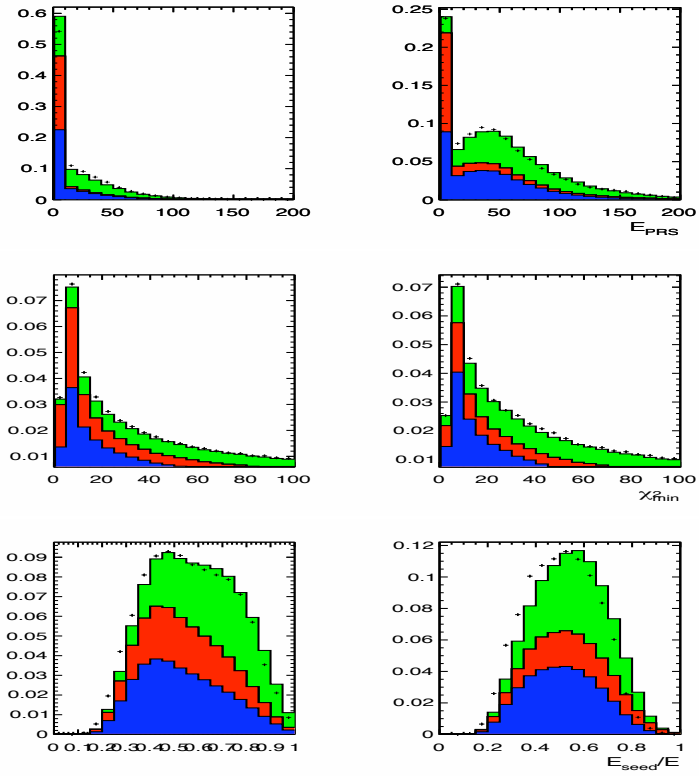

Figure 6.10: Data vs Monte Carlo agreement for the three variables of interest used in the present estimator, the PRS energy (top), χ^2_{min} (middle plots) and the ratio E_{seed}/E (bottom). The left and right columns correspond to the candidates having no SPD hit in front of the ECAL cells and the candidates with a SPD hit, respectively. The histograms are the accumulation of the background photons (blue), the other backgrounds (red) and the signal (green).

as the number of bunches along the accelerator did not exceed 400 it was decided to have the same focusing at LHCb as at the ATLAS and CMS interaction points, with a β^* value of 2.5m. These conditions led to a larger pile-up than expected. All the data Monte-Carlo comparisons suffer from this. The present situation should be transitory as we expect 2011 condition to be less aggressive, moreover the present Monte Carlo simulation do not integrate the pile-up conditions experienced in 2010. But it is clear that such a pile-up would also produce a larger contamination of low energy particles that may affect the averaged response of the calorimeter.

As was pointed out already, having an unbiased photon sample that could be used in order to extract probability distributions from the data is not possible. A path that was followed recently consisted in selecting photons from electron bremsstrahlung. But the purity and efficiency obtained from such a selection do not permit to get clean enough distributions. Nevertheless, this could be used as a cross-check.

The algorithm presented here was implemented in 2009 and is part of the standard reconstruction and analysis packages of LHCb[5]. The probability density functions are integrated to

[5]The packages are called Brunel and DaVinci respectively and are part of the LHCb Gaudi software frame-

the standard LHCb condition and simulation databases, so that the estimator is evaluated by default on the calorimeter clusters both in the simulation and in the data sample recorded with the detector.

work.

Chapter 7

Absolute calibration of the ECAL and Preshower

Contents

7.1 Introduction 117
7.2 Toy Monte Carlo 119
7.3 ECAL and PRS extraction method 124
7.3.1 Energy scale extraction 124
7.3.2 The β coefficients 125
7.3.3 Width minimisation 125
7.4 LHCb Monte Carlo 127
7.4.1 Extraction of the calibration from the MC-truth 127
7.4.2 β extraction on a Monte Carlo sample 128
7.5 β extraction from the 2010 data sample 132

7.1 Introduction

The calorimeter system must be precisely calibrated in order to correctly determine the energy of the absorbed particles. The technique used to calibrate the HCAL relies on the LED [95], the position of the mip and the flattening of the energy flow [37]. The ECAL is calibrated altogether from the position of the π^0 mass and from the energy flow method. Moreover, the ECAL gain is regularly monitored both by the LED and the energy flow [37, 94, 76].

The technique foreseen to calibrate the PRS consists in getting the position of the mip as it is measured in the scintillator. This measurement gives a precise cell to cell calibration but does not permit to extract the absolute energy absorbed both in the scintillator and the lead and that is usually modelized by a factor β (see section 3.1 of [59] and [71, 58]):

$$E_{PRS} = \beta E_{Scint.} \tag{7.1}$$

where E_{PRS} is the energy lost in the PRS and $E_{Scint.}$ is sometimes called the active energy, and so that the total energy deposited in the calorimeter by electromagnetic particles is obtained by:

$$E = \alpha E_{ECAL} + \beta E_{Scint.} \tag{7.2}$$

Hence, the calibration of the calorimeter requires altogether the determination of the ECAL and PRS parameters, α and β. This appears to be difficult especially because α is in fact extracted per cell and α and β are strongly anti-correlated.

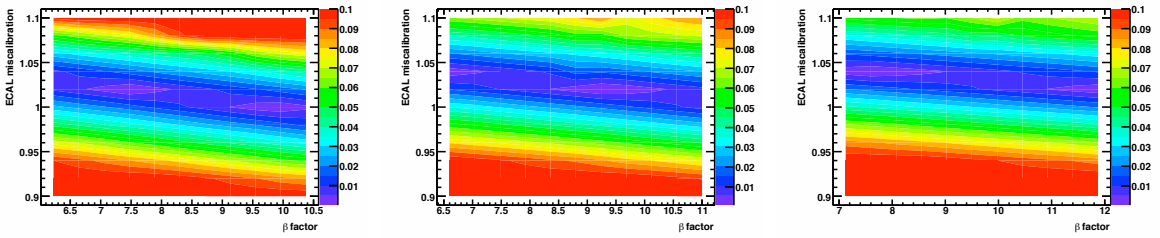

Figure 7.1: Correlation between the ECAL miscalibration and the PRS β factor. The parameter plotted on the z axis is the absolute value of the difference between the reconstructed π^0 mass and the PDG value. The graphs are for the outer (left), middle (center) and inner (right) regions of the calorimeter.

Another solution was envisaged and consisted in operating in two steps. First, a sample of π^0 whose γ do not deposit energy in the PRS is built. This corresponds to roughly $e^{-7/9\times 2.5X^0} \approx 14\%$ of the photons or 2% of the neutral pions. The ECAL is calibrated by tuning the reconstructed mass to the PDG mass [1]. Then, the full π^0 sample is used in order to tune the β of the PRS so that the mass reconstructed from the total sample is also the PDG mass. This approach suffers from several problems. Equation 7.2 and figures 7.1 show that E_{ECAL} and E_{PRS} are fully anti-correlated. The energy repartition between the ECAL and the PRS is such that a small error on the ECAL calibration leads to a strong effect on the β estimation. Moreover, it appears that the ECAL calibration depends on effects difficult to control (pile-up, S-shape correction [2],...) so that an absolute calibration of the ECAL at the percent level independent of the selection used to calibrate is difficult.

The error δ_β on β can be roughly expressed from the error on α, δ_α, and the fraction of energy x deposited in the PRS with respect to the original particle energy[3]:

$$\delta_\beta \approx \frac{1-\delta_\alpha(1-x)}{x} \tag{7.3}$$

[1] The Particle Data Group 2010 [84] mass is 134.98MeV/c^2.

[2] The most naive impact position reconstruction in the calorimeter may be done with a simple barycenter procedure. Nevetheless, such a method leads to a bi-dimensional error (in the (x, y) plan of the calorimeter) error having the shape of an "S" and that may be corrected with an "S-shape correction". More details may be found in [56]

[3] Notice that the average ratio of energy deposited in the PRS by the total energy is a function of the total energy of the particle and can only be used in a simple model. In the following (toy model, MC and data β extraction) the formalism is not based on this ratio.

If x is zero, it is obvious that no information can be extracted from the data, and more generally the lower the x fraction the larger is the dependency of β with α as can be seen from figure 7.2, for three different values of x. The curves of 7.2 can be compared to the 2 dimensional plots of figure 7.1 from which we could extract an effective x parameter in each zone. This is done here from MC true information and cannot be done on data.

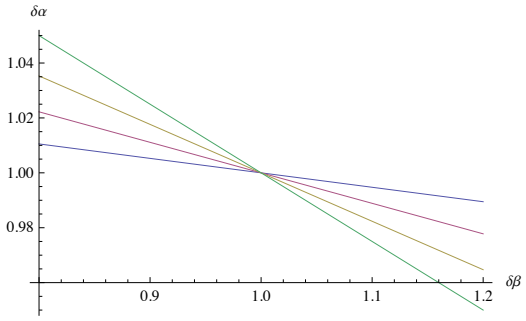

Figure 7.2: Approximated relation between an absolute miscalibration of the ECAL and the corresponding error on a simple β extraction. The relation extracted here depends on the introduced fraction of energy in the PRS over the total energy of the particle, called x in the text. The four curves are for four values of x, 5% (blue), 10% (red), (brown) and 20% (green).

Notice, that the unbalanced effect of the ECAL versus the PRS is due to the relative amount of energy deposited in both sub-detectors and also shows that the β PRS calibration is a second order effect. Nevertheless, the PRS calibration is a necessary step towards a precise ECAL and the overall calorimeter system calibrations.

A new method less affected by the ECAL energy scale had to be found. The width of the π^0 mass distribution independently of the peak position looked as a good candidate for such a calibration.

7.2 Toy Monte Carlo

In order to understand the effects contributing to the π^0 mass width, a simulation was written based on :

- The π^0 energy and transverse energy. A 2D (E,E_t) map is extracted from a large Monte Carlo sample of minimum bias events (see figure 7.3).
- The energy resolution of the ECAL

$$\frac{\sigma_E}{E} = \frac{10\%}{\sqrt{E}} \oplus 1.5\% \tag{7.4}$$

- An average error on the photon position reconstruction of 5 mm (this value corresponds to the spatial resolution expectation for the middle region of the calorimeter). We suppose here that only local miscalibrations may have an impact on the S-shape position reconstruction and that whatever the overall miscalibration of the ECAL or the PRS the spatial resolution is constant.

- The fraction of energy of the photons deposited in the PRS and the ECAL depending on the energy of the incoming particle (see figure 7.4) is not assumed as a constant as before. The corresponding distribution is extracted from Monte Carlo simulations of minimum bias events. No SPD hit should be present in front of the ECAL cluster. Moreover, the PRS energy is summed up over the 9 cells facing the 3×3 ECAL cluster.

The simulation is done by generating from the π^0 kinematics (figure 7.3) the 4-vectors of the two photons. An E_t cut on each photon of 200 MeV is applied and corresponds to the minimum threshold used in the standard LHCb photon reconstruction. The π^0 considered further should pass this requirement. Then, the photon energy is attributed partly to the ECAL and to the PRS according to figure 7.4 by pulling a random fraction. This is done by selecting the slice of the 2D plot which corresponds to the photon energy considered and extracting a random number from this resulting one-dimensional distribution. The ECAL part is smeared by the detector resolution (see equation 7.4). An overall PRS energy gaussian smearing is also added and is calculated either from the RMS of the one-dimensional slice obtained to evaluate the PRS energy fraction or from a function fitted to the data and giving the PRS absorber energy RMS (figure 3.3 of [59]). Half the RMS is assumed to be coming from the PRS energy smearing only, independently from the energy fluctuations between the ECAL and the PRS, which is a strong assumption. From the resulting toy Monte Carlo simulation it is possible to extract the

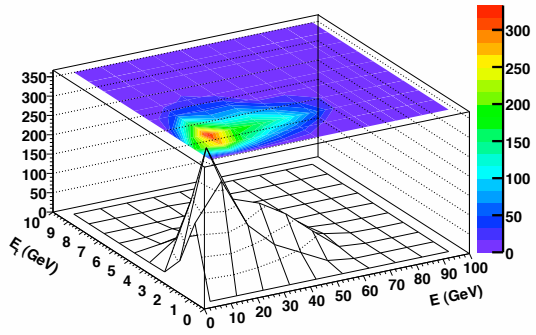

Figure 7.3: E versus E_t 2D distribution of π^0 from a simulated minimum bias sample. A constraint on the distance between the 2 photons (distance larger than 3 times the cell size of the calorimeter region) is applied and removes the merged π^0 contribution.

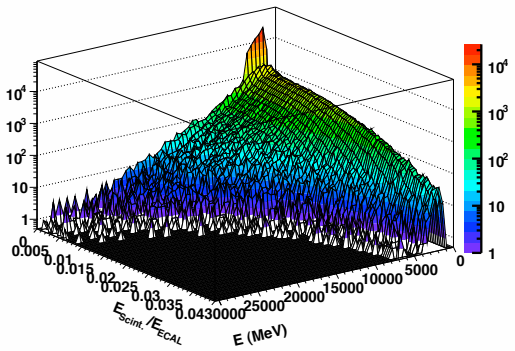

Figure 7.4: The figure represents the ratio of the energy seen by the PRS ($E_{Scint.}$, no β factor weighting) by the ECAL energy versus the incoming particle energy. The plot is rotated with respect to the usual representation to clearly show the variations.

different contributions to the π^0 mass width. Figure 7.5 shows the width obtained depending on an overall factor applied to the β parameter and the different contributing effects simulated here:

- The ECAL energy resolution has no direct effect on the width curve, but the parabolic shape is less pronounced the larger is this contribution. In order to be sensitive to β, it is thus preferable to perform first the relative calibration of the cells. The same conclusion

α	0.95	1.00	1.05
β	0.93	0.99	1.05

Table 7.1: Results of the π^0 mass width minimisation with respect to β in three ECAL miscalibration cases.

is relevant concerning the ECAL spatial resolution. The two effects could be modelized by a constant σ_{ECAL}.

- The β correction is the parameter we want to extract and figure 7.5 shows that a fit of the width should permit to obtain it. The green contribution is from a perfect calorimeter except for β. Clearly, if β is correct (i.e. the multiplicative correction on β, δ_β is 1), the detector is perfect and the width is 0. If β is lower(larger) than zero, then mass peak leaks towards the lower(larger) masses and the width increases linearly with β. A contribution $\sigma_\beta(\beta - \beta_{true})$ is taken for the effect, where β_{true} is the correct β value .

- The purple curve of figure 7.5 includes both the β error (previous bullet) and the smearing of the preshower energy. The latter contribution is also a linear effect but that is null for a β value of zero. This effect will distort the parabolic shape of the final width curve and should be corrected. A spread $\beta\sigma_{PRS}$ will be included for this contribution

The $\sigma_\beta(\beta-\beta_{true})$ contribution is the effect we use to extract β and may be easily understood from the following.

Writing the mass of the π^0

$$m^2 = 2(1 - \cos\theta)E_1E_2 \tag{7.5}$$

we take on average the same energies for the 2 photons, suppose no error both on θ and the total reconstructed energy and express $x = E_{PRS}/E_{Tot}$. The parameters δ_α and δ_β being the multiplicative corrections so that

$$\begin{array}{rcl} \delta_\alpha & = & \alpha/\alpha_{true} \\ \delta_\beta & = & \beta/\beta_{true} \end{array} \tag{7.6}$$

equation 7.5 becomes

$$(m - \langle m\rangle)^2 \approx m_{PDG}^2((\delta_\alpha - \delta_\beta)\sigma(x))^2 \tag{7.7}$$

Hence, the smallest contribution to the π^0 mass width is not exactly the best absolute value of δ_β (i.e. 1 in our Monte Carlo toy), but the value of β having the same error as the error on α. Thus, working on the π^0 mass width turns equation 7.3 into

$$\delta_\beta \approx \delta_\alpha \tag{7.8}$$

and reduces the problem caused by the unknown fraction x to a constant contribution to the width. Moreover, this means that in theory, the error on β is of the same order as the one we have on α. To phrase the previous equation differently, an equal miscalibration of α and β leads to a new π^0 mass distribution whose width is null (as if the detector was perfect) but whose central value is displaced by the amplitude of the miscalibration both on the ECAL and

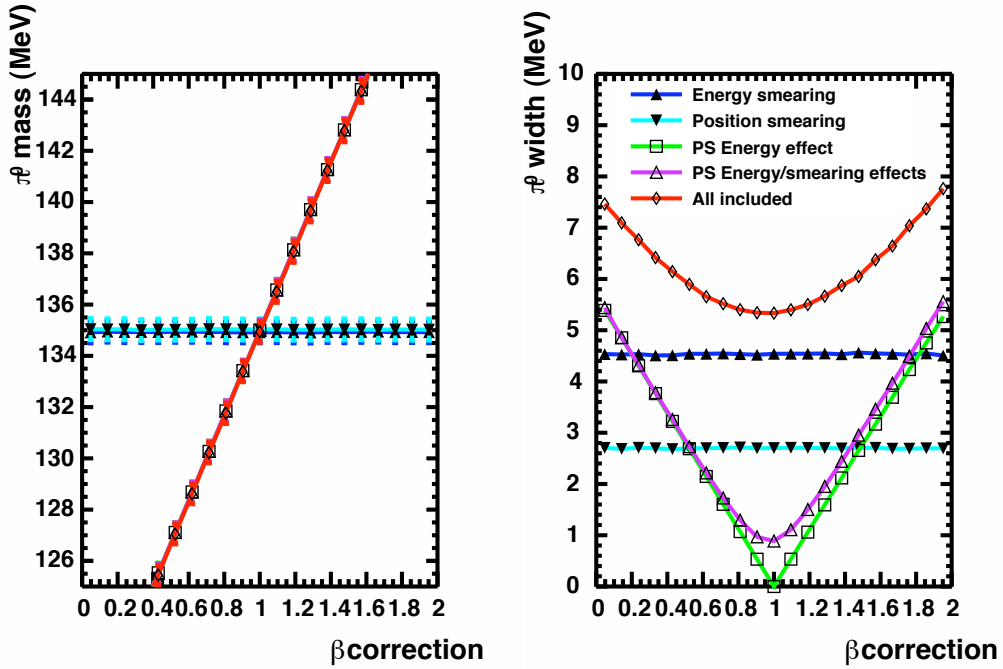

Figure 7.5: The two plots show the reconstructed mass and the width obtained from the toy Monte Carlo for different β corrections hypothesis, each point being extracted from 100000 generated π^0. The width contributions (right plot) are separated in order to emphasize the effects. The ECAL resolution is split between the energy resolution (blue) and the ECAL spatial resolution (cyan). The PRS effects are the β correction effect that is used for the calibration (green) and the PRS energy smearing (purple). The red curve is the overall mass spread effect. The mass evolves with β (left plot) only when considering the PRS effects which are here superimposed on the red curve. Of course, in this toy Monte Carlo the optimal β is for m_{PDG} and no effect on the neutral pion mass appear if the PRS is not considered (blue curves).

PRS. As we uniquely rely on the width to extract β we cannot remove the effect due to the error on α but we may hope to reach a few percent accuracy for this parameter and the fraction x being of the order of 10-20%, an error of 1% on β is a negligible effect.

The question on how we could reach a good precision on α without knowing β appears at that point. A method consisting in getting β from a first guess of α followed by an adjustment of the full mass distribution to the PDG mass should, after a few iterations, lead to the correct α and β values. The method will be described in the next section.

Finally, another effect has to be mentioned and is linked to the angle distribution of the two photons. The position error which is roughly gaussian in x and y distorts the m_{π^0} distribution especially at low angles. This effect is coupled to δ_β and leads to an overall deformation of the curve of the π^0 width with respect to β. The effect is

- proportional to the spatial resolution of the calorimeter,

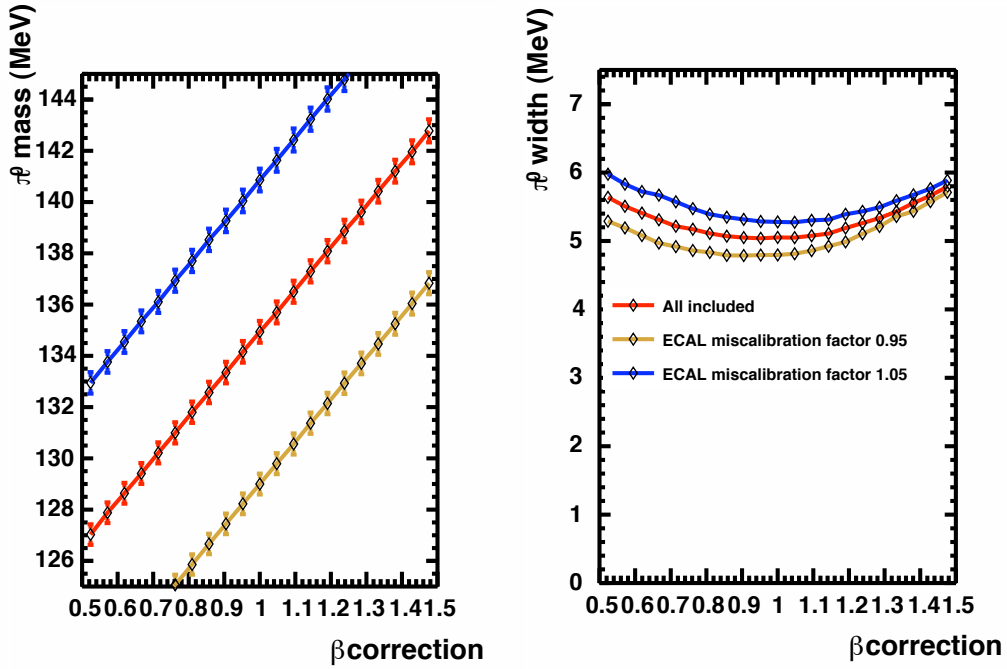

Figure 7.6: Results of the width minimization after applying a miscalibration factor on the ECAL of 0.95, 1.00,1.05. The left plots shows the corresponding effect on the π^0 mass reconstruction. The extraction of the minimum gives the value of β (see table 7.1). A statistics of 100000 π^0 have been generated per point.

- larger for small angles or high energy π^0,
- and is proportional to β.

The spatial resolution that must be simulated to see the effect is large (typically 20 mm) compared to the true calorimeter resolution. Moreover, when two photons coming from a π^0 are close to each other, the cluster overlaps. It leads to energy over counting and mixing as a fraction of each photon may potentially be present in the two clusters. We get rid of this effect by requesting an inferior limit on the distance of the two clusters. This cut reduces drastically the dependency of the π^0 mass width with the angular aperture of the two photons. Moreover, the best spatial resolution is obtained in the region of the calorimeter where the aperture is the smaller so that the effect is not specifically enhanced in a zone according to its granularity. And finally, looking at the effect with the Monte Carlo model described here, it appears that the angular aperture leads to a spread contribution linear in β which is hence swallowed by the σ_{PRS} contribution when the mass width curve is fitted. In the following σ_{PRS} is called $\sigma_{PRS+\theta}$.

Although the advantage of working on the width instead of the absolute π^0 mass to calibrate the PRS is now clear, the difficulty is in extracting the mass width and its dependency with β with a sufficient precision as can be seen from figures 7.5 and 7.6. We will see in the next chapter that the needed statistics is large.

The different contributions mentioned above are quadratically summed and build the shape of the fit function used to extract the corrected β:

$$\sigma^2(\beta, \beta_{corr}) = \sigma^2_{ECAL} + \sigma^2_{\beta}(\beta - \beta_{corr})^2 + \beta^2\sigma^2_{PRS+\theta} \tag{7.9}$$

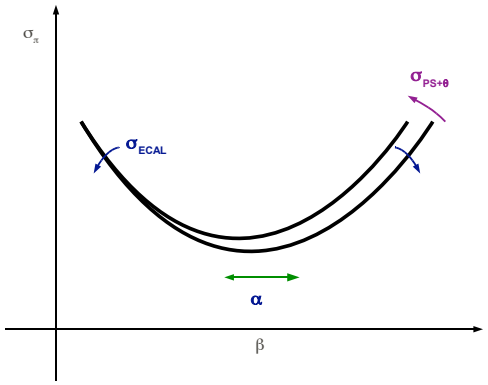

Figure 7.7: The figure shows the effects modifying the π^0 mass curve with respect the β parameter. The four effects here have been described in the text and are σ_{ECAL} which tends to flatten the parabolic shape keeping the symmetry, the ECAL miscalibration (shifted α) leads to an equivalent offset on β. Finally the PRS energy resolution and ECAL spatial resolution have an asymmetric effect distorting the parabola at high β.

Figure 7.7 shows the different effects governing the dependency of the π^0 mass width on the beta parameter.

7.3 ECAL and PRS extraction method

7.3.1 Energy scale extraction

The previous study was based on a simple Monte Carlo toy model which permitted to explain the method to extract β, it is necessary to confront it to a Monte Carlo sample and ultimately to real data.

The technique allows, as we will see, to extract both the PRS and ECAL absolute energy scale from the data. Both the π^0 width and the mass position are necessary and the extraction is performed iteratively:

1. A first set of values is chosen for α and β. Here, we use the Monte Carlo expectations. It was already mentioned that the ECAL and PRS cell per cell relative calibrations must be performed before the extraction of the ECAL and PRS absolute scales.

2. A correction on β is evaluated from the minimisation of the width of the π^0 mass distribution. At this stage the absolute position of the π^0 mass was not used in the algorithm.

3. The correction on β being extracted from the previous minimization, the ECAL energy scale is corrected from the error on the π^0 mass. This new energy scale α is used to build a new set of mass curves for a range of β value hypothesis.

The algorithm can be used iteratively and a new correction can be extracted. In practice, α is already known to a few percent. After the first α extraction, the variation is at most of this amplitude. The correction on β obtained after the first iteration is so small, that there is no real reason to perform any iteration.

7.3.2 The β coefficients

The β extraction has to be done per region : the characteristics of the cells (size, wave shifting fibre length, ...) are different. This is a feature that is already implemented in the reconstruction.

Apart from the regions, the calibration coefficient are different for photons and electrons and as the shower of the electrons starts before, we expect β to be larger for electrons than for photons.

In the case of the β parameter for photons, the π^0 mass curves are built from reconstructed γ that did not have a hit in the SPD and did not convert before the calorimeter system. The electron case is treated specifically by building mass curves from fully converted photons that have a hit in the SPD in front of the ECAL cluster seed.

As a whole 6 values of β are extracted for the 3 regions and in the 2 cases, photons and electrons.

7.3.3 Width minimisation

π^0 mass minimization not using β

The sensitivity of the method relies on the variation of the π^0 mass width with respect to β. The largest contribution to the π^0 width comes from the ECAL miscalibration. If it is too significant, the width can be such that the parabola shape showed on 7.7 and 7.12 is not well pronounced and the β correction minimization becomes very imprecise. Hence, it is necessary to reduce any other contribution that doesn't come from β.

- The LHCb calorimeter cells are calibrated in time by measuring the energy deposited in three consecutive events centered on a "true" bunch crossing [4]. The best sensitivity to evaluate the correct timing consists in determining the clock phase so that the energy is well-balanced between two crossings. From the amount of energy deposited in the calorimeter cells before, during and after the bunch crossing, the timing of each one of the 6016 cells of the ECAL is tuned [66].

- The relative energy calibration of the ECAL is performed in several steps:

[4]The LHCb trigger system can be configured so that when an interaction occurs, several consecutive trigger signals are sent to the front-end and lead to the acquisition of a window of events around the actual interaction at the origin of the trigger.

- The LED pulses are used to estimate the gain of the cells by measuring the pulse width. The precision obtained from this method is better than 10% [35].
- As a second step, the ECAL cell response is flattened by integrating the amount of energy seen on each cell. The sum per cell is normalized by the number of hits and the local variation are smoothed by applying gain corrections. The expected precision reaches 5% at this level [37].
- The next step consists in building a π^0 mass curve per cell [5], its energy deposits and the other clusters of the ECAL being used. A fraction of the error on the mass reconstruction is due to the cell gain error and can be corrected iteratively. Notice that at this stage, the selection imposes a cut on the PRS energy deposit in front of the ECAL clusters. The PRS scale is not calibrated yet and a dependency on the PRS would lead to a systematic error on the ECAL calibration of the cells. The precision at this level is of 2.5% although it is difficult to evaluate [1].
- The last step consists in using again the energy flow method which permits to recover from some bad features of the calibration from the π^0 mass reconstruction affecting for example the borders of the calorimeter regions or the neighbours of dead or noisy channels. The energy flow method treats more cleanly those specific cases.

As already mentioned, the PRS relative calibration is done by equalizing the position of the mip peak for all the cell of the PRS.

The background has also an effect on the π^0 mass width and increases it. A selection on the $\Delta \log \mathcal{L}$ at -1. permits to reduce the width without reducing significantly the statistics (see the previous section).

π^0 mass width minimization from β

From a relative calibration of the ECAL and PRS, the π^0 mass curve is constructed for different β values with steps of 5%.

Each mass curve is then minimized by the sum of a gaussian and a first order polynomial. Only the π^0 peak region is fitted. This is done by:

- Fitting first over a large interval. This is necessary as the variation of β leads to a shift of the π^0 mass peak position, that has to be properly determined.
- The parameters are then used as the initial values for a second fit using the same function but for which the fit interval is reduced to $\pm 2.5 \times \sigma$, σ being the standard deviation extracted from the gaussian of the first fit.

The figures 7.8 (Monte Carlo initial β value, no correction) and 7.11 (mass curve after best estimated β correction) show two mass curves and the result of the fits.

Finally and from the previous fits, the width curve (see an example on 7.12) is built and is minimized according to the function 7.9.

[5] For each cell, all the π^0 for which one of the two photons deposits a large fraction of its energy in this cell are built.

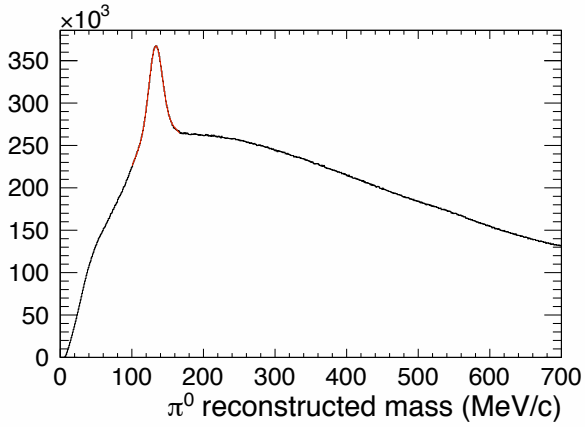

Figure 7.8: Reconstructed mass curve built from pairs of photons. This curve is obtained on the not converted sample, in the outer region and for $\beta = 8.3$ (correction=1.). The mass width extraction with the corresponding fit are shown in red on the mass curve.

7.4 LHCb Monte Carlo

7.4.1 Extraction of the calibration from the MC-truth

In order to determine the precision of the method, the ECAL and PRS "true" calibration coefficients α_{true} and β_{true} have to be extracted. This is done here by using the Monte Carlo truth information and evaluating corrections $\delta\alpha_{\text{true}}$ and $\delta\beta_{\text{true}}$ on the parameters α_{rec} and β_{rec} actually used in the reconstruction. A list of photons γ_{MC} is built and the associated reconstructed photons γ_{rec} are determined.

To calibrate the ECAL independently from the PRS a sub-sample of those γ_{MC} is extracted by requiring that no energy was deposited in the PRS. Let's recall, that here, we make an intensive use of the MC "truth" as we want to get the "best" possible calibration parameters. The ultimate aim is to compare this estimation to the β extraction based on the method introduced in the previous sections. The difference between the energy reconstructed and the MC truth energy $\delta\alpha_{\text{true}}E_{\gamma_{rec}} - E_{\gamma_{MC}}$ is fitted by a gaussian. Depending on $\delta\alpha_{\text{true}}$, the reconstructed energy of the photons is shifted and the gaussian fit slightly moves, as seen on the plot 7.9. A linear fit of the obtained calibration curve permits to extract the best estimation for $\delta\alpha_{\text{true}}$ in the three regions, values which are listed in table 7.2.

The extraction of $\delta\beta_{\text{true}}$ is very similar to the determination of $\delta\alpha_{\text{true}}$, but this time, the full MC sample is used, no constraint is imposed any more on the photon deposit in the PRS and $\delta\alpha_{\text{true}}$ is kept constant, at the value listed in table 7.2. The curves of 7.10 give the expression

$$(\delta\alpha_{\text{true}}E_{\gamma_{rec}} + \delta\beta_{rec} \times \beta_{rec}E_{PRS} - E_{\gamma_{MC}}) \tag{7.10}$$

where $\delta\beta_{rec}$ is the correction on the original β used in the reconstruction β_{rec}. The linear fit results is given in table 7.2.

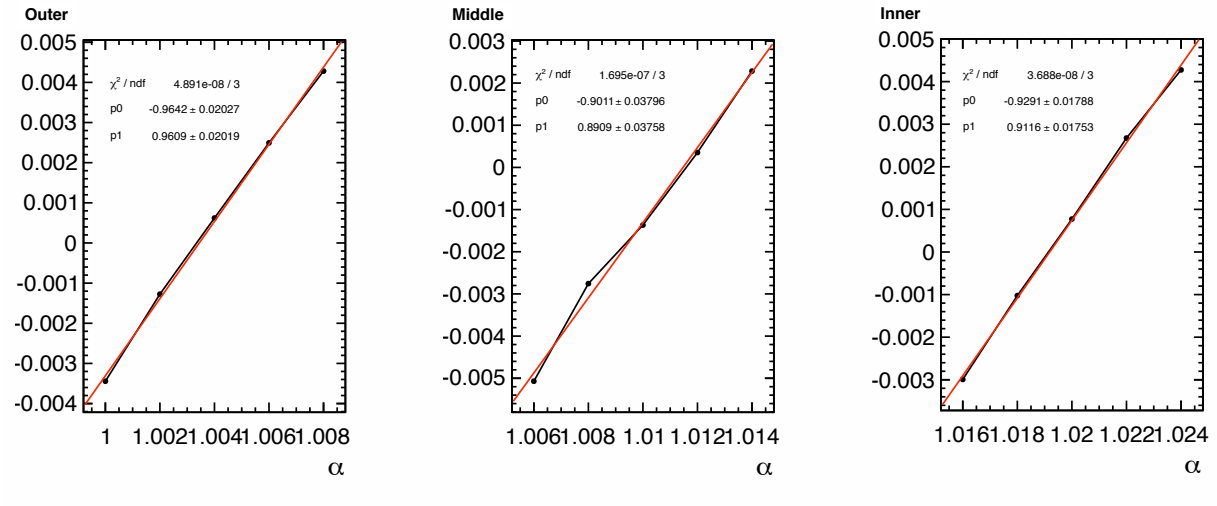

Figure 7.9: Absolute calibration of the ECAL using the Monte Carlo truth information in the three regions of the calorimeter. The difference $\delta\alpha_{\text{true}} E_{\gamma_{rec}} - E_{\gamma_{MC}}$ is shown on the ordinate for several $\delta\alpha_{\text{true}}$ coefficients hypothesis. A linear fit of the curve permits to extract the best estimation from the Monte Carlo "truth".

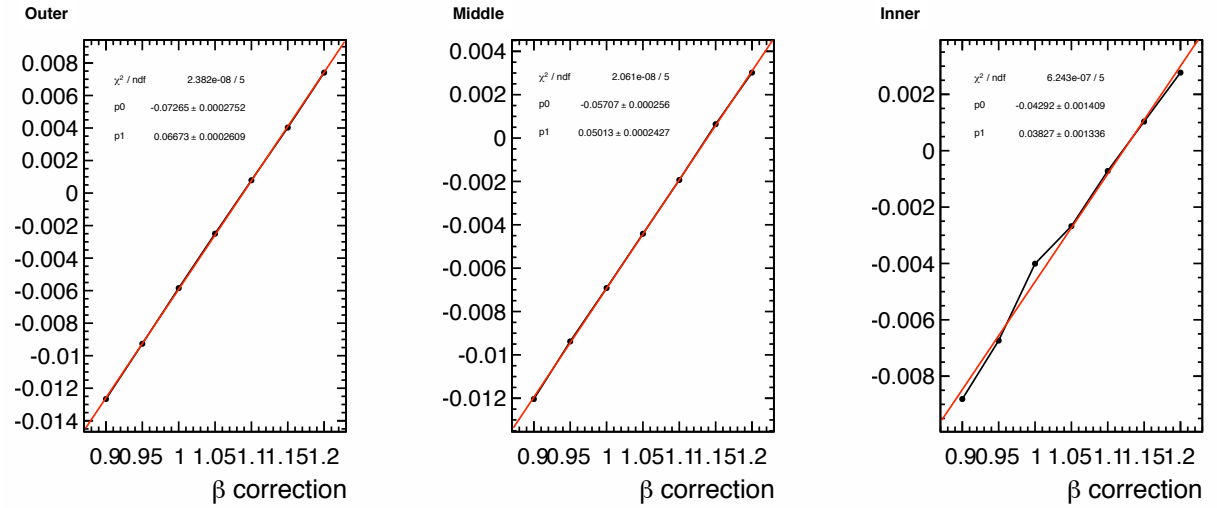

Figure 7.10: Extraction of the β_{MC} coefficient from the MC truth information and after ECAL α_{MC} determination. The results for the three regions are given.

7.4.2 β extraction on a Monte Carlo sample

The "theoretical" coefficients β_{true} being known, this value is compared with the experimental extraction.

A large data sample of 69155667 events of minimum bias type, generated at 7TeV (MC2010) is used. The reason for such a large sample is that it will be split in 16 sub-samples roughly

Zone	$\delta\alpha_{\text{true}}$	β_{rec}	$\delta\beta_{rec}$ correction	β_{true}
Outer	1.003	8.3	1.089	9.04
Middle	1.011	8.5	1.138	9.67
Inner	1.019	9.5	1.122	10.66

Table 7.2: Values of the calibration coefficients of the ECAL and PRS in the three regions of the system.

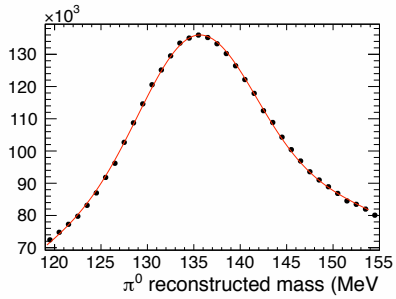

Figure 7.11: Detail of the π^0 mass histogram around the peak of the distribution with the gaussian fit (red curve) in the outer zone (photon case) and for the full real data sample.

Sample	N_{Outer} $(\gamma\gamma)$	β_{Outer} $(\gamma\gamma)$	N_{Middle} $(\gamma\gamma)$	β_{Middle} $(\gamma\gamma)$	N_{Inner} $(\gamma\gamma)$	β_{Inner} $(\gamma\gamma)$
0	158107	9.34	66876	10.52	91682	10.56
1	177830	9.21	77186	9.47	106302	9.93
2	169104	9.26	72519	10.17	97177	10.23
3	169608	9.39	72031	9.47	100694	10.17
4	159330	9.64	70081	10.65	89567	10.48
5	169429	9.12	75316	6.86	98757	11.75
6	166449	8.82	76794	9.47	97305	9.93
7	170941	9.41	73606	9.79	100980	12.08
8	178094	9.45	78610	9.82	104130	10.34
9	175973	9.30	77432	9.63	104714	9.54
10	161193	9.40	71578	9.86	94155	9.88
11	167113	9.09	72027	9.63	95551	10.19
12	178451	9.34	78986	9.44	104149	9.92
13	163425	9.25	70304	10.31	92446	10.10
14	169920	9.63	76414	9.47	98770	10.33
15	168319	8.80	75375	11.13	98675	9.94
All	2711971	9.40 ± 0.07	1192554	9.73 ± 0.09	1585829	10.15 ± 0.13

Table 7.3: The results for the 16 sub-samples and the full Monte Carlo simulation sample (bottom line). The β per region for not converted photons is given and the π^0 statistics evaluated from the π^0 mass curve fit. The statistical error quoted for the full sample is determined from the RMS of the sub-sample measurements.

identical in size, in order to get an estimation of the statistical error of the method. Another reason for such a large statistics is that the π^0 contributing to the β estimation must have both photons of the same type (converted or not converted), passing the cuts and absorbed in the same region of the calorimeter. This is necessary in order not to mix the coefficients of different ECAL areas and electromagnetic shower types. Those constraints reduce drastically

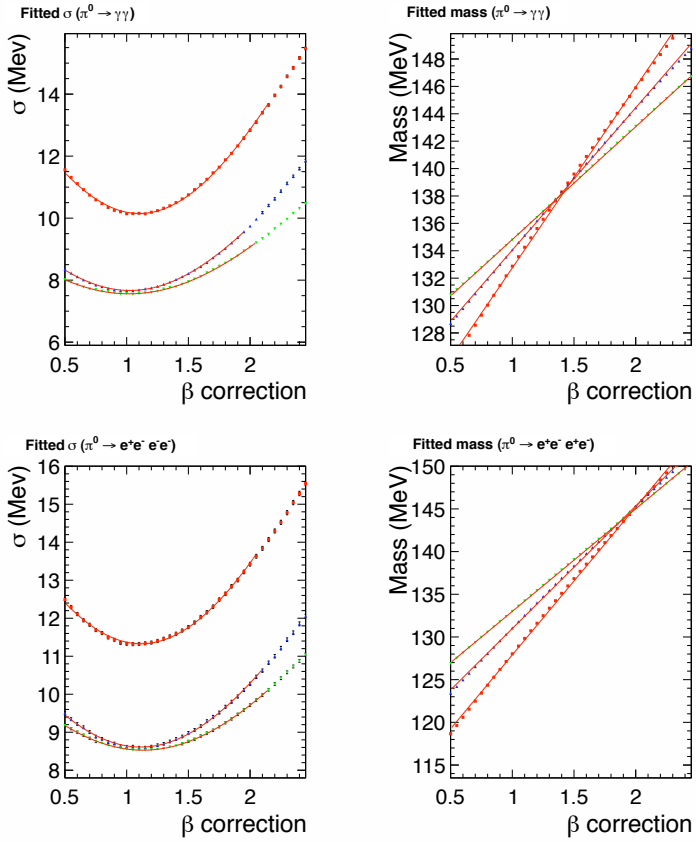

Figure 7.12: The figure shows the extraction of the 6 β parameters for the photons (top) and the electrons (bottom) in the three regions, outer(red dots), middle (blue dots) and inner (green markers) and on the full Monte Carlo sample. The right curves show the dependency of the π^0 mass peak position with respect to the β coefficient.

the number of π^0 per event. Finally, the mass curve must be properly described with as less statistical fluctuations as possible.

40 mass curves are built from 40 β hypothesis in each region and for the 17 (16+1) samples.

6 β values are extracted as explained in section 7.3.1. The width minimization parabolas for the full sample are visible on figures 7.12, the left curves showing the σ measured versus the multiplicative correction applied to β (the initial values used in the reconstruction are listed in 7.2, column "β_{rec} ") in the three regions, for the photons (top) and the electrons (bottom). The right plots of the same figure show the variation of the mass peak position versus β in the same cases. The figure 7.11 is the mass curve obtained for the smallest width in the outer region and for the not converted case.

The 6 β values are also extracted from each of the 16 sub-samples. The resulting coefficients are shown on the histograms of figure 7.13 altogether with the full sample extraction (red marker). In order to estimate the statistical error on β, the root mean square from the determination of the 16 β values is evaluated for each electromagnetic shower type and each region. The statistics of the small samples is obtained by integrating the gaussian part of the

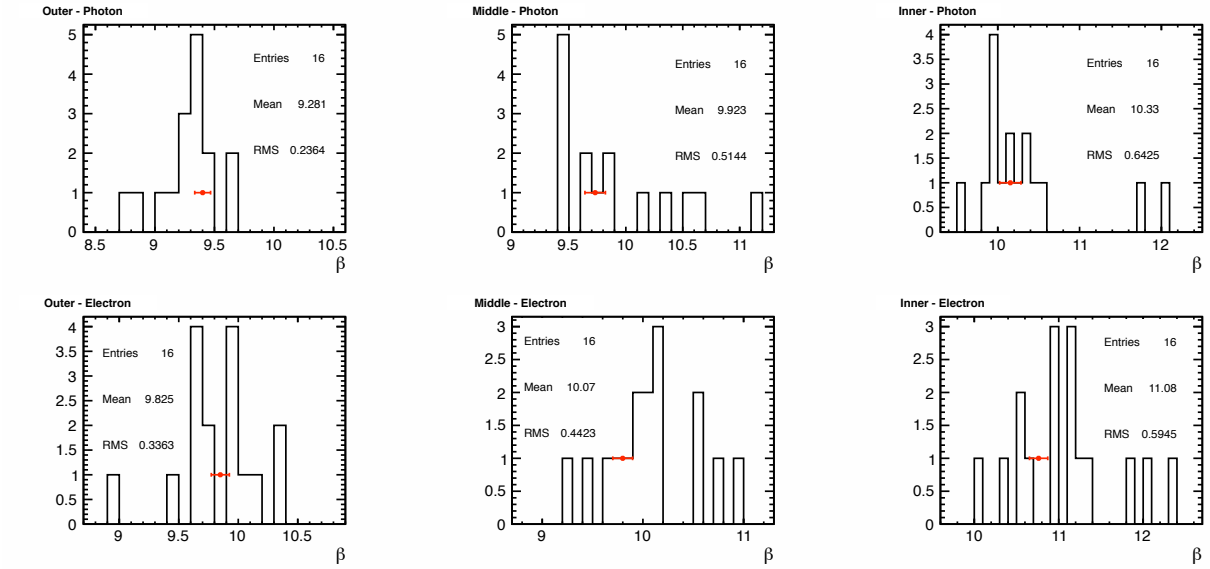

Figure 7.13: The β coefficients extracted from the 16 sub-samples (histograms) and the full sample (red marker). The top line corresponds to the photon case and the bottom one to the electron β parameters. The columns are for the outer (left), middle (center) and inner (right) regions. The full sample measurement error is extracted from the spread of the 16 measurements as described in the text.

Sample	N_{Outer} (ee)	β_{Outer} (ee)	N_{Middle} (ee)	β_{Middle} (ee)	N_{Inner} (ee)	β_{Inner} (ee)
0	96002	9.70	42816	10.51	78474	10.91
1	109724	8.94	50644	9.23	89763	12.03
2	101206	10.00	46097	10.04	79586	10.08
3	105670	9.63	49847	10.00	85356	10.54
4	100844	10.07	45151	10.02	77136	11.27
5	107096	9.77	48668	10.57	86265	11.15
6	103582	9.65	48377	10.18	81545	10.34
7	105690	9.94	48000	10.10	84629	10.70
8	106143	10.30	52387	9.77	86742	11.38
9	108305	9.97	49708	10.74	86313	10.92
10	101101	10.34	45147	9.88	78212	10.93
11	101875	10.12	47722	10.13	81140	12.35
12	110843	9.91	50616	9.95	86473	11.16
13	97559	9.62	46026	9.68	78927	11.85
14	103630	9.74	47811	10.90	79098	10.53
15	104706	9.47	48972	9.43	84927	11.17
All	1672924	9.85 ± 0.08	773910	9.80 ± 0.10	1330155	10.76 ± 0.11

Table 7.4: The results for the 16 sub-samples and the full Monte Carlo simulation sample (bottom line). The β per region for converted photons is given and the π^0 statistics evaluated from the π^0 mass curve fit. The statistical error quoted for the full sample is determined from the RMS of the sub-sample measurements.

mass curve fit.

The tables 7.3 and 7.4 give the extracted statistics in the three regions, for photons and electrons respectively, and the β coefficients obtained. The last line of the table gives the same

parameters for the full sample and includes the estimated statistical error on β scaled from the RMS of the 16 measurements and the statistics evaluated from the integral of the gaussian part of the fit of the full sample.

The β parameters for the electrons are slightly larger than for the photon shower as was expected. The overall statistical error from the large sample is roughly 1% but the systematics is difficult to extract and most certainly larger.

Zone	Outer	Middle	Inner
π^0 mass (MeV/c)	134.5	134.4	135.0

Table 7.5: π^0 mass obtained by using the values of α_{true} (calibration of the ECAL from the Monte Carlo truth information) and β (π^0 mass width minimization).

A final cross-check is performed by looking at the final π^0 mass obtained in the three regions using the α_{true} and determined β coefficients (see table 7.5). Notice that the π^0 mass peak position has never been used, neither for α_{true} (obtained from the reconstruction energy of photons in the Monte Carlo) nor for β (evaluated from the π^0 mass width minimization).

The systematics can be evaluated from the difference between the calibration performed with the Monte Carlo truth information and the width minimization β extraction. The shift are respectively of 4.0, 0.6 and 4.8 % in the outer, middle and inner regions. A systematics of 5% will be quoted whatever the regions.

7.5 β extraction from the 2010 data sample

The data stored in 2010 have been used to measure the β parameters of the LHCb PRS. A large sample of 93010464 minimum bias events[6] has been used and split in 10 sub-samples in order to test the stability of the fit convergence on a smaller statistics. The results are showed on tables 7.6 and 7.7 in the photon and electron cases respectively.

The spread of the β extraction on the sub-samples is quite similar to the one obtained with the Monte Carlo and is the sign of the good stability of the fits. The width curve for the data are shown on figure 7.14 and are also very similar to what was measured on a Monte Carlo sample (figure 7.12).

The values measured are all above the coefficients originally used on the reconstruction and which reached 8.3, 8.8 and 9.5 for the outer, middle and inner zones respectively. The correction are of the order of 5 to 10%. This feature looks also confirmed by comparing the π^0 mass measurements from photons depositing energy or not depositing energy in the PRS. But the values used in the reconstruction have been extracted from an old simulation.

In section 7.4.1, the reconstruction factor had been re-estimated and were corrected by 8 to 14% (see table 7.2). Comparing these new estimations with the calibration performed from the data, the difference is now only of 3.9, 5.8 and 2.7% in the outer, middle and inner. This shows

[6]The LHCb data are categorized according to several selection cuts. This process is called the stripping. The events used here are from the minimum bias stripping line. They have been produced during the reconstruction pass number 5 and the 9th stripping of the data.

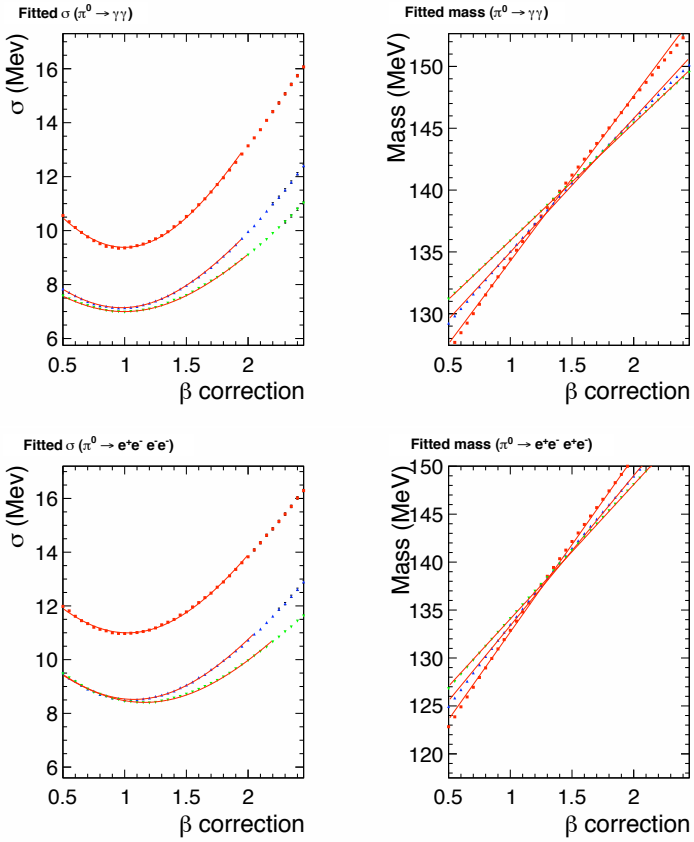

Figure 7.14: The two left plots show the evolution of the π^0 mass width with respect to the β PRS parameter. Those curves are obtained from real data recorded in 2010. The points are the actual measurements, the fit is indicated by the red curve. The right plots show the dependency of the π^0 mass reconstruction with the β value. The two top figures correspond to the "photon" PRS calibration case and the bottom ones to the electron calibration.

a good agreement between data and Monte Carlo if we take into account the 5% systematic error extracted from the Monte Carlo study. The table 7.8 gives the final results for the PRS calibration on the data in the "photon" and "electron" cases and for the 3 zones. The systematic uncertainties (assuming 5%) and statistical errors are also given in the same table.

Notice that there was no specific β value for the electrons up to now and this is the first estimation which is moreover extracted from the data themselves.

The stability of the method has been tested both on data and Monte Carlo by changing the fit range and changing the initial values. The observed differences are smaller than the statistical errors quoted in tables 7.6 and 7.7.

The mass peak position can be used to estimate the ECAL energy scale.

The results are given in table 7.9 and lead to corrections ranging from 0.2% to 1.0% maximum in the electron case and the inner region. Nevertheless, notice that it is not planed yet to have specific corrections for the electrons energy measurements in the ECAL.

With such small ECAL energy corrections, an iteration on the β extraction doesn't lead to

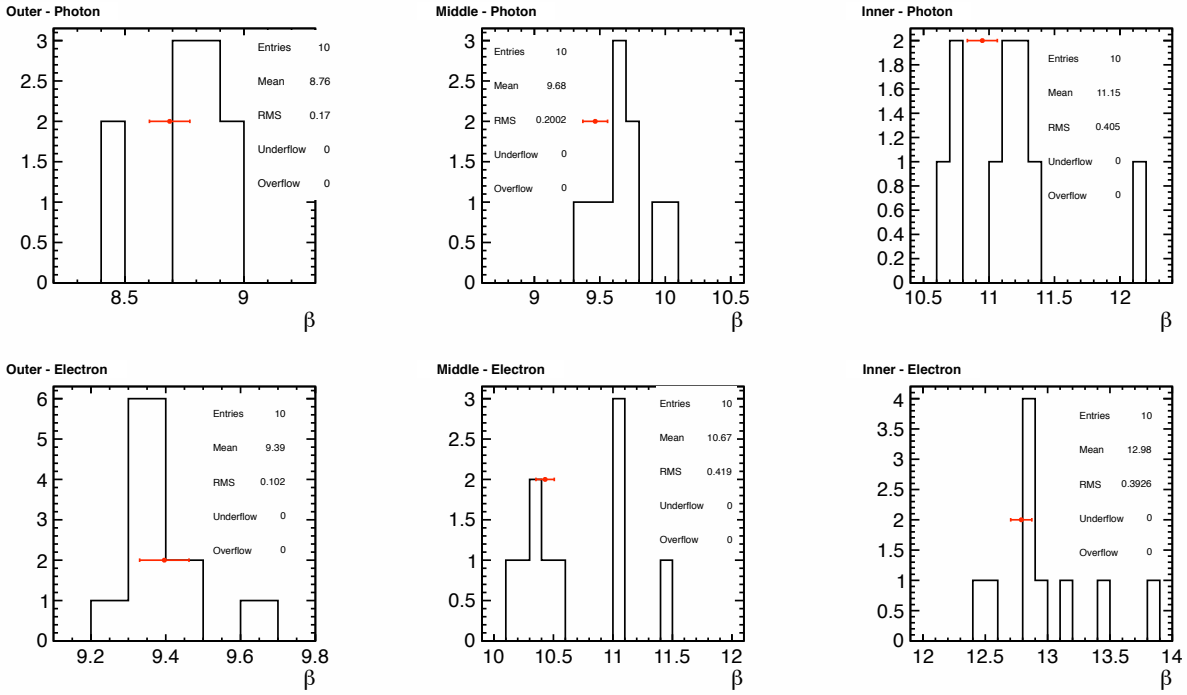

Figure 7.15: Extraction of the β coefficients in the electron case and the three regions. The lines give results for the 10 sub-samples described in the text and the full statistics. The N_{zone} columns are the number of π^0 extracted from the fit.

Sample	N_{Outer} $(\gamma\gamma)$	β_{Outer} $(\gamma\gamma)$	N_{Middle} $(\gamma\gamma)$	β_{Middle} $(\gamma\gamma)$	N_{Inner} $(\gamma\gamma)$	β_{Inner} $(\gamma\gamma)$
0	167459	8.90	69331	9.93	73517	11.28
1	276108	8.87	115716	9.30	124426	10.80
2	280054	8.72	111282	9.69	120153	11.03
3	126710	8.45	51360	10.02	52090	12.17
4	255856	8.81	102744	9.60	109309	11.13
5	262336	8.82	107370	9.66	112973	11.10
6	248563	8.71	102091	9.78	109410	11.37
7	272246	8.99	108839	9.47	119247	11.26
8	267158	8.40	108392	9.74	112788	10.68
9	225800	8.76	91102	9.51	100980	10.75
All	2379585	8.69 ± 0.08	966280	9.46 ± 0.09	1032522	10.95 ± 0.11

Table 7.6: A minimum bias real data sample of 2010 has been split in 10 sub-samples. The extraction of the β parameters for the photons in each region of the calorimeter system is listed here for each sub-sample and the total statistics where the errors quoted are extracted from the Monte Carlo study. The columns N_{Outer}, N_{Middle}, N_{Outer} indicate the number of π^0 measured from the fit.

Sample	N_{Outer} (ee)	β_{Outer} (ee)	N_{Middle} (ee)	β_{Middle} (ee)	N_{Inner} (ee)	β_{Inner} (ee)
0	171908	9.42	81091	10.54	110550	13.41
1	278514	9.33	126490	11.10	183708	12.87
2	278917	9.33	127715	10.40	184871	12.80
3	125059	9.35	55895	10.22	82220	13.19
4	245895	9.37	113630	10.35	162148	13.00
5	253896	9.27	118650	11.03	170299	12.84
6	250080	9.69	114323	10.40	163864	13.83
7	269721	9.36	124963	11.41	176263	12.54
8	269114	9.31	121125	11.08	170601	12.88
9	220920	9.41	100772	10.16	144397	12.41
All	2364111	9.40 ± 0.07	1080191	10.43 ± 0.08	1547709	12.79 ± 0.08

Table 7.7: Extraction of the β parameters for the electrons in the three regions of the calorimeter system. The numbers are given for each sub-sample obtained by splitting the total statistics for which the results are given on the last line of the table. Here, the errors are extracted from the Monte Carlo study. The columns N_{Outer}, N_{Middle}, N_{Outer} indicate the number of π^0 measured from the fit.

	β_{Outer}	β_{Middle}	β_{Inner}
$\gamma\gamma$	$8.69 \pm 0.43 \pm 0.08$	$9.46 \pm 0.47 \pm 0.09$	$10.95 \pm 0.55 \pm 0.11$
$(e^+e^-)(e^+e^-)$	$9.40 \pm 0.47 \pm 0.07$	$10.43 \pm 0.52 \pm 0.08$	$12.79 \pm 0.64 \pm 0.08$

Table 7.8: PRS calibration results for the three regions and the photons/electrons. The quoted errors are the systematic uncertainty (assuming 5%) and the statistical errors evaluated from the Monte Carlo study.

	π^0 mass (β_{Outer})	π^0 mass (β_{Middle})	π^0 mass (β_{Inner})
$\gamma\gamma$	134.32 (0.5%)	134.73 (0.2%)	135.87 (0.6%)
$(e^+e^-)(e^+e^-)$	134.16 (0.6%)	134.55 (0.3%)	136.35 (1.0%)

Table 7.9: The reconstructed π^0 mass after PRS calibration. The ECAL energy scale corrections to be applied for photons and electrons are given brackets.

any significant variation of the coefficients and no iteration procedure is applied.

Conclusions

During the past years, I worked mainly on the design of the LHCb calorimeter electronics. This document is an overview of the work which has been done. This was intended to be both a description of my activities but also a document that could be considered as a future reference on the electronics and its design. The moment to write it is appropriate. The LHCb electronics has been designed, installed and commissioned. One year has passed since the first collisions at high energy occurred and we have sufficient hindsight on the calorimeter system.

The electronics of the detector has been a common work done by a small group of physicists and engineers at LAL. This document being an "habilitation à diriger des recherches", I did not talk about all the work which has been done and I described only the activities in which I was engaged. I tried to give the references when an essential part was missing. Moreover, I mainly described the hardware without mentioning the periods of installation, test and commissioning of the electronics although they have been very time consuming activities. The first beam came in late 2009 (I will not talk about the incident of 2008). I have had the chance to spend almost one year and a half at CERN from mid 2009. This gave me the opportunity to participate to the first data acquisitions both being deeply involved in the LHCb calorimeter but also working in the control room and during shifts with the members of the other sub-detector groups. This period was very exciting and very enriching.

From the beginning of the data taking, the calorimeter was in a very good shape. The last worry concerned the noise between the CROC and a specific FEB in the crates (see section 3.5.5). But, thanks to the prompt reaction of the group, the problem was identified, a solution (the design of the present shielding) was found and the noise that was slightly larger than expected disappeared by Summer 2009.

TED runs took place before the actual first circulating beams and collisions. They consisted in having a proton injection up to the entrance of the LHC where the "low intensity" beam was stopped by a screen. This led to bursts of particles due to the proton-screen interaction, mainly muons, that reached the LHCb detector. The interest for those events concerned essentially the tuning of the timing of the cells of the calorimeter. Although a precise time adjustment was not possible with TED, those runs allowed us to learn how we could calibrate the detector efficiently and using the minimal amount of data, so that most of the time could be dedicated to physics runs. This was the time when most of the slow control tools have been designed, for example, to extract calibration parameters and perform scans on the full calorimeter system.

The calorimeter system had quite a lot of pressure during the first data taking period, at the end of 2009. The first level trigger was used to filter the events and this trigger was relying on the calorimeter information provided by the electronics. This was also a reason not to loose time on calibration runs specific to our system as this would have blinded the full detector for

some time. The timing of the calorimeter was rapidly done by Marie-Noëlle Minard, from the method proposed by [66]. I integrated the $\cos(\theta)$ and PMT high voltage corrections and the first set of precise time delays to apply to the cells was calculated and loaded through slow control into the electronics. After a few runs we obtained a good precision and the stability of our system has been welcomed by the full collaboration and provided a trusty trigger information. The first particles have been rapidly seen, the π^0 peak being observed almost online from the first data samples.

Part of this work was done again at the beginning of 2010 with the increase of the statistics and of the energy of the machine. Since, that moment, our understanding of the detector improved. The first precise calibrations appeared after a few weeks. This was an important task that is not completely achieved yet. The rapidly changing beam conditions of 2010 did not help in extracting easily the relevant parameters. Moreover, the pile-up that reached up to 2.7 average events per crossing (it was expected not to overtake 0.4 in "nominal") led to unforeseen difficulties in reconstructing the events. Nevertheless, even in those unexpected conditions, the calorimeter system was reliable and no major problem appeared in 2010.

After the time adjustment of the cells, the energy calibration of the detector was the second step. The work was done with regularity and the almost weekly calibration meetings of the beginning permitted to coordinate efficiently the work of the whole group. The calibration presented in this document is a fraction of the work done by a few people among the calorimeter group to extract the most precise set of coefficients for the SPD, PRS, ECAL and HCAL and obtain the most relevant data from the detector and for the physics analysis.

2011 will mostly be another year of increasing statistics, the aim being ultimately to reach 1fb^{-1} by the end of the year. The winter shutdown has been used to consolidate the electronics and to fix the spares. Let's hope that the system stability and functioning will be as much satisfying in the next year as in 2010.

Bibliography

[1] I. Belyaev B. Bobchenko V. Egorychev Y. Gilitsky A. Golutvin O. Gouchtchine I. Korolko T. Kvaratskheliia A. Arefev, S. Barsuk. Organization of the monitoring system for the lhcb electromagnetic calorimeter. *LHCb-INT-2009-019*, 2009.

[2] ACTEL. Ax family datasheet. *June 2002*, 2002.

[3] Y; Denissov S; Dzhelyadin R I; Kobelev A; Konoplyannikov A K; Kurakina O; Matveev V; Nekipelova G D; Obraztsov V F et al. Afanasieva, L G; Bogomolov. The hadron calorimeter design and construction. *LHCb-2000-045*, 2000.

[4] Sukesh K. Aghara. Characterization of an in-core irradiator for testing of microelectronics in a mixed radiation environment. *PhD thesis, University of Texas (Austin)*, August 2003, 2003.

[5] J. Lefrançois B. Delcourt. Investigation of widening of the p0 mass peak with electronic defects. *LHCb-2000-029*, 2000.

[6] BNL. Radiation test. *http://klabs.org/richcontent/fpga_content/SXA_Series/BNL_08_01-/154SX16A_UMC_P22/BNL_08_01_A54SX16A_UMC_P22.htm*, 2000.

[7] BNL. Radiation test. *http://klabs.org/richcontent/fpga_content/pages/rad_data/sxs_rad-.htm#SEE*, 2000.

[8] BNL. Radiation test. *http://klabs.org/richcontent/fpga_content/SXA_Series/BNL0900/SX-A_UMC/Test_BNL0900_SX-A_UMC.htm*, 2000.

[9] BNL. Radiation test. *http://klabs.org/richcontent/fpga_content/SXA_Series/BNL1000/SX-A_UMC/Test_BNL1000_SX-A_UMC.htm*, 2000.

[10] A; Coca C; Dumitru D; Giolu G; Magureanu C; Petrescu R; Popescu S; Ajinenko I; Dorokhov A E et al. Bonnet, M; Schopper. The hadron calorimeter prototype design and construction. *LHCb-2000-035*, 2000.

[11] Boost. Boost c++ libraries, `http://www.boost.org/`. `http://www.boost.org/`.

[12] V. Tocut C. Beigbeder, D. Breton. A programmable clock distribution chip for lhcb calorimeter. *EDMS-709938*, 2004.

[13] N. Cabibbo. Unitary symmetry and leptonic decays. *Phys. Rev. Letter*, 10:531, 1963.

[14] CERN-ESE-PH. Cern gigabit optical link (gol) transmitter asic. *http://proj-gol.web.cern.ch/proj-gol/*, 2002.

[15] Machefert Frédéric Charlet Daniel. Calorimeter and specs component irradiation at psi in june 2005. *LHCb-2005-046*, 2005.

[16] J. Christiansen. Requirements to the l0 front-end electronics. *LHCb-2001-014*, 2001.

[17] The LHCb Collaboration. Letter of intent : A dedicated lhc collider beauty experiment for precision measurements of cp-violation. *CERN-LHCC-95-5*, 1995.

[18] The LHCb Collaboration. Technical proposal : A large hadron collider beauty experiment for precision measurements of cp-violation and rare decays. *CERN-LHCC-98-4*, 1998.

[19] The LHCb Collaboration. The lhcb magnet technical design report. *CERN-LHCC-2000-007*, 2000.

[20] The LHCb Collaboration. The rich technical design report. *CERN-LHCC-2000-037*, 2000.

[21] The LHCb Collaboration. The muon system technical design report. *CERN-LHCC-2001-010*, 2001.

[22] The LHCb Collaboration. The outer tracker technical design report. *CERN-LHCC-2001-024*, 2001.

[23] The LHCb Collaboration. The velo technical design report. *CERN-LHCC-2001-011*, 2001.

[24] The LHCb Collaboration. The trigger system technical design report. *CERN-LHCC-2003-031*, 2003.

[25] The LHCb Collaboration. The computing technical design report. *CERN-LHCC-2005-019*, 2005.

[26] The LHCb Collaboration. The lhcb online system. *CERN-LHCC-2005-039*, 2005.

[27] The LHCb Collaboration. Jinst the lhcb detector. *JINST*, 3, 2008. S08005,.

[28] The LHCb Collaboration. The inner tracker technical design report. *CERN-LHCC-2002-029*, 2009.

[29] J. W. Cronin. Cp symetry violation-the search for its origin. *Rev. Mod. Phys.*, 53:373, 1980.

[30] Dominique Breton Daniel Charlet. Specs: the serial protocol for the experiment control system of lhcb. *LHCb-2003-004*, 2003.

[31] Dominique Breton Daniel Charlet. Using the specs in lhcb. *LHCb-2003-005*, 2003.

[32] A. Hrisoho et al. Lhcb ecal/hcal front-end chip. *CERN-LHCb-2002-002*, 2002.

[33] A. Perez-Calero et al. The muon track alley of the lhcb high level trigger. *CERN Report LHCb-2008-075*, 2008.

[34] Arefev et al. Design of pmt base for the lhcb electromagnetic calorimeter. *LHCb-2003-150*, 2003.

[35] Arefev et al. Beam test results of the lhcb electromagnetic calorimeter. *LHCb-2007-149*, 2007.

[36] Arefev et al. Design, construction, quality control and performance study with cosmic rays of modules for the lhcb electromagnetic calorimeter. *LHCb-2007-149*, 2007.

[37] Aurelien Martens et al. Calibration of the lhcb calorimeters with energy flow. *LHCb-2010-021*, 2010.

[38] Beigbeder-Beau et al. Calorimeter readout card (croc) design. *LHCb-2004-008*, 2004.

[39] C. Beigbeder et al. Lhcb calorimeter front-end electronics radiation dose and single event effects. *LHCb-2002-021*, 2002.

[40] C. Beigbeder et al. The lhcb calorimeter front-end crate. *LHCb-2003-038*, 2003.

[41] C. Beigbeder et al. The trigger part of the calorimeter front-end card. *LHCb-2003-037*, 2003.

[42] C. Beigbeder-Beau et al. A joint proposal for the level 0 calorimetric triggers. *LHCb-99-017*, 1999.

[43] C. Beigbeder-Beau et al. The front-end electronics for lhcb calorimeters. *LHCb-2000-028*, 2000.

[44] C. Beigbeder-Beau et al. Description of the ecal-hcal front-end card. *LHCb-2003-036(EDMS-909465)*, 2003.

[45] C. Drancourt et al. The readout of the lhcb calorimeters. *EDMS-527942*, 2005.

[46] C. Vial et al. A new approach for the prediction of the neutron-induced seu rate. *IEEE Trans. on Nuclear Science*, 1998. vol 45 number 6.

[47] David Gascon et al. Cards, crates and connections for the calorimeters. *LHCb-2003-121*, 2003.

[48] G. Böhner et al. Front-end electronics for the lhcb preshower detector. *LHCb-2000-048*, 2000.

[49] G. Böhner et al. Very front-end electronics for lhcb preshower. *LHCb-2000-047*, 2000.

[50] G. Haefeli et al. The lhcb daq interface board tell1. *Nucl. Inst. Meth. A 560, (2006), 494-502*, 2006.

[51] Griffin et al. The role of thermal and fission neutrons in reactor neutron-induced upsets in commercial srams. *IEEE Transactions on Nuclear Science*, 1997. vol. 44, number 6.

[52] I. Lax et al. The gigabit optical transmitters for the lhcb calorimeters. *12th Workshop on Electronics For LHC and Future Experiments, Valencia, Spain*, pages 479–482, 2006. 25 - 29 Sep pp.

[53] J. J. Wang et al. Single event effects of a 0.15um antifuse fpga. *2002 MAPLD International Conference, Laurel, MD*, 2002.

[54] K. Johansson et al. In-flight and ground testing of single event upset sensitivity in static rams. *IEEE Trans. on Nuclear Science*, 1998. vol 45 number 3.

[55] O. Deschamps et al. B0->pi+pi-pi0 reconstruction with the re-optimized lhcb detector. *LHCb-2003-077*, 2003.

[56] O. Deschamps et al. Photon and neutral pion reconstruction. *LHCb-2003-091*, 2003.

[57] O. Deschamps et al. The ckm angle α at lhcb. *LHCb-2007-046*, 2007.

[58] P. Perret et al. Study of a preshower dynamics using high energy aleph ecal data. *LHCb-99-048*, 1999.

[59] S. Amato et al. Lhcb calorimeters technical design report. *CERN-LHCC-2000-036*, 2000.

[60] S. Amato et al. Hlt1 muon alley description. *CERN Report LHCb-2008-058*, 2008.

[61] S. Barsuk et al. Design and construction of the electromagnetic calorimeter for the lhcb experiment. *LHCb-2000-043*, 2000.

[62] S. Barsuk et al. Radiation damage of lhcb electromagnetic calorimeter. *LHCb-2000-033*, 2000.

[63] S. Bota et al. Scintillator pad detector front-end electronics. *LHCb-2000-027*, 2000.

[64] S. N. Filippov et al. Design and construction of the lhcb scintillator-pad/preshower detector. *LHCb-2000-042*, 2000.

[65] S. N. Filippov et al. Experimental performance of ps/spd prototypes. *LHCb-2000-031*, 2000.

[66] Yasmine Amhis et al. Proposal for a procedure for the time alignment in the ecal and hcal. *LHCb-2007-146*, 2007.

[67] G. Shaw F. Mandl. *Quantum field theory*. Wiley, 1984.

[68] M.Huhtinen F. Faccio. Computational method to estimate single event upset rates in an accelerator environment. *Nuclear Instruments and Methods in Physics Research*, 2000. A 4509 155-172.

[69] V. L. Fitch. The discovery of charge-conjugation parity asymmetry. *Rev. Mod. Phys.*, 53:367, 1980.

[70] L. Shekhtman G. Corti. Radiation background in the lhcb experiment. *LHCb-2003-83*, 2003.

[71] E. Guschin and S. V. Laptev. Monte-carlo study of lhcb preshower. *Note LHCb-2000-030*, 2000.

[72] J. Angel Hernando. The hadron alley description. *CERN Report LHCb-2009-034*, 2009.

[73] P. Moreira J. Christiansen, A. Marchioro and T. Toifl. Ttcrx reference manual. *http://ttc.web.cern.ch/TTC/TTCrx_manual3.11.pdf*, 2004.

[74] klabs. Fpga - programmable technologies web page. `http://klabs.org/fpgas.htm`, 2002.

[75] klabs. Programmable technologies web page. `http://klabs.org`, 2002.

[76] K. Koopmans. Current status of the cosmic ray calibrations of the lhcb ecal modules. *LHCb-2004-060*, 2004.

[77] I. Korolko. Neutron flux in the lhcb scintillator pad detector. *LHCb note Calo in preparation*, 2000.

[78] M. Lamont. Comparison of integrated luminosities. *Proceedings of Chamonix 2010 workshop on LHC Performance*, 2010.

[79] K. Maskawa M. Kobayashi. Cp-violation in the renormalizable theory of weak interaction. *Progr. Theor. Phys.*, 49:652, 1973.

[80] D. Schroeder M. Peskin. *An introduction to quantum field theory*. Addison-Wesley, 2002.

[81] F. Machefert. Lhcb calorimeter front-end electronics radiation dose and single event effects. *LHCb-2002-072*, 2002.

[82] F. Machefert. Photon identification. *LHCb-2004-032*, 2004.

[83] P. Moreira. Ttcrq manual, version 1.5. *CERN-EP/MIC*, 2004.

[84] pdg. Particle data group. `http://pdg.lbl.gov/index.html`.

[85] PVSS. PVSS : a SCADA (Supervisory Control and Data Acquisition) system. `http://lhcb-online.web.cern.ch/lhcb-online/ecs/PVSSIntro.htm`.

[86] Python. Python programming language. `http://www.python.org/`.

[87] ROOT. Root, a framework for data processing. `http://root.cern.ch/`.

[88] L. H. Ryder. *Quantum field theory*. Cambridge University Press, 1996.

[89] A. D. Sakharov. Violation of cp symmetry, c-asymmetry, and baryon asymmetry of the universe. *JETP Lett*, 5:24–27, 1967.

[90] E. Scifo. Identification of bremsstrahlung photons, 2010.

[91] V. Talanov. Estimation of absorbed dose levels at possible locations for lhcb detector electronics. *LHCb-2000-015*, 2000.

[92] B. Adeva et al The LHCb Collaboration. Roadmap for selected key measurements of lhcb. *arXiv:0912.4179v2*, 2009.

[93] wxWidgets. Cross-platform gui library,. `http://www.wxwidgets.org/`.

[94] E. A. Melnikov Y. Gilitsky, I. Korolko. The monitoring system for the lhcb ecal. *LHCb-2003-151*, 2003.

[95] A. Konoplyannikov V. Matveev V. Novikov M. Soldatov Y. Guz, R. Dzhelyadin. Design and integration of hv, led monitoring and radioactive-source system for hcal. *LHCb-2003-147*, 2003.

[96] James Ziegler. The stopping and range of ions in matter. *http//www.srim.org*, 2005.

Merci !

Avant mon arrivée au Laboratoire de l'Accélérateur Linéaire, je n'avais essentiellement fait que de l'analyse de données pour la physique et le sujet sur lequel on me demandait de m'impliquer était nouveau, en grande partie tourné vers la réalisation de l'électronique des calorimètres de l'expérience LHCb. Le physicien en charge de cette électronique était Jacques Lefrançois que j'avais déjà pu croiser sur ALEPH au cours de ma thèse. Je voudrais remercier Jacques pour ces dix années au LAL au cours desquelles, il m'a beaucoup appris, mais aussi pour sa disponibilité, sa gentillesse et toutes les réponses qu'il a su m'apporter, toujours avec simplicité.

J'aimerais également exprimer ma gratitude aux autres membres de mon jury, Achille Stocchi qui me fait l'honneur de présider mon jury d'habilitation et Pierluigi Campana ainsi qu'Isabelle Wingerter-Seez, Jacques Chauveau et Ken Wyllie qui ont accepté d'être rapporteurs de ce mémoire et de donner une partie de leur temps à le lire avec beaucoup d'attention, bien que le sujet soit parfois technique ou loin de leur travail quotidien. Merci pour leurs remarques et commentaires pertinents.

Je tiens à remercier l'ensemble des membres du groupe LHCb au LAL : Sergey Barsuk, Olivier Callot, Bernard D'Almagne, Benoît Delcourt, Frédéric Fulda-Quenzer, Jibo He, Bernard Jean-Marie, Aurélien Martens, Alexandra Martin Sanchez, Michelle Nicol, Patrick Robbe, Marie-Hélène Schune, Benoît Viaud et Ioana Videau. J'ai pu travailler directement avec certains d'entres-vous dans le cadre de LHCb, mais chacun contribue à l'excellente ambiance du groupe. Au-delà du LAL, ma reconnaissance va également à d'autres membres de l'expérience LHCb : Vanya Belyaev, Olivier Deschamps, Cyril Drancourt, Iouri Guz, Anatoli Konoplyannikov, Marie-Noëlle Minard, Stéphane Monteil, Valentin Niess, Pascal Perret, Andreas Schopper, Stéphane T'Jampens pour le travail effectué ensemble, votre aide ou votre soutien.

Ce travail n'est pas le fruit d'une seule personne, mais le travail d'un groupe constitué de physiciens et d'électroniciens de mon laboratoire et je tiens à remercier Christophe Beigbeder, Olivier Duarte et Daniel Charlet avec qui j'ai passé beaucoup de temps durant ces dernières années à la fois pour la conception de notre électronique, mais également son installation, sa maintenance ou bien dans le cadre des tests en faisceau. Je garde un excellent souvenir de ces moments...à tel point que je signe à nouveau pour l'upgrade ! Merci également à Laurence Le Thiec, Vanessa Tocut, Dominique Breton, Thierry Cacéres, Patrick Cornebise, Patrick Favre, Pierre Imbert et Khaï Truong pour leur aide au cours de ces années.

Je voudrais dire toute ma sympathie a l'ensemble des personnels de mon laboratoire que j'ai pu cotoyer, directement dans le cadre de mon travail sur LHCb, de mes enseignements ou plus simplement autour d'un café.

Enfin, merci à Carole, Côme et Maixent. Votre présence à mes côtés m'est précieuse à tout instant.

Abstract

LHCb is one of the four large experiments installed on the LHC accelerator ring. The aim of the detector is to precisely measure CP violation observables and rare decays in the B meson sector. The calorimeter system of LHCb is made of four sub-systems: the scintillating pad detector, the preshower, the electromagnetic (ECAL) and hadronic (HCAL) calorimeters. It is essential to reconstruct B decays, to efficiently trigger on interesting events and to identify electrons and photons.
After a review of the LHCb detector sub-systems, the first part of this document describes the calorimeter electronics. First, the front-end electronics in charge of measuring the ECAL and HCAL signals from the photomultipliers is presented, then the following section is an overview of the control card of the four calorimeters. The chapters three and four concern the test software of this electronics and the technological choices making it tolerant to radiations in the LHCb cavern environment. The measurements performed to ensure this tolerance are also given.
The second part of this document concerns both the identification of the photons with LHCb and the calibration of the calorimeters. The photon identification method is presented and the performances given. Finally, the absolute energy calibration of the PRS and ECAL, based on the data stored in 2010 is explained.

Résumé

LHCb est l'une des quatre grandes expériences installées sur l'anneau du LHC. Le détecteur a pour but la mesure précise de la violation de CP et de canaux rares de désintégration dans le secteur des mésons B. Le calorimètre de l'expérience est un ensemble de quatre sous-systèmes : le détecteur de pied de gerbe, le "preshower" et les calorimètres électromagnétique (ECAL) et hadronique (HCAL). Il est essentiel pour la reconstruction des événements, pour le déclenchement de l'expérience et pour l'identification des électrons et des photons.
Après une revue du détecteur LHCb, l'électronique des calorimètres est décrite dans la première partie de ce mémoire. Dans un premier temps l'électronique de lecture des voies des photomultiplicateurs des ECAL et HCAL est présentée en mettant l'accent sur ses performances, puis la carte de contrôle de l'ensemble du système calorimétrique de l'expérience est détaillée. Les chapitres trois et quatre concernent les programmes de test de cette électronique, les choix technologiques permettant de la rendre suffisamment tolérante aux radiations et les mesures quantifiant cette tolérance.
La seconde partie de ce mémoire porte d'abord sur l'identification des photons avec les calorimètres de LHCb. La méthode est présentée avec ses performances. Enfin, l'étalonnage absolu en énergie des PRS et ECAL, basée sur les données enregistrées avec le détecteur en 2010, est décrite dans le dernier chapitre de cette même seconde partie.